Simulation of the dynamics and geometry of broad line region in active galactic nuclei

CAMK
PAN

Author: Mohammad Hassan Naddaf

Advisor: Prof. Bożena Czerny

CENTRUM ASTRONOMICZNE IM. MIKOŁAJA KOPERNIKA
POLSKIEJ AKADEMII NAUK

A thesis submitted in partial fulfillment of the requirements for the degree of
Doctor of Philosophy
in
Astronomy

March 23, 2023

Abstract

Broad emission lines, produced due to complex motion of illuminated material in a certain nuclear region of most active galaxies (known as the broad line region), are the most characteristic features of the optical/UV spectra of these sources. However, the dynamical nature of the broad line region (BLR) of active galaxies remains an open question, with observed evidence indicating a largely Keplerian motion alongside the possible traces of inflow or outflow. In this thesis, I present a comprehensive investigation into the BLR dynamics through analysing the efficiency of the dust driving mechanism, which is based on radiation pressure acting upon dust present at the surface layers of the accretion disk. Employing a non-hydrodynamical approach, I examine the behavior of dusty clouds leaving the disk surface and moving in the radiation field of the entire accretion disk, utilizing a realistic model for dust opacity and introducing a geometrical model as proxy for the local shielding. In Paper I, I expand the idea of the basic dynamical one-dimensional model of dust-driving mechanism responsible for the formation of broad line region in active galaxies, developed by Czerny & Hryniewicz (2011), known as FRADO (failed radiatively accelerated dusty outflow). We present the 3D numerical version of the model (2.5D due to azimuthal symmetry) in detail. I developed a non-hydrodynamical model with the single-cloud approach to the dynamics of BLR, but we carefully model the dust radiation pressure and the 3-D motion of a cloud. We showed that the radiation pressure exerted upon dusty clouds is potent enough to cause a dynamic outflow from the surface of accretion disk. I showed that the overall dynamics of BLR in this model is very complex, and the radial structure of BLR consists of zones of mostly failed winds, but also of an outflow from intermediate radii. The dynamics is strongly influenced by the Eddington ratio of the source, with high Eddington ratio sources showing a complex velocity field mentioned above and with significant vertical velocities relative to the local Keplerian rotation velocity of accretion disk, while lower Eddington ratio sources produce smaller vertical velocities and most of emission originates in proximity to the surface of accretion disk. Ultimately, the cloud dynamics serves as the principal determinant of the three-dimensional geometry of the BLR. In Paper II, we performed a preliminary test of the model using the observationally established radius-luminosity relation in AGNs. In the model the location of the BLR is not a parameter but it is determined mostly by the dust sublimation temperature. We showed that the model with different values of accretion rate and with adjusting the shielding effect can explain the observed location of the BLR comming from the most recent sample of sources with reverberation measured $H\beta$ time-delays which includes the spread over the phenomenological relation with respect the Eddington ratio of the source. In Paper III, we tested the model by calculating the predicted spectral line generic profiles, using a large grid of results from the 2.5D FRADO numerical code. In this work, we have conducted an analysis of the impact of various parameters, including accretion rate, black hole mass, viewing angle, and dust-to-gas mass ratio, on the shape of the spectral line profiles. Our results demonstrated that the spectral line profiles are significantly influenced by the dust-to-gas mass ratio, which regulates the strength of the radiation pressure. We have also shown that the model can appropriately explain the shapes of the low-ionized broad emission lines, such as MgII and $H\beta$, observed in quasars mean spectrum. In this comparison, the only free parameter of the model was the dust-to-gas mass ratio, since the mass and Eddington ration were taken from the peaks of the quasar distribution for these parameters, and the viewing angle also represented the mean quasar viewing angle.

Streszczenie   (Abstract in Polish)

Szerokie linie emisyjne, powstające z wyniku złożonego ruchu oświetlonej materii w pewnym obszarze jądra większości aktywnych galaktyk (znanym jako obszar szerokich linii emisyjnych), są najbardziej charakterystycznymi cechami widm optycznych/UV tych źródeł. Jednak natura dynamiczna obszaru emitujacego szerokie linie amisyjne (*ang. BLR*) aktywnych galaktyk pozostaje otwartym pytaniem, a obserwowane dowody wskazują na w dużej mierze keplerowski ruch orbitalny, z możliwymi śladami wpływu lub wypływu w kierunku radialnym. W niniejszej pracy przedstawiam wszechstronne badania dynamiki BLR w oparciu o model ruchu materii spowodowany działaniem cisnienia promieniowania na pył obecny w powierzchniowych warstwach dysku akrecyjnego. Wykorzystując podejście niehydrodynamiczne, badam zachowanie chmur gazu i pyłu opuszczających powierzchnię dysku i poruszających się w polu promieniowania całego dysku akrecyjnego, wykorzystując realistyczny model nieprzezroczystości pyłu i wprowadzając model geometryczny jako substytut lokalnego osłonięcia. W Pracy I, rozwijam ideę podstawowego dynamicznego jednowymiarowego modelu mechanizmu działania cisnienia promieniowania na pył odpowiedzialnego za powstawanie obszaru szerokich linii emisyjnych w aktywnych galaktykach, opracowanego przez Czerny i Hryniewicza (2011), znanego jako FRADO (*ang. failed radiatively accelerated dusty outflow*). Przedstawiamy szczegółową wersję numeryczną modelu 3D (2.5D ze względu na symetrię osiową). Skonstruowałem w tym celu model niehydrodynamiczny opisujący ruch szeregu pojedynczych chmur reprezentujących dynamikę BLR, ale starannie modelujemy w nim siłę ciśnienia promieniowania pyłu. W niniejszej pracy pokazaliśmy, że siła ciśnienia promieniowania działa na chmury pyłu wystarczająco silnie, aby wywołać dynamiczny wypływ z powierzchni dysku akrecyjnego. Pokazałem, że ogólna dynamika BLR w tym modelu jest bardzo skomplikowana, a struktura radialna BLR składa się głównie z powracających wiatrów (*ang. failed winds*), z wypływem z pośrednich promieni. Na dynamikę ma silny wpływ stosunek Eddingtona danego źródła, przy czym wysokie stosunki Eddingtona wykazują skomplikowane pole prędkości, jak omówione powyżej, oraz znaczne prędkości pionowe w stosunku do lokalnej prędkości rotacji keplerowskiej dysku akrecyjnego, podczas gdy niższe stosunki Eddingtona w żródle generują mniejsze prędkości pionowe i większość emisji pochodzi z materii w bliskiej odległości od powierzchni dysku akrecyjnego. Ostatecznie dynamika gromady chmur służy jako główny determinant trójwymiarowej geometrii BLR. W Pracy II, przeprowadziliśmy wstępny test modelu, używając obserwacyjnie odkrytej relacji promień-jasność w AGN. Pokazaliśmy, że model z różnymi wartościami tempa akrecji oraz z regulacją efektu osłony może wyjaśnić położenie obszaru BLR, które wynika z najnowszych pomiarów czasowych opóźnień linii Hβ dla szerego żródeł, który obejmuje rozrzut w tej fenomenologicznej relacji spowodowanym zakresem stosunku Eddingtona źródeł w próbce. W Pracy III, przetestowaliśmy model poprzez obliczenia przewidywanych profili linii widmowych, używając dużej siatki wyników z kodu numerycznego 2.5D FRADO. W tej pracy przeprowadziliśmy analizę wpływu różnych parametrów, w tym tempa akrecji, masy czarnej dziury, kąta widzenia oraz stosunku masy pyłu do gazu, na kształt profili linii widmowych z modelu. Nasze wyniki wykazały, że profile linii emisyjnych silnie zależą od stosunku masy pyłu do gazu, który reguluje siłę ciśnienia promieniowania. Pokazaliśmy również, że model dobrze wyjaśnia szerokie linie emisyjne nisko-jonizowane, takie jak MgII i Hβ, zaobserwowane w uśrednionym widmie kwazarów. W tym porównaniu tylko stosunek masy pyłu do gazu był swobodnym parametrem, ponieważ masa czarnej dziury i tempo Eddingtona zostały wyznaczone z maximum rozkładu parametrów kwazarów, a przyjęty kąt widzenia także reprezentował średni kąt widzenia kwazarów.

Declarations

I hereby declare that the content of this thesis was undertaken between October 2018 and January 2023 under the supervision of Prof. Bożena Czerny from the Center for Theoretical Physics, Polish Academy of Sciences, after my registration for the degree of PhD at Nicolaus Copernicus Astronomical Center, Polish Academy of Sciences.

Wherever the contributions of others are involved, I indicate this clearly, with due to reference to the literature, acknowledgment in manuscripts, and statements of contribution from coauthors, which I include in the Appendix.

This thesis includes content which have appeared in the following publications:

- *Chapter 3:* **Naddaf, M. H.**; Czerny, B.; Szczerba, R., 2021 *The picture of BLR in 2.5D FRADO: dynamics and geometry*, The Astrophysical Journal, 920, 30

- *Chapter 4:* **Naddaf, M. H.**; Czerny, B.; Szczerba, R., 2020 *BLR size in realistic FRADO model: The role of shielding effect*, Frontiers in Astronomy and Space Sciences, 7:15

- *Chapter 5:* **Naddaf, M. H.**; Czerny, B., 2022 *Radiation pressure on dust explaining the low ionized broad emission lines in AGNs*, Astronomy and Astrophysics, 663, A77

Apart from manuscripts included in this thesis, I have contributed to the following publications:

- Czerny, B. et al. **3rd author** (2023), *Dusty plasma in active galactic nuclei*, accepted for publication in European Physical Journal D (in press), arXiv e-prints, arXiv:2211.11022

- Czerny, B. et al. **7th author** (2023), *Accretion disks, quasars and cosmology: meandering towards understanding*, Astrophysics and Space Science, 368, 2, 8

- Prince R. et al. **12th author** (2022), *Wavelength-resolved Reverberation Mapping of quasar CTSC30.10: Dissecting MgII and FeII emission regions*, Astronomy and Astrophysics, 667, A42

- Naddaf, M. H. et al. **1st author** (2022), *The Wind Dynamics of Super-Eddington Sources in FRADO*, Dynamics, Vol. 2, No. 3, pp. 295-305

- Müller, A. L. et al. **2nd author** (2022), *Non-thermal emission from fall-back Clouds in the broad line region of active galactic nuclei*, The Astrophysical Journal, 931, 39

- Zajaček, M. et al. **10th author** (2021), *Time Delay of Mg II Emission Response for the Luminous Quasar HE 0435-4312: toward Application of the High-accretor Radius-Luminosity Relation in Cosmology*, The Astrophysical Journal, 912, 10

- Czerny, B. et al. **7th author** (2021), *Dark Energy Constraints from Quasar Observations*, Acta Physica Polonica A, 139, 389

- Zajaček, M. et al. **9th author** (2020), *Time-delay Measurement of Mg II Broad-line Response for the Highly Accreting Quasar HE 0413-4031: Implications for the Mg II-based Radius-Luminosity Relation*, The Astrophysical Journal, 896, 146

- Czerny, B. et al. **20th author** (2019), *Time Delay Measurement of Mg II Line in CTS C30.10 with SALT*, The Astrophysical Journal, 880, 46

Moreover, I am the leading author of the following manuscript submitted to the refereed journal:

- **Naddaf, M. H.** et al. **1st author** (2023), *Dust-driven wind as a model for broad absorption line quasars*, Astronomy and Astrophysics, under the first revision with only minor comments, arXiv e-prints, arXiv:2212.08222

Acknowledgements

I would like to extend my deepest gratitude and sincere appreciation to Professor Bożena Czerny, the epitome of an exceptional supervisor, for her memorable guidance, and support throughout my PhD journey. Her knowledge, expertise, and patience have been invaluable to me, and her unwavering belief in my abilities have been instrumental in shaping my research and academic growth. Beyond her scientific expertise, I truly admire her humanistic character and I feel incredibly fortunate to have had her as my supervisor. I will always cherish the lessons and values she has imparted on me.

I would also like to express my heartfelt appreciation to my late father, whose encouragement throughout my academic journey continues to inspire me. His memory will always be a source of strength and motivation for me. I am also grateful for the constant encouragement and belief given to me by my mother, my siblings, and my friends. The unwavering support and love I received from them have been a driving force behind my success.

Additionally, I am indebted to all of my collaborators who have provided me with their guidance and encouragement. My sincere gratitude goes to Prof. Ryszard Szczerba who made my business trip in the first year of PhD to the charming city of Toruń memorable by his great mentorship, exceptional hospitality, kindness, and genial personality. I am particularly grateful to Prof. Paola Marziani, Prof. Vladimír Karas, Dr. Mary Loli Martínez-Aldama, Dr. Marzena Śniegowska, Dr. Swayamtrupta Panda, Dr. Michal Zaječek, Dr. Raj Prince, Dr. Ana Laura Müller, Dr. Anabella Araudo, and Mgr. Vikram Kumar Jaiswal, who have all been instrumental in our group discussions, providing me with valuable insights and sparking many brilliant conversations.

Furthermore, I would like to express my appreciation to my previous supervisors, Dr. Jamil Ariaei, Prof. Hosein Haghi, and Prof. Shahram Abbassi, for their support during my early careers in science. They played a crucial role in helping me to take my first steps in the field of Physics and later Astrophysics.

Finally, I would also like to appreciate all the assistance, kindness, and support that I received during my PhD studies from the professors, staff, colleagues, and friends at the Nicolaus Copernicus Astronomical Center and the Center for Theoretical Physics.

Last but not least, I am thankful to the Polish grant agency, NCN, for the grant that funded research activities during my PhD studies. [1]

Contents

Chapter 1

Introduction

The nucleus of a galaxy contains a supermassive black hole at the center of a galaxy, which can be called as active nucleus when it swallows the ambient matter through a process known as accretion. The active episode of the nucleus of galaxies, known as Active Galactic Nuclei (AGN), is a crucial stage in their evolution. Through accretion process, feeding the black hole, the corresponding gravitational potential energy is transformed into huge amount of radiation that feedbacks the host galaxy in return and regulates its star formation activity, hence its evolution. On the other hand, there is a characteristic feature, i.e. Broad Emission Lines (BEL) in the spectra of bright AGNs. Measured from black hole, the radial distance of the region, where the kinematics of material manifests itself in BEL, known as Broad Line Region (BLR), scales with the corresponding AGN absolute luminosity through an observationally-calibrated phenomenological relation, known as radius-luminosity relation. Knowing the absolute luminosity, AGNs can thus be located on the Hubble diagram, hence recruited as distance indicators. This makes studying the underlying mechanism of BEL formation and also theoretical localization of BLR crucial.

My thesis, therefore, encompasses three published papers, as provided in chapters 3, 4, and 5, all devoted to studying the formation, dynamics, geometry, and other properties of BLR in numerical context. In this chapter, in order to locate my results into the big frame of AGN studies, first I will briefly surf the history and structure of AGNs, and also their prospected role in cosmology in section 1.1, followed by a comprehensive review on BLR in section 1.2 which is the main focus of this thesis. The chapter 2 is then fully devoted to the fundamental calculations behind the numerical computations in this work on the physics of BLR. Finally, in chapter 6, a summary of the thesis is presented along with a brief description of the future potential works, especially those in preparation or submission stage.

1.1 AGNs in a nutshell

The fascinating story of AGNs started earlier than a century ago with the observation of the galaxy NGC 1068 by Edward A. Fath (1909) who was aiming at clarifying the nature of the spiral nebulae. He found strong and composite both emission and absorption lines in the spectrum of NGC 1068. In almost two decades later, a more accurate observation of the same source by Vesto M. Slipher (1917) using a narrow spectrograph slit revealed that not only the emission lines are broader, compared to that of previously measured, but also the emission was covering a large range of wavelengths. This made him

to decline the ordinary interpretation of those line widths which was merely based on radial velocity. Later, Edwin Hubble (1926) also confirmed the presence of strong and broad emission lines and more importantly the planetary nebula–type spectrum of NGC 1068. Spectrograms of six galaxies with bright nuclei, including NGC 1068, obtained later by Carl K. Seyfert (1943), although came up with broad emission lines different in widths and shape of profiles, they were typically similar. Emergence of radio astronomy then led to introduction of a new class of objects in order to accommodate these apparently point-like sources. They were similar to stars in terms of optical appearance and size, but with significantly different spectra, so they were hence called as quasi-stellar radio sources, later named as quasars (QSOs). Twenty years after the systematic study by Seyfert, Schmidt (1963) (among his colleagues, Greenstein & Matthews 1963; Greenstein 1963; Hazard et al. 1963 all working on the puzzle of spectra of these objects) was smart enough to be the first one to realize the cosmological redshift in Balmer lines. The relatively (at that time) large redshift of 0.158 measured by Maarten Schmidt for the source 3C 273, and 0.37 measured by Jesse Greenstein for the source 3C 48 just shortly afterward, revealed the hugely large intrinsic luminosity of these sources.

It was first in early 1950s that the term Active Galactic Nuclei due to bright nuclei of these sources was coined in the Solvay Conference 1958 by Viktor Ambartsumian where he argued that this brightness should be due to explosions of large amounts of mass of an unknown nature in the galactic nuclei (Israelian, 1997). But a proper explanation for the enormous brightness of these objects was given just after the redshift measurements by Edwin Salpeter and Yakov Zeldovich in 1964 (Salpeter, 1964; Zeldovich, 1964), who all proposed that this is the result of accretion of material onto a supermassive black hole. Then in 1969, Donald Lynden-Bell (Lynden-Bell, 1969) came with the first calculations of a disk of gas in circular motion around a blackhole. Soon after, in 1973, the first convenient formalism for describing the process of accretion was introduced by Nikolai I. Shakura and Rashid A. Sunyaev (Shakura & Sunyaev, 1973), which is the most ever cited paper in the studies of accretion physics, although it was motivated by the discovery of Xray binaries, not quite by the mainstream of AGN studies.

Nowadays, AGNs are known as a spectacular class of astronomical objects with largely known structure and components due to modern high resolution images (e.g., GRAVITY Collaboration et al., 2018). The mainstream of studies on different aspects of AGNs contribute to a major part of research in astrophysics and cosmology, both observational and theoretical.

1.1.1 Structure & components of AGNs

The nuclei of many galaxies are highly luminous, powered by efficient accretion of matter onto a central supermassive black hole of millions to billions solar mass, transforming the gravitational energy into radiation, hence called as active galactic nuclei. AGNs thus primarily consist of a central black hole and accretion disk of material. Through the process of accretion of material onto black hole, other secondary components can be formed such as a jet, dusty torus, broad and narrow line emitting regions, etc.

The overall widely-accepted structure of AGNs, as shown in figure 1.1, can be described with a black hole at the center of a galaxy surrounded by an accretion disk emitting emitting predominantly in the optical/UV band, forming the Big Blue Bump. A jet may emanate from the vicinity of the central black hole perpendicularly to the disk plane which is a source of the two-peak non-thermal synchrotron and Compton emission visible over the broad frequency range from radio to gamma rays.
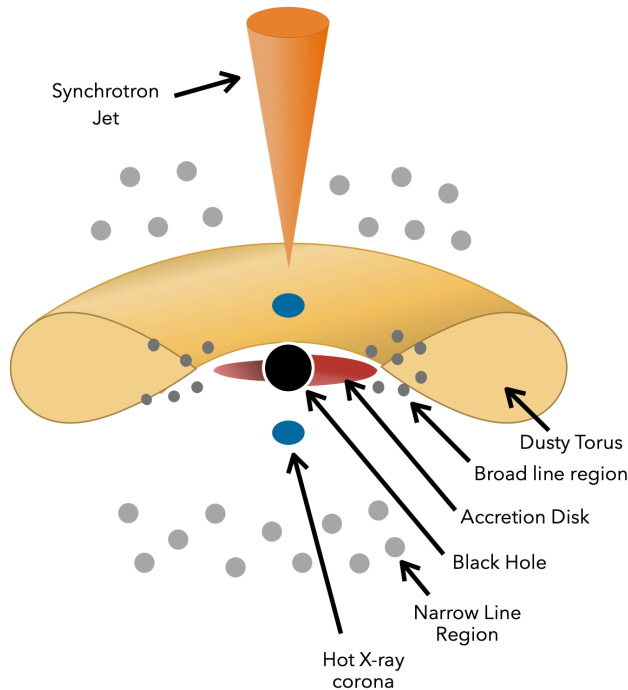
Figure 1.1: Components of AGNs adapted from Thorne et al. (2022); sizes are not in scale!

Thermal emission seen mostly in the hard X-rays comes from the corona, located close to the black hole, and there is also soft X-ray emission which comes from the warm corona and/or reprocessing of the X-rays by the surface of irradiated accretion disk. The system of disk and black hole are embedded within a large torus-like molecular dusty structure known as torus, which may obscure the nucleus from line of sight depending on the viewing angle. There are huge amount of plasma gas spanning from the vicinity of up to large distances from the disk surface, which contains clumpy dusty-gaseous material that forms the broad and narrow line region. These components are addressed one by one in the following.

Black hole

As far as known to the date, every single galaxy hosts at its center a supermassive black hole (SMBH) the mass of which ranges from 10^5 up to 10^{10} $M_\odot$ (Kormendy & Richstone, 1995). The SMBH is the central engine of an AGN where the material from the surrounding environment falls onto the black hole, that releases the gravitational energy and emits radiation. The presence of an SMBH in an AGN can be inferred from the observation of its effects on the surrounding environment, such as the shapes of emission lines in the AGN spectrum particularly in the X-ray band where relativistically smeared iron Kα line is seen in many sources. The compactness of the emitting region is also directly implied by the AGN variability. In some cases with less activity, the presence of an SMBH can be also directly confirmed by observing the velocity dispersions and motion of stars or gas clouds near the black hole. Also, the disk continuum contains information about BH through the Innermost Stable Circular Orbit (ISCO), which refers to the closest stable circular path that matter can take around a black hole without falling in. Moreover, there are exceptional cases of direct imaging of blackhole shadow, i.e. the images of blackhole at the center galaxies Sgr A* and M87 taken by Even Horizon Telescope (EHT). The study of SMBHs in AGN has important implications for our understanding

of the formation and evolution of galaxies and the growth of massive black holes over cosmic time (Kormendy & Ho, 2013).

The gravitational radius, r_g, defined as below for a non-rotating black, is a fundamental parameter used to characterize a black hole.

$$r_g = \frac{GM}{c^2},$$
(1.1)

where M is the mass of black hole, c is the speed of light, and G is the gravitational constant.

Accretion disk

The accretion disk forms as material from the surrounding environment falls onto the central super-massive black hole, with certain amount of angular momentum. The infalling material contains the gas and the dust. The structure and properties of the disk are influenced by the black hole mass, and the accretion rate, though magnetic fields can also play a crucial role in shaping the structure and properties of accretion disks by influencing the movement of charged particles in the disk, hence inducing turbulence, heating the disk, generating jets, affecting the transport of matter and energy, and forming hot spots and asymmetries.

The rate at which the matter is added to a central object, here a supermassive black hole is called accretion rate. It is typically measured in units of solar masses per year and represents the mass that is accreted per unit time. The gravitational energy released by the infalling material heats up the disk, causing it to emit radiation across the electromagnetic spectrum, including ultraviolet, optical, and X-rays. The total power radiated by the object, integrated over all frequencies is called bolometric luminosity, usually expressed in units of ergs per second (erg/s).

On the other hand, there is a useful general definition known as Eddington luminosity referring to the amount of luminosity emitted by a spherically symmetric object when the inward gravitational force is balanced by the outward force of radiation pressure acting on the fully ionized hydrogen gas. The Eddington luminosity is given by:

$$L_{\text{Edd}} = \frac{4\pi GM m_p c}{\sigma_T}$$
(1.2)

where L_{Edd} is the Eddington luminosity, G is the gravitational constant, M is the mass of the black hole, m_p is the mass of a proton, c is the speed of light, and σ_T is the Thomson scattering cross-section. Likewise, Eddington accretion rate can be found through

$$\dot{M}_{\text{Edd}} = \frac{L_{\text{Edd}}}{c^2 \eta}$$
(1.3)

where η is the efficiency of accretion flow.

The Eddington ratio, which is the dimensionless ratio of the accretion rate to the Eddington accretion rate, $\dot{m} = \dot{M}/\dot{M}_{\text{Edd}}$, or, equivalently, the dimensionless ratio of the bolometric luminosity to the Eddington luminosity, $\lambda_{\text{Edd}} = L_{\text{bol}}/L_{\text{Edd}}$, is a convenient and useful key parameter that determines the properties of the accretion disk and the emission it produces.

There are several different types of accretion disk models that are commonly used to describe the behavior of matter around a supermassive black hole. These include geometrically thin models, appropriate for AGNs, for which the height of the disk is far less than the corresponding radii, and moderately geometrically thick models with the disk height comparable to the radius:

- Standard thin disk model (SS disk: Shakura & Sunyaev, 1973): This is the simplest and most commonly used model, which assumes that the disk is flat, geometrically thin, and optically thick, and that the local dissipation of gravitational energy is mostly responsible for the heating and radiation of the disk. The temperature of the disk at a given radius is determined by the balance between energy released by viscous dissipation and radiative losses. The disk emits thermal radiation that basically follows a blackbody spectrum and its luminosity is proportional to the mass accretion rate onto the black hole. The radiation flux from a disk at the radius r from a unit area is given by the formula (Shakura & Sunyaev, 1973; Novikov & Thorne, 1973):

$$F(r) = \frac{3GM_{\mathrm{BH}}\dot{M}}{8\pi r^3} f(r), \tag{1.4}$$

  where $f(r)$ stands for the boundary conditions. The efficiency of accretion is such model depends only on $f(r)$ setting the location of the ISCO orbit, and is generally high, from 5.8% in a non-rotating, up to 42% in the maximally rotating black hole case.

  The Eddington ratio in the standard disk model is typically between 0.01 up 1. We mainly focus on sources with this range of accretion rates, hence we use the standard disk model in our computations.

- Advection-dominated accretion flow (ADAF) model (Narayan & Yi, 1994): In this model, the accretion flow is assumed to be radiatively inefficient, with most of the energy carried by the accreting gas advected onto the black hole rather than being radiated away. Such a disk is geometrically moderate and optically thin, electron temperature is usually different from the ion temperature, the emission mechanism is due to free-free emission (Bremsstrahlung) and synchrotron emission. The efficiency of accretion is low and difficult to estimate. This model is often invoked to explain the observed properties of low-luminosity black holes. The EHT image of M87 shows the ADAF around the blackhole. The Eddington rate in the ADAF model is very low, typically less than one percent of the Eddington luminosity.

- Slim disk model (Abramowicz et al., 1988): In a slim disk, the accreting gas forms a geometrically moderate disk, but the disk is optically thick to electron scattering. This means that radiation is trapped within the disk to some extent, but some can still escape. The Eddington ratio in slim disks is typically above one, and the efficiency of accretion drops with the rise of Eddington ratio. Such models are particularly important for understanding the behavior of super-Eddington accretion-rate black holes, such as those found in AGNs.

Corona

The X-ray corona is a region of highly energetic and hot gas (low-density, high-temperature plasma) that surrounds the central black hole and the accretion disk. Most of the corona emission originates very close to the black hole, as implied by the X-ray variability. This component is thought to scatter the ultraviolet photons via inverse Compton mechanism up from the disk to high energies, mainly to the X-ray band, hence responsible for the hard X-ray emission observed in many AGN (Haardt & Maraschi, 1991; Titarchuk, 1994). But the existence of the corona is not well predicted by the theory of accretion disks. Its geometry also is not well known; for example, models are proposed such as a thin outermost layer of the accretion disk (Haardt & Maraschi, 1991; Różańska, 1999), inner ADAF or

ionized inner edge of the accretion disk (Ichimaru, 1977; Narayan & Yi, 1994; Gardner & Done, 2014), lamp-post; serving as the base of the jet as well (Henri & Pelletier, 1991; Matt et al., 1991; Dauser et al., 2013; Ursini et al., 2020). Corona can directly illuminate the inner part of the disk which leads to formation of the soft X-ray emission lines (Różańska et al., 2002), a relativistically broadened iron Kα line (Tanaka et al., 1995), and the formation of the Compton reflection component seen in hard X-ray band (Pounds et al., 1990). Corona can eventually irradiate the outer parts of the disk and BLR clouds (Chen et al., 1989). The contribution of hard X-ray to the bolometric luminosity decreases with rising Eddington ratio (Kubota & Done, 2018). The soft X-ray excess is likely a combination of the reprocessing (soft X-ray lines and continua) with warm corona layer above the inner part of the disk developed due to magnetic heating of the disk surface layers (e.g., Różańska et al., 2015)

Broad Line Region (BLR)

The BLR is a region surrounding the central engine at a distance of a few hundreds to few thousands gravitational radii where clouds composed of gas and likely dust emit broad spectral lines, which are important for determining the central black hole mass and understanding the dynamics of the region. The BLR is comprehensively addressed in the Section 1.2 below. Source showing broad lines are classified as Seyfert 1 galaxies, broad line radio galaxies, or type 1 quasars.

Narrow Line Region (NLR)

The NLR is defined as a bi-conical structure of low-density ionized dusty clouds that surrounds the central engine of an AGN and emits narrow permitted and forbidden emission lines with full-width at half maximum (FWHM) less than 1000 km/s (Netzer & Laor, 1993). These clouds are thought to reside up to distances of about a kilo-parsecs from the central black hole, outflowing mostly pushed up by the radiation pressure and going through severe turbulence due to shocks so not virialized, and they are characterized by a direct line of sight to the innermost regions of the AGN system. This direct line of sight provides the high ionization radiation necessary to excite the narrow emission lines that are observed in the NLR. These lines are important for determining the density, chemical composition, and physical conditions of the gas in the NLR and for understanding the interaction between the AGN and its host galaxy. Some AGNs only show narrow lines and they are classified as Seyfert 2 galaxies, narrow line radio galaxies, or type 2 quasars.

Torus

The dusty torus is a doughnut-shaped region of dust and gas that surrounds the central engine and obscures the AGN from our line of sight. The dust torus can re-emit absorbed radiation in the infrared and sub-millimeter regions of the spectrum, making AGN appear as luminous infrared sources. The first hint on the presence of a dust dates back to a work by Rees et al. (1969), but the torus geometry was postulated by Antonucci & Miller (1985) at the basis of polarization studies.

Jet

Some AGNs are associated with highly collimated, relativistic outflows of gas known as jets. These jets can emit synchrotron radiation in the radio band and Comptonized emission dominating in Gamma rays. The presence or absence of jets in a particular source can depend on a variety of factors,

including the accretion rate, the black hole spin, and the surrounding environment, and can change over time. The presence of strong radio jets is considered a defining characteristic of radio-loud AGNs, as confirmed by several studies, including the study by Kellermann et al. (1994) who found that radio-loud AGNs are typically characterized by extended radio structures, such as radio jets and lobes, that emit synchrotron radiation across the entire radio spectrum.

A classification scheme for radio sources based on the morphology of their radio emission by Fanaroff & Riley (1974) divided radio sources into two main classes: compact (core-dominated) and extended (lobe-dominated) sources, known as FRI and FRII, respectively.

Traditionally, all AGNs are divided into radio-Loud (RL) and Radio-Quiet (RQ) AGN, from the point of view of the strength of their radio emission. First examples of RL AGN were radio galaxies. Later, this distinction was established in relation to quasars, with the threshold between the two categories set by either (1) radio flux density or luminosity (Peacock et al., 1986) or (2) the ratio of radio-to-optical flux density or luminosity (Schmidt, 1970). The origin of this classification can be traced back to Sandage (1965). Following the discovery of the first quasar, namely 3C 273, which was an extremely intense radio source, he recognized the presence of a multitude of similar sources in the sky that went undetected by the radio telescopes in operation at that time. Over time, radio loudness has been defined differently in various studies. It is important to note that these classical definitions are only applicable to type 1 AGN, as pointed out by Padovani et al. (2011) and Bonzini et al. (2013).

More recently, another division of radio AGNs into two sub-classes of jetted and non-jetted sources was introduced. Padovani (2016, 2017b) has contended that the distinction between RL and RQ AGN is not a mere semantic matter, but rather that these two categories denote fundamentally distinct objects. Specifically, RL AGN emit a significant portion of their energy non-thermally and generate powerful relativistic jets, while the multi-wavelength emission of RQ AGN is characterized by thermal emission, which is directly or indirectly associated with the accretion disk. Furthermore, Padovani argued that the designations RL and RQ are now outdated, misleading, and unsuitable. As the presence or absence of robust relativistic jets is the primary physical distinction between these two categories, it also follows that the maximum photon energies attained by these two classes differ considerably. For a most recent review, see Padovani et al. (2017); Padovani (2017a).

1.1.2 Unification scheme of AGNs

The idea of unifying AGNs through a model that explains the diverse observational properties of these sources dates back to 1990s, when (Antonucci, 1993; Urry & Padovani, 1995) suggested that the differences in observed properties of AGNs result from differences in our line of sight relative to the central regions of these sources.

A major breakthrough in the unification of AGNs came with the discovery of broad emission lines in the polarized light in the spectra of some Seyfert 2 galaxies, which had previously been considered to be a distinct class of AGNs. This discovery led to the recognition that Seyfert 1 and 2 galaxies are essentially the same type of object, with the differences in their observed properties being due to orientation effects. The orientation of the torus relative to our line of sight determines whether we see the AGN as a Seyfert 1 or a Seyfert 2. The original unification model primarily focused on Seyfert galaxies, but it has since been expanded to include other types of AGNs, such as Blazars and radio galaxies, by incorporating the role of relativistic jets in these sources (Netzer, 2015).

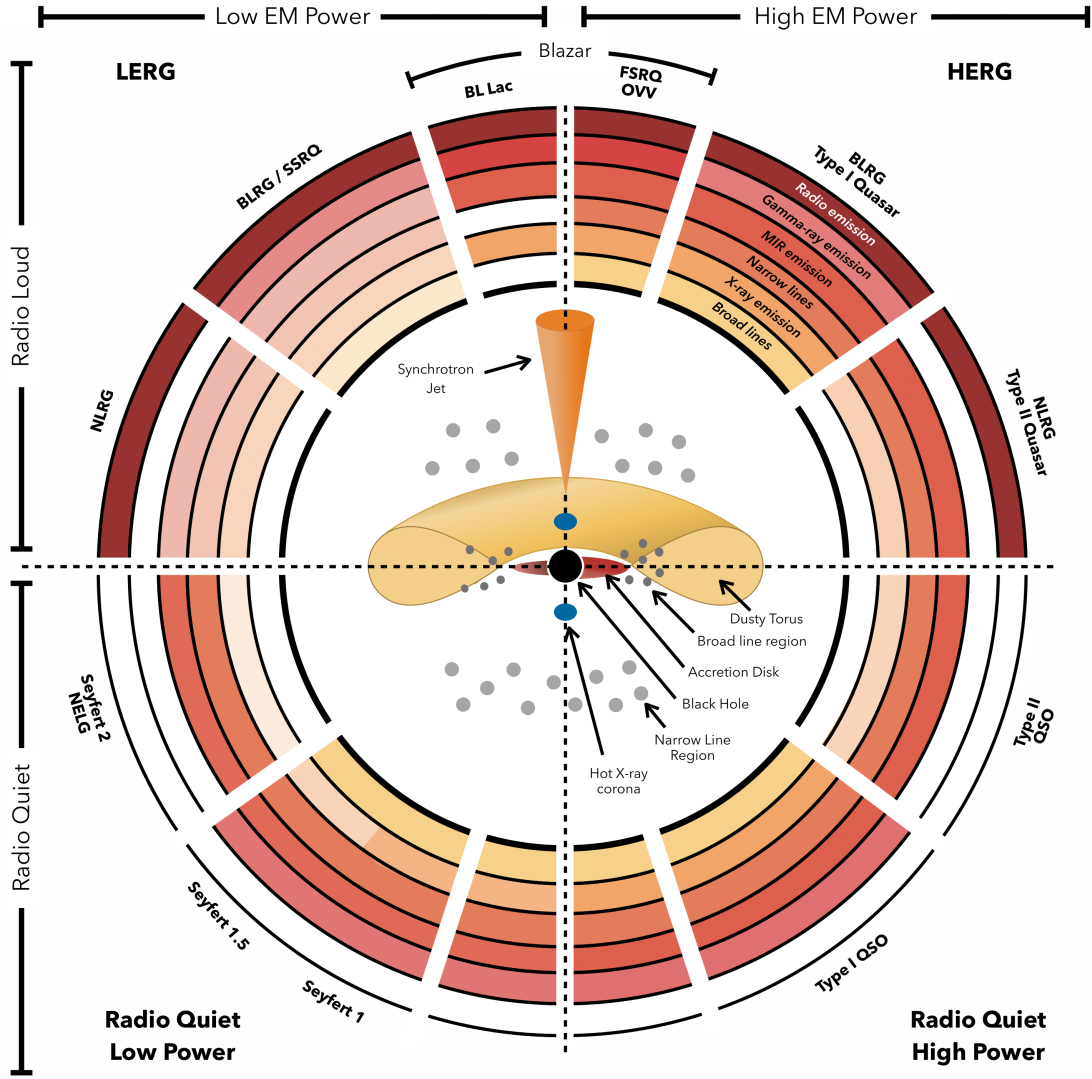A comprehensive sketch illustrating the unified model of AGNs is shown in figure 1.2. This model

Figure 1.2: Unification model of AGNs adapted from Thorne et al. (2022)

posits that the type of AGN observed depends on three key factors: the viewing angle, the presence or absence of a significant relativistic jet, and the rate of accretion onto the central supermassive black hole. Specifically, the viewing angle determines whether or not the dusty torus surrounding the AGN is visible, which in turn affects the observed characteristics of the AGN. The presence of a significant jet, whether it be RL or RQ, also has an impact on the observed properties of the AGN. The rate of accretion onto the central black hole determines not only the overall electromagnetic power of the AGN, but also the broad band shape of the spectrum, which are of key factors that affect the observed characteristics of these sources. The black hole mass also can impact the rate of accretion onto the central black hole, which in turn affects the overall electromagnetic power of the AGN and its observed characteristics. It can also impact the formation and properties of the relativistic jet, which is another important factor in the orientation unified scheme of AGNs. But the role of black hole mass can be embedded in the accretion rate if the rate is expressed dimensionless.

Referred to figure 1.2, apart from division into RL (upper part) and RQ (lower part), they can be also divided into low (left hand side) and high (right hand side) electromagnetic power.

RL sources can be then classified into two main categories based on their spectral characteristics and the properties of their radio emission: low excitation radio galaxies (LERGs) and high excitation radio galaxies (HERGs). LERGs are often referred to by several other names, including hot mode, radio mode, jet mode, and radiatively inefficient sources. These AGNs are characterized by their low level of optical and ultraviolet emission and are thought to be fueled primarily by the accretion of hot gas onto the central supermassive black hole. HERGs, on the other hand, are also known as cold mode, quasar mode, radiative mode, and radiatively efficient sources. These AGNs are characterized by their high level of optical and ultraviolet emission and are thought to be fueled primarily by the accretion of cold gas or material from a surrounding disk onto the central black hole. HERGs are considered to be more luminous than LERGs, and they are thought to be the counterparts of the bright and highly-energetic quasars that are seen in the universe.

RQ sources also can be then divided into two classes of low power (Seyfert galaxies) and high power (QSOs), however, Seyfert galaxies can also be called as moderate power sources compared to less bright sources such as Sgr A*. It is also notable that RQs should not be confused with radio-silent sources as several galaxies emit low-level radio emission that are not substantially higher than those produced by star-formation. As a result, it is unclear whether these galaxies host radio jets or not. Overall, the lowest luminosity sources are not accommodated in this sketch and it can be the case for sources with luminosity above one percent Eddington luminosity.

Some of the most frequently utilized names for diverse types of AGN, such as broad-line radio galaxy (BLRG), narrow-line radio galaxy (NLRG), narrow emission line galaxy (NELG), flat-spectrum radio quasar (FSRQ), steep-spectrum radio quasar (SSRQ), optically violent variables (OVV), and quasi-stellar objects (QSO) are incorporated into this sketch. The schematic around the central part indicates whether a specific combination of power, radio emission, and geometry is anticipated to produce broad or narrow emission lines, or MIR, radio, X-ray, or gamma-ray radiation. The degree of transparency in each ring corresponds to the increasing intensity or occurrence of a specific emission type.

The term "quasar" and "QSO" (Quasi-Stellar Object) are mostly used interchangeably in astronomy, and they both refer to a type of active galactic nucleus (AGN) that emits a tremendous amount of energy across the electromagnetic spectrum. However, traditionally, astronomers have used the term "quasar" to refer to AGNs that emit strong radio waves, while "QSO" has been used to refer to AGNs that emit little or no radio waves. So, in this sense, a quasar is considered to be a type of RL AGN, while a QSO is classified as RQ. In recent years, however, as astronomers have refined their understanding of AGNs, this distinction between quasars and QSOs has become less clear. Nowadays, the two terms are often used interchangeably to refer to any AGN that emits an enormous amount of energy and has a compact, point-like appearance in the sky.

In the following we concentrate on RQ sources with $\lambda_{\mathrm{Edd}} > 1\%$, dominated by optical/UV. Such objects belong to Seyfert 1/QSO class. Then, for simplicity, we refer to all of the as QSO.

AGNs populate nearby Universe starting from tens of Mpc up to large cosmological redshifts. They can be thus used as a probes of the Universe expansion, which became important due to recent problems with the standard cosmological model of ΛCDM, known as Hubble tension, which is addressed in the next section.

1.1.3 Hubble tension and the role of AGNs

The Hubble tension refers to the discrepancy between the value of the Hubble constant, which measures the current rate of expansion of the universe, obtained from local measurements and that obtained from observations of the cosmic microwave background (CMB) radiation. It has been the subject of ongoing investigation and debate in the astronomical community. The first measurements of the Hubble constant were made in the 1920s and 1930s using observations of nearby galaxies. These early measurements, such as those by Edwin Hubble in 1929, yielded values of the Hubble constant in the range of 500-1000 km/s/Mpc (Hubble, 1929). Georges Lemaître in 1927 (Lemaître, 1927, 1931) measured an estimated value for the proportionality constant even earlier than Hubble due to which the expansion law is currently known as Hubble-Lemaitre law. Subsequent observations and improvements in distance-measuring techniques, such as the Cepheid variable method and the Tully-Fisher relation, reduced the uncertainty in the Hubble constant and led to a more accurate value of about 75 km/s/Mpc by the 1990s (Sandage & Tammann, 1990; Tully & Fisher, 1977). In the late 1990s, the value of Hubble constant inferred from the cosmic microwave background became possible with the launch of the COBE satellite. The CMB provides a snapshot of the universe when it was about 380 k yrs old and its temperature can be used to determine the average density and expansion rate of the universe at that time. The first measurements from the CMB, made by the COBE satellite (Bennett et al., 1996), yielded a value for the Hubble constant of about 50 km/s/Mpc. Subsequent observations from the WMAP satellite (Spergel et al., 2003) and the Planck satellite (Planck Collaboration et al., 2016) have refined the measurement of the Hubble constant from the CMB and currently yield a value of about 67 km/s/Mpc. On the other hand, local measurements of the Hubble constant using supernovae type Ia and the distance ladder based on Cepheid variables (e.g., Riess et al., 2019) have not changed significantly and still yield a value of about 74 km/s/Mpc, though the value measured using the calibration of the supernovae Ia with the tip of the red giant branch (Freedman et al., 2020) yielded a value around 70 km/s/Mpc. Possible explanations for the discrepancy include systematic errors in the measurements or new physics beyond the standard model of cosmology, such as the presence of time-dependent (redshift-dependent) dark energy replacing the cosmological constant, or a modification to general relativity (Di Valentino et al., 2021; Di Valentino, 2021). In recent years, new measurements of the Hubble constant using independent methods, such as the late-time cosmic expansion rate (Riess et al., 2020), have also been made, and these measurements generally agree with the local measurements. This agreement provides strong support for the accuracy of the local measurements and suggests that the Hubble tension is a real and significant discrepancy in our current understanding of the expansion of the universe. The Hubble tension is a critical and unresolved issue in cosmology that represents an active area of research and investigation. Further measurements and improvements in both local and CMB techniques will be crucial in resolving the discrepancy and advancing our understanding of the universe. The implications of the Hubble tension are not yet fully understood, but it has far-reaching consequences for our understanding of the universe.

On the other hand, AGNs represent a promising new tool for cosmology, owing to their abundance and broad range of redshifts, spanning from nearby sources 10 Mpc away to quasars at redshift 6. However, utilizing AGNs as a cosmological tool is a more intricate process, with multiple independent methods available for use (as detailed in Czerny et al., 2018). Quasar-based methods were already used to address the issue (see e.g., Czerny et al., 2013; Risaliti & Lusso, 2019; Lusso, 2020; Shajib et al., 2020; Wong et al., 2020; Sacchi et al., 2022). However, the method based on BLR does not yet

reach that stage but it may in the nearest future.

1.2   Broad Line Region

The BLR is important for several reasons. First, it provides a means of determining the masses of the central black holes in AGN (for a recent review see, Baron & Ménard, 2019). Since the velocity of the gas in the BLR is virialized dominated by gravitational potential of the black hole, hence mass of the black hole can be dynamically estimated using the Keplerian scaling $M_{\mathrm{BH}} \propto R\Delta V^2$, where M_{BH} is the black h ole mass, R is the radial distance of the BLR from black hole, and ΔV is the velocity dispersion of the gas clouds which is proportional to the width of the broad emission lines (Marconi et al., 2008; Netzer & Marziani, 2010; Reines & Volonteri, 2015). Second, the broad emission lines in the BLR spectrum can be used to probe the physical conditions in the region, such as the density, temperature, and chemical composition of the gas. Finally, the BLR is also thought to play a role in regulating the accretion process onto the black hole, as it may help to absorb and re-emit some of the high-energy radiation emitted by the accretion disk, and may partially have a form of efficient winds.

The study of the BLR is challenging because of its small size and its proximity to the central black hole. Only in three sources the BLR was marginally resolved using the IR interferometry with GRAVITY instrument: 3C 273 (GRAVITY Collaboration et al., 2018), IRAS 09149-6206 (GRAVITY Collaboration et al., 2020), NGC 3783 (GRAVITY Collaboration et al., 2021). However, advances in observational techniques, such as reverberation mapping (RM), have made it possible to study the BLR in detail in many other sources and to gain insight into the structure and properties of this important component of AGN. The RM technique involves measuring the time delay caused by the light-travel time between variations in the continuum emission from the accretion disk around the SMBH and the corresponding variations in the emission lines from the BLR. By measuring the time delay, one can determine the size (location) of the BLR, which is related to the mass of the SMBH, as well as the velocity dispersion and structure of the BLR (Peterson & Gaskell, 1991; Peterson et al., 1993; Kaspi et al., 2000; Bentz et al., 2022). The technique has been successfully used in studying the BLR in many AGNs (over 200 objects so far), including quasars and radio galaxies. Reverberation mapping has been used to make some of the most accurate measurements of SMBH masses to date (e.g., Grier et al., 2013), and has also provided insights into the dynamics and physics of the BLR (e.g., Bentz et al., 2009, 2013).

The optical/UV spectrum of a typical quasar, as partially decomposed shown in figure 1.3, usually consists of many different components including continuum emission from the disk forming a power law and emission lines, especially Balmer lines which are due to reprocess and re-emission of the inner disk radiation as well as corona emission by circumnuclear moving material. Doppler broadening of emission lines in the spectra of AGNs as a result of velocity dispersion due to kinematics of those moving material ($\Delta\lambda/\lambda = v/c$) is usually a blend of two components of narrow and broad with widths of order of few hundred km/s and up to 10^4 km/s, respectively (Kollatschny & Zetzl, 2011). The regions where the moving material produces narrow and broad emission lines are called Narrow Line Region (NLR) and Broad Line Region (BLR).

The lines are frequently observed in the form of single-peaked (mostly in high accretion rates) and double-peaked (for low accretion rates) emission line profiles (Osterbrock & Mathews, 1986). These broad lines are further divided into two main types of High Ionization Lines (HIL) emitted by
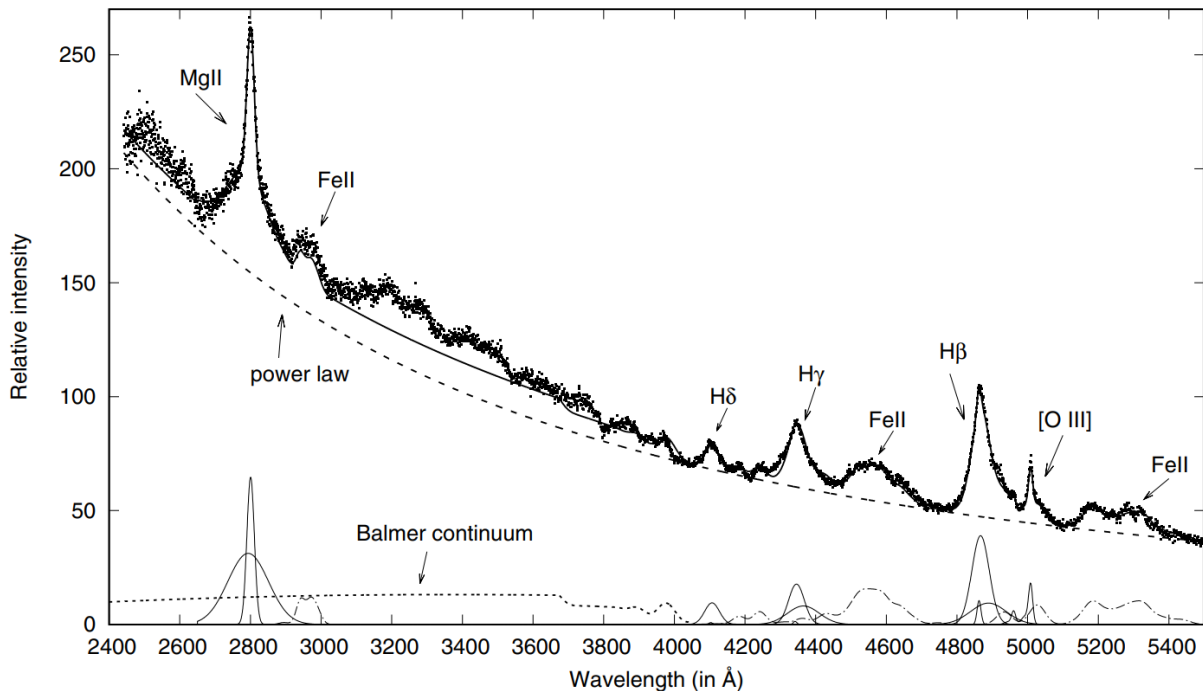
Figure 1.3: Representative UV-optical spectrum of a typical type 1 QSO from SDSS (Kovačević-Dojčinović et al., 2017). The power law represents the continuum from the accretion disk. The FeII pseudo-continuum and also some emission lines including strong Balmer lines, MgII from BLR, and OIII narrow lines are visible.

hotter and lower-density clouds, and Low Ionization Lines (LIL) originating from cooler, denser clouds located further away from the central black hole than HIL medium (Collin-Souffrin et al., 1988). The measured time delays are shorter for HIL lines like HeII and CIV, while LIL represented by Balmer lines and the MgII emission show longer delays, indicating a stratification of the emission with the ionisation degree (Peterson & Wandel, 1999; Zajaček et al., 2021).

Observations indicate that the circumnuclear moving material giving rise to formation broad emission lines are clumpy (Markowitz et al., 2014; Armijos-Abendaño et al., 2022), most likely due to thermal instability (Risaliti et al., 2011; Pietrini et al., 2019). Recent advanced simulations address the issue of cloud formation in such a wind due to thermal instability (Waters et al., 2022). The BLR material is most likely expected to originate from the disk due flat geometry implied from observations (see e.g., GRAVITY Collaboration et al., 2018, 2021).

1.2.1 Proposed models for BLR

There have been many attempts over the last 50 years to explain the formation of BLR under different scenarios. Different models have been proposed to explain the origin of the BLR material, and dynamics of BLR clouds in a theoretical context, but the origin of the BLR remains uncertain. Modelling efforts could be divided into dynamics-oriented and line emission-oriented, with a slow progress towards a unified approach.

Initially, researchers attempted to explain the emission line formation by assuming a random spherical distribution of clouds in Keplerian motion and concentrating on the photoionization equilibrium (Kraemer & Harrington, 1986; Ferland et al., 1998; Kaastra et al., 2004; Goad et al., 2012; Ferland et al., 2017). The history of photoionization modeling of BLR in AGNs dates back to the 1970s, when

it was first proposed that the BLR is a region of photoionized gas surrounding the central accreting black hole. One of the earliest photoionization models of the BLR was presented by Osterbrock (1978); Ferland & Osterbrock (1986). They found that the observed emission line spectrum could be reproduced by a model with a single value of the photoionization parameter. This ionization parameter, U, is defined as the ratio of ionizing photon density to gas density. Since then, photoionization modeling of the BLR has become a standard technique in the study of AGN, with many advances in both the modeling codes and observational data. Since the detailed modelling implied a range of densities in the BLR, Baldwin et al. (1995) presented a model of the BLR based on the concept of a "locally optimally emitting cloud" (LOC), which assumed that the gas in the BLR is clumpy, covers a range of distances, and at each distance there are clouds of different densities. All distributions are described assuming power law dependence on radius and local density. This model can reproduce the observed emission line profiles and variability of AGN. Another important development was the inclusion of X-ray ionization in photoionization models, which is important for AGN with a strong X-ray component. This was first done by Korista & Ferland (1998), who showed that X-ray ionization can explain the observed variability of the BLR in NGC 5548. However, this approach has not been consistently sufficient to explain the BLR formation mechanism and dynamics (Capriotti et al., 1980).

Parametric models are general attempts to the modelling of the BLR based on simple assumptions about the geometry and kinematics of the gas clouds. For example, in an early study in this context by Mardaljevic et al. (1988), in order to explain the broad emission lines in AGNs, radially outflowing clouds from a Keplerian disk are just assumed without addressing a mechanism that can give rise to their formation and geometry. These models generally feature diverse geometries such as rings, disks, shells, and cones filled with clouds (Netzer & Laor, 1993). The density of clouds within the BLR follows a particular function (Adhikari et al., 2018) and their physical properties are parameterized to optimize the emission line shape and the corresponding time-delay maps (Pancoast et al., 2014). These models can provide quantitative constraints on the dynamics and geometry of the BLR (Li et al., 2013) or infer the transfer function (Krolik & Kriss, 1995), however, may not reflect the true physical conditions. As such, they should be used with caution, and their results should be interpreted in the context of the limitations and assumptions of the model being used.

As for the dynamics-oriented aspect, magnetically driven winds have been first proposed as a generic outflow wind solution. The concept of magnetically driven winds was first proposed by Blandford & Payne (1982) to explain the jet formation in some AGN, followed later by others (Konigl & Kartje, 1994; Everett & Murray, 2007). Such magnetically driven outflow can originate at any disk radius, so it can explain both the jet phenomenon as well as the outer dusty torus and X-ray absorption features (Elitzur & Shlosman, 2006). One of the main advantages of magnetically driven winds is that they can naturally explain the observed variability of the BLR, as the wind is driven by the accretion disk and can respond to changes in the disk's ionizing radiation flux. Additionally, magnetic fields are known to play a key role in many astrophysical processes, so it is not unreasonable to expect them to be important in AGN as well. However, this mechanism is based on assumption of the existence of global magnetic field. There are also some potential disadvantages to using magnetically driven winds to model the BLR. One issue is that the models are often complex and computationally expensive, as they require detailed calculations of the magnetic field structure and the interaction between the wind and the accretion disk (Li & Cao, 2022). Additionally, the models often require a number of free parameters related to the global magnetic field and unconstrained by the data, which can make

it difficult to accurately constrain the physical conditions of the BLR.

In another model, Begelman et al. (1983) suggested that the irradiation of the outer disk by the central source to the Inverse Compton temperature could give rise to the formation of thermally-driven winds, which could also be the origin of the BLR. This required additional elements to be assumed, such as a hot corona above the disk or an inner hot flow (Czerny & King, 1989; Witt et al., 1997; Blandford & Begelman, 1999).

Radiatively line-driven mechanism, although initially developed by Castor et al. (1975) to address the stellar winds, was also used as a the most attractive scenario for BLR formation as winds emerging from the accretion disk in AGNs and first studied in this regard by Murray et al. (1995); Murray & Chiang (1997). These are the first papers which combined the physically dynamical approach with the computations of the emission line profiles emerging from the wind. The mechanism works based on the fact that resonance line absorption in an accelerating flow could be significantly more efficient than electron scattering. Following the study by Murray et al. (1995); Murray & Chiang (1997), the principle underwent through numerous tests in AGNs with semi-analytical and also hydrodynamical simulations with varying initial conditions, and these models have shown that winds can be generated for a broad range of black hole masses and accretion rates, and it has been particularly successful at predicting the HIL formation (Proga et al., 2000; Proga & Kallman, 2004; Risaliti & Elvis, 2010; Higginbottom et al., 2014; Waters & Proga, 2016; Waters et al., 2016).

There are also other models such as inflow models (Done & Krolik, 1996; Wang et al., 2017), and disk instabilities (Collin & Zahn, 1999; Wang et al., 2011, 2012). But, dust-driven models are the new and last resorts in this context in which the possible presence of dust in AGN black hole accretion disks and in BLR motivated researcher to examine the possible formation of BLR due to radiation pressure of accretion disk acting on dusty material. In the following, in section 1.2.2, I review the literature hinting on the presence of dust especially in BLR, and then the models of BLR based on dust in section 1.2.3.

1.2.2 Dust in BLR

The existence of dust in the BLRs of AGNs has been a topic of debate among astronomers for many years. For old reviews, see e.g., (MacAlpine, 1985; Goodrich, 1995).

The detection of significantly lower Lyα and ultraviolet line to Balmer line ratios than expected in Seyfert 1 galaxies and quasars by Baldwin (1977), subsequently confirmed by multiple researchers, prompted an increased concern about the potential impact of reddening. Moreover, the International Ultraviolet Explorer satellite data revealed that dust in active galaxies may possess extinction properties different from those found in the interstellar medium in our Galaxy, especially with respect to the potential absence of a notable 2200Å feature (Neugebauer et al., 1980). Additionally, it was observed that continuous spectra of quasars could not be explained entirely by simple power laws (Richstone & Schmidt, 1980). Thus, it was realized that arguments against quasar reddening based on apparent continuum characteristics might not be valid. Shuder & MacAlpine (1977, 1979); Baldwin et al. (1978); Netzer & Davidson (1979) all identified specific line ratios that indicated considerable differential extinction due to dust in the line of sight, while London underscored the possibility of dust destroyed by trapped Lyα emission.

There is also another compelling evidence for the presence of dust in AGNs that has been revealed through polarization and infrared observations. In certain Seyfert 1s and BLRGs, the comparable

polarization of both emission lines and underlying continuum has been attributed to either dust scattering or transmission, as demonstrated by different researchers (Thompson et al., 1980; Martin et al., 1982; Rudy et al., 1983, 1984). Moreover, Rudy et al. (1983) found a relationship between measured polarizations and broad line Balmer decrements, and many AGNs display an apparent rise in continuum polarization towards shorter wavelengths, which may indicate the presence of dust scattering. However, Miller & Antonucci (1983) warned that the perceived increase in polarization towards blueward wavelengths could also result from dilution by unpolarized starlight. Although Antonucci (1984); Antonucci & Miller (1985) have proposed that electron scattering is responsible for the observed polarization of lines and non-stellar continuum in the BLRG 3C 234 and the Seyfert 2 galaxy NGC 1068 (Angel et al., 1976), this interpretation may apply to other AGNs as well. Nevertheless, several of these AGNs exhibit signs of dust besides polarization.

In the 1970s and 1980s, the study of AGN broad emission lines became more sophisticated, and it was discovered that the lines showed a range of asymmetries and profiles that could not be explained by simple models of the emitting gas. It was proposed that this could be due to the presence of dust in the BLRs (Netzer, 1987). The question of the exact location of the dust in AGN remained a matter of debate for many years. It was initially thought that the dust was located in a torus-shaped structure surrounding the central black hole, but later observations suggested that the dust could also be present closer to the central engine, in the BLRs or even in the accretion disk itself. (Kraemer & Harrington, 1986; Maiolino et al., 2001b,a; Suganuma et al., 2006).

The exact role of dust in the BLRs and its effects on the observed properties of AGN are still a subject of active research (Ilić et al., 2012; Shablovinskaya et al., 2020). The broad hydrogen Balmer emission line ratios observed in AGN are not consistent with simple theoretical predictions, and the presence of dust has been proposed as a possible explanation (Ilić et al., 2012). In general, a medium that is exposed to the central flux in AGN cannot remain dusty at distances smaller than the torus inner radius. However, the disk in AGN is geometrically thin, and its inner part, or winds, may shield the disk and allow dust to survive close in. Measurements of the time lag between the non-polarized continuum and polarized broad line variability in Mrk 6 have indicated the presence of a scatterer much closer than the torus but further away than the BLR (Shablovinskaya et al., 2020). Another important fact is that broad lines coexist with a cold disk located much closer to the torus than previously thought. Several studies (Rees et al., 1969; Rieke, 1978; Barvainis, 1987; Dong et al., 2008) also suggest that there might be dust present in the outer regions of an accretion disk. This cold disk contains low-ionized material with dust, as the effective temperature of the accretion disk drops below 1000 K (Czerny et al., 2004; Loska et al., 2004).

These facts motivated the development of the radiatively dust-driving models for the BLR which is the subject of the section 1.2.3 below.

1.2.3 Dust-based models for BLR

A decade ago, Czerny & Hryniewicz (2011) showed that dust can form at large radii of accretion disk where the disk effective temperature drops below the order of 1000 K, thus proposed a non-adhoc physically-motivated fully-analytical one-dimensional (1D) model based on radiatively dust-driving mechanism to explain the LIL part of BLR. In this model, a dusty wind is initiated from the disk due to disk radiation pressure but finally falls back onto the disk, hence the model is called FRADO (Failed Radiatively Accelerated Dusty Outflow). The FRADO model directly predicts the inner/outer radius
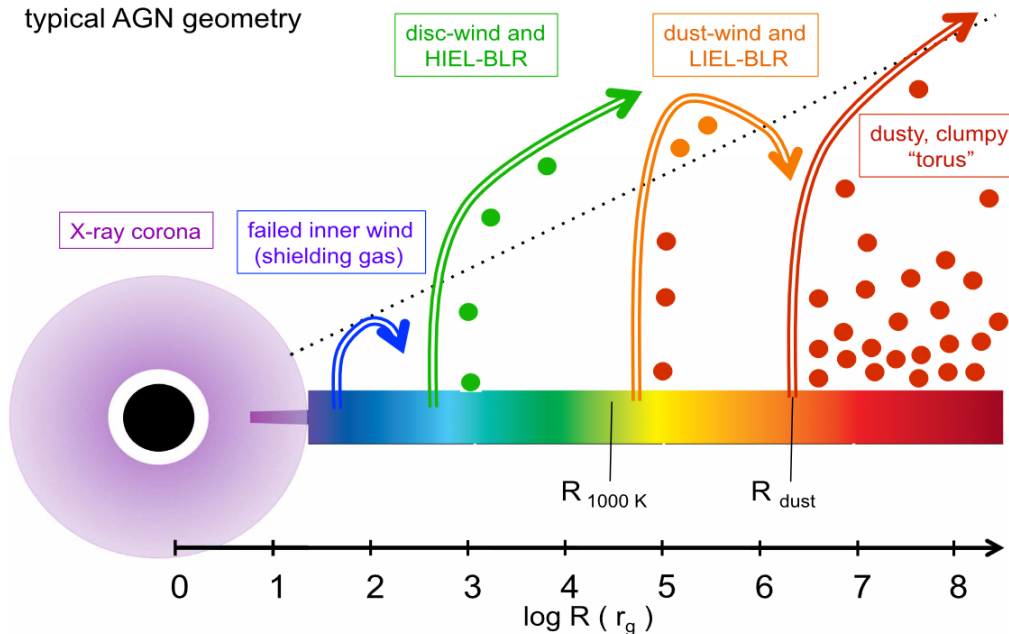
Figure 1.4: A typical geometry of a quasar adopted from Miniutti et al. (2013).

of LIL-BLR, asymmetry in line profiles (due to dust evaporation); observationally consistent line shape parameter FWHM/σ, the dependence of virial factor on black hole mass, and most importantly the radius-luminosity (RL) relation (Czerny et al., 2015, 2016, 2017).

Later, Baskin & Laor (2018) developed another model in which a static disk is just puffed-up due to irradiation in the dust-dominated region. According to Czerny et al. (2015), the Planck mean opacity in the upper region of the accretion disk atmosphere is significantly higher than the Rosseland mean opacity used in the interior of the disk. This results in the lack of hydrodynamical balance in the optically thin surface layers of the disk, and indicates that the larger Planck value, appropriate for wind-driving, inevitably causes an outflow launching, even though a failed wind (For a recent review on radiation-driven accretion disk winds see Giustini & Proga, 2019). In contrast, Baskin & Laor (2018) only utilized a static solution and were unable to capture the potential for strong winds to form from the disk at high accretion rates. Although they acknowledged this possibility, their static analysis could not account for this feature. In a typical geometry of a quasar as shown in figure 1.4, formation of low-ionized broad emission line with a single-peaked profile is expected only if a wind, even a failed wind, is formed. Irradiated static disk surface in the model of Baskin & Laor (2018) usually leads to double-peaked line profiles. There is also another model in the context of dust-driving mechanism by Dorodnitsyn et al. (2016), though appropriate for the outer disk and dusty torus. However, later Dorodnitsyn & Kallman (2021) developed an extension of the static model of Baskin & Laor (2018) that includes a convective component responsible for launching an outflow from the disk.

The basic model of FRADO, however, is 1D fully analytical in which the flux is very local and constant with height, shielding effect is neglected, radiation from other radii is neglected in motion, the motion is only described in the vertical direction and radial motion is neglected, a wavelength-averaged dust opacity is used, and the full picture of LIL-BLR is in the form of failed wind (no signature of outflow), but the successful predictions of the model motivated the development of a more comprehensive model, accounting for the full 3D geometry of AGNs. During my PhD I developed the 2.5D numerical non-hydrodynamical FRADO code to simulate the dynamics of material in low

ionized BLR. The code incorporates the realistic prescription of extended disk radiation field, advanced values of wavelength-dependent dust opacities (Szczerba et al., 1997; Röllig et al., 2013), dynamical dust sublimation process and shielding effect (Murray et al., 1995). It shows that cloud motion is rather complex and strongly depends on the parameters like black hole mass, accretion rate, viewing angle towards the nucleus, and the metallicity of material. It successfully explains many observational dynamical features of LIL-BLR, as presented in Paper I. For example, it predicts formation of an outflow structure similar to empirical picture of Elvis (2000). Successful test of the model with the observationally-established radius-luminosity relation in AGNs also confirms its predictive power, as detailed in Paper II. The model can consistently recover the shape of low-ionized emission line profiles of AGNs, hence serves as an appropriate model to account for LIL-BLR, as addressed in Paper III.

1.3 Thesis overview

In my thesis I focus on the dynamical nature of the broad line region (BLR) in active galaxies through a numerical approach based on dust driving mechanism. The BLR is a nuclear region of most active galaxies, characterized by broad emission lines in the optical/UV spectra produced due to complex motion of material. The precise dynamics of the BLR as an open question, with observations indicating a largely Keplerian motion alongside possible traces of inflow or outflow, seems to be unfolded at least for the low ionized part, from the point of view of my thesis that presents a comprehensive investigation into the BLR dynamics through radiation pressure acting upon dust present at the surface layers of the accretion disk at large radii. To do so, I developed the 2.5D numerical version of the FRADO model with non-hydrodynamical single-cloud approach to the dynamics of BLR which is addressed in Chapter 2, and Paper I. In this paper, I showed that the radiation pressure exerted upon dusty clouds is potent enough to cause a dynamical (mostly failed) outflow from the surface of the accretion disk. The overall dynamics of BLR in this model is very complex, consisting of two parts of failed winds and outflow. The dynamics is strongly influenced by the Eddington ratio of the source. Ultimately, the cloud dynamics serves as the principal determinant of the three-dimensional geometry of the BLR. In Paper II, I performed a preliminary test of the model with the observationally-established radius-luminosity relation in AGNs. It shows that the model with different values of accretion rate and adjusting the shielding effect can explain the most recent sample of reverberation measured Hβ time-delays which includes the spread over the phenomenological relation with respect the Eddington ratio of the source. In Paper III, I tested the model with calculations of the spectral line generic profiles, using a large grid of results from the 2.5D FRADO numerical code. I conducted an analysis of the impact of various parameters, including accretion rate, black hole mass, viewing angle, and dust-to-gas mass ratio, on the shape of the spectral line profiles. The results demonstrate that the spectral line profiles are significantly influenced by the dust-to-gas mass ratio, which regulates the strength of the radiation pressure. They also show that the 2.5D FRADO model can appropriately explain the low-ionized broad emission lines, such as MgII and Hβ, observed in quasars mean spectrum.

Overall, the thesis presents a novel dust-based approach to understanding the dynamics of the BLR in active galaxies. The thesis findings highlight the significant role of radiatively dust-driving mechanism in shaping the BLR dynamics, and the importance of metalicity, or dust-to-gas mass ratio in determining the spectral line profiles. These findings provide valuable insights into the physics of active galaxies and contribute to the broader understanding of these fascinating astrophysical objects.

Chapter 2

FRADO in 2.5D: Calculations & Setup

2.1 Radiation pressure

Specific (radiative) intensity is a quantity used in physics that describes electromagnetic radiation. It is a term used in much of the older scientific literature. The present-day SI term is spectral radiance, which can be expressed in base SI units as W m^{-2} sr^{-1} Hz^{-1}.

In terms of the spectral radiance, I_ν, the energy flowing across an area element of dA, located at $\mathbf{r}$ in time dt, in the solid angle $d\Omega$ about the direction $\hat{\mathbf{n}}$ in the frequency interval ν to $\nu + d\nu$ is

$$dE_\nu = I_\nu(\mathbf{r}, \hat{\mathbf{n}}, t) \ \cos(\alpha) \ d\nu \ dA \ d\Omega \ dt \tag{2.1}$$

where α is the angle that the unit direction vector $\hat{\mathbf{n}}$ makes with a normal to the area element $\hat{\mathbf{n}}_A$.

It can alternatively expressed in terms of wavelength as

$$dE_\lambda = I_\lambda(\mathbf{r}, \hat{\mathbf{n}}, t) \ \cos(\alpha) \ d\lambda \ dA \ d\Omega \ dt \tag{2.2}$$

The solid angle defines as

$$\Omega = \int_B \frac{\hat{\mathbf{n}}_B \cdot \hat{\mathbf{n}}}{s^2} dB = \int_B \frac{\cos(\beta) \ dB}{s^2} \tag{2.3}$$
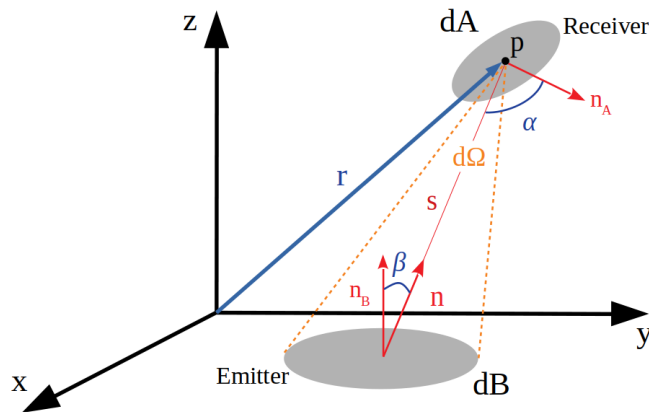

Figure 2.1: The geometry for the definition of specific (radiative) intensity.
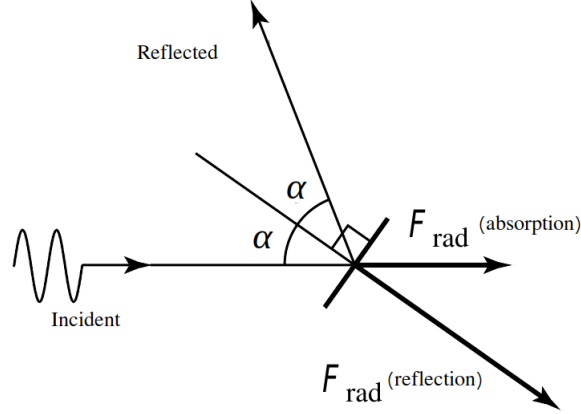
Figure 2.2: Components of radiative force.

So one can write

$$dE_\lambda = I_\lambda(\mathbf{r}, \hat{\mathbf{n}}, t) \; \frac{\cos(\alpha) \; \cos(\beta)}{s^2} \; d\lambda \; dA \; dB \; dt \tag{2.4}$$

Then the differential amount of radiation flux from the solid angle $d\Omega$ is

$$dF_\lambda = \frac{dE_\lambda}{d\lambda \; dA \; dt} = I_\lambda(\mathbf{r}, \hat{\mathbf{n}}, t) \; \cos(\alpha) \; d\Omega \tag{2.5}$$

so the monochromatic radiation flux reads

$$F_\lambda = \int I_\lambda \; \cos(\alpha) \; d\Omega \tag{2.6}$$

or, equivalently, the total flux as

$$F = \int I \cos(\alpha) \; d\Omega \tag{2.7}$$

To get the flux of radiation momentum (momentum per unit time per unit area = radiation pressure), using the definition of photon's momentum in Relativity, i.e. $p = E/c$, we have

$$P_{rad} = \text{flux of momentum} = \frac{\text{flux of energy}}{c} \tag{2.8}$$

or

$$P_{\text{rad}} = \frac{1}{c} \int I_\lambda \; \cos(\alpha) \; d\Omega \; d\lambda \tag{2.9}$$

According to the figure 2.2, the radiation pressure can be expressed in two ways depending on whether the light is reflected from or absorbed by the surface.

1) If the light is completely **absorbed**, then the force due to radiation pressure is in the direction of the light's propagation and the equation 2.9 remains unchanged.

2) If the light is instead completely **reflected**, then the radiation pressure force must act in a direction perpendicular to the surface which requires one more factor of $\cos(\alpha)$, that is the component of radiation pressure parallel to the surface cannot exert a force. A factor of 2 is also needed due to conservation of momentum. Therefore the radiation pressure takes the form

$$P_{\text{rad}} = \frac{2}{c} \int I_\lambda \; \cos^2(\alpha) \; d\Omega \; d\lambda \tag{2.10}$$

If the effective cross section of the irradiated object is always perpendicular to $\hat{\mathbf{n}}$, the radiation

pressure is then given as

$$P_{\text{rad}} = \frac{1}{c} \int I_\lambda \; d\Omega \; d\lambda \qquad \text{(full absorption)} \tag{2.11}$$

$$P_{\text{rad}} = \frac{2}{c} \int I_\lambda \; d\Omega \; d\lambda \qquad \text{(full reflection)} \tag{2.12}$$

Radiation pressure is something intrinsic to the radiation source and independent of the optical properties of the irradiated object. The radiative force due to the radiation pressure, however, is a function of the optical properties of the irradiated object, that is its scattering and absorption cross-sections. It means that a given object might be fully transparent to the radiation, so that it feels no radiative force acting upon it, regardless of the radiation pressure of the radiation source.

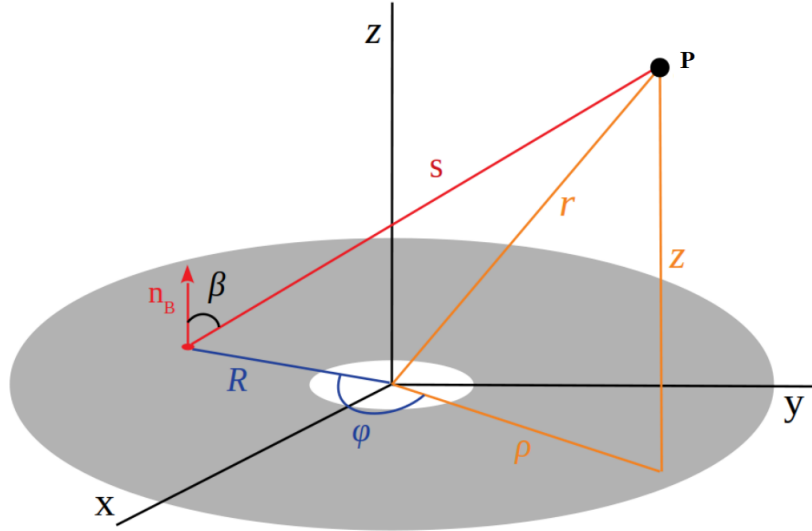## 2.2 Radiative force of an anisotropic disk at an arbitrary point P

Figure 2.3: A particle at **P** under radiation pressure from an emitting extended disk.

Following equations 2.11 and 2.12, the absorption- and scattering-driven radiative force exerted on an infinitesimal object (dA) by an infinitesimal emitter (dB) shown in figure 2.1 can be obtained if simply multiplied by a corresponding cross-section. Therefore one can find the radiative accelerations as

$$\mathbf{a}^{\text{abs}} = \frac{1}{Mc} \int \int I_\lambda \; \sigma_\lambda^{\text{abs}} \; \hat{\mathbf{s}} \; d\Omega \; d\lambda \tag{2.13}$$

$$\mathbf{a}^{\text{sca}} = \frac{2}{Mc} \int \int I_\lambda \; \sigma_\lambda^{\text{sca}} \; \hat{\mathbf{s}} \; d\Omega \; d\lambda \tag{2.14}$$

where M the mass of irradiated object (particle at P), and σ_λ is the cross section of the irradiated object for absorption or scattering which in general is wavelength-dependent. It should be noted that we have put σ_λ rather than dA which means that not only the gradient of radiation pressure across the irradiated object is negligible, but also σ_λ includes the information of reflectivity and absorption efficiency of the irradiated object. It implies that the object is small, for example dust grains with

small values of cross-sections, so the total radiative acceleration of the object is

$$\mathbf{a}_{\text{grain}}^{\text{rad}} = \frac{1}{M_{\text{grain}}} \frac{1}{c} \int \int I_\lambda \ \sigma_\lambda^{\text{rad}} \ \hat{\mathbf{s}} \ d\Omega \ d\lambda \qquad (2.15)$$

where $\sigma_\lambda^{\text{rad}} = \sigma_\lambda^{\text{abs}} + 2\sigma_\lambda^{\text{sca}}$.

Using the definition of solid angle, we consider an extended disk-like radiating surface shown in figure 2.1 in grey where red spot is the area element in polar coordinate, dB, shown in the figure 2.3 and $\hat{\mathbf{n}}_B$ is the unit vector normal to dB. So we have

$$d\Omega = \frac{\cos\beta}{s^2} \ R \ dR \ d\varphi \qquad (2.16)$$

where $\cos\beta = z/s$, and $\hat{\mathbf{s}} = \mathbf{s}/s$. So we have

$$\mathbf{a}_{\text{grain}}^{\text{rad}} = \frac{1}{M_{\text{grain}}} \frac{z}{c} \int \int \int I_\lambda \ \sigma_\lambda^{\text{rad}} \ \frac{\mathbf{s}}{s^4} \ R \ dR \ d\varphi \ d\lambda \qquad (2.17)$$

Knowing that $(\mathbf{s} = \mathbf{r} - \mathbf{R})$, using the below definitions

$$\begin{cases} \mathbf{r} = & \rho & \hat{\rho} + & z & \hat{\mathbf{z}} \\ \mathbf{R} = & R \ \cos\varphi & \hat{\rho} + & R \ \sin\varphi & \hat{\rho}_\perp \end{cases} \qquad (2.18)$$

we can obtain the vector $\mathbf{s}$ and its length as

$$\mathbf{s} = (\rho - R \ \cos\varphi) \ \hat{\rho} - R \ \sin\varphi \ \hat{\rho}_\perp + z \ \hat{\mathbf{z}} \qquad (2.19)$$

$$s^2 = r^2 + R^2 - 2 \ \rho \ R \ \cos\varphi \qquad (2.20)$$

Due to azimuthal symmetry, the summation over the second term of $\mathbf{s}$ would give zero, so we have

$$\mathbf{a}_{\text{grain}}^{\text{rad}} = \frac{1}{M_{\text{grain}}} \frac{z}{c} \int \int \int I_\lambda \ \sigma_\lambda^{\text{rad}} \ \frac{(\rho - R \ \cos\varphi) \ \hat{\rho} + z \ \hat{\mathbf{z}}}{(r^2 + R^2 - 2 \ \rho \ R \ \cos\varphi)^2} \ R \ dR \ d\varphi \ d\lambda \qquad (2.21)$$

for which one can have the components in Cartesian coordinates just using $\hat{\rho} = (x \ \hat{\mathbf{x}} + y \ \hat{\mathbf{y}})/\rho$.

This gives the net radiative acceleration for a single grain of a specific size and certain type of material. But for a dusty clump, i.e. a distribution of dust particles (with different material and different size) embedded in and strongly coupled with a volume of gas, the radiative acceleration can be obtained by summation over the type and size of dust particles as below

$$\mathbf{a}_{\text{clump}}^{\text{rad}} = \frac{1}{M_{\text{clump}}} \frac{z}{c} \int \int \int I_\lambda \ \sigma_\lambda^{\text{tot(rad)}} \ \frac{(\rho - R \ \cos\varphi) \ \hat{\rho} + z \ \hat{\mathbf{z}}}{(r^2 + R^2 - 2 \ \rho \ R \ \cos\varphi)^2} \ R \ dR \ d\varphi \ d\lambda \qquad (2.22)$$

where $M_{\text{clump}} = M_{\text{dust}} + M_{\text{gas}}$.

2.3 Dust modelling

In order to find $\sigma_\lambda^{\text{tot(rad)}}$, assuming a dust model with a population of dust types with a given grain size distribution, we proceed with a general relation valid for grains with radius $a_- \leq a \leq a_+$ as below

$$dn_i(a) = nf_i(a) \ da = n_i(a) \ da \tag{2.23}$$

where $n_i(a)$ is the number-density of grains of the chemical composition i, n is the number-density of H nuclei ($n = n_H + 2n_{H_2}$), and f_i is a modular function. Now one can write for example the total absorption cross-section (the same applies to total scattering cross-section) for a given dust sort as

$$\sigma_{\lambda,i}^{\text{tot(abs)}} = V_{\text{clump}} \int_{a_-^i}^{a_+^i} n_i(a) \ [\sigma(a)]_{\lambda,i}^{\text{abs}} \ da \tag{2.24}$$

where $[\sigma(a)]_{\lambda,i}^{\text{abs}}$ is the absorption cross-section of a single grain of a certain sort of size a (radius) at wavelength λ, and V_{clump} is the volume of the clump. Summation over sorts of dust gives

$$\sigma_\lambda^{\text{tot(abs)}} = \sum_{i=1}^{\text{NDS}} \sigma_{\lambda,i}^{\text{tot(abs)}} = V_{\text{clump}} \sum_{i=1}^{\text{NDS}} \int_{a_-^i}^{a_+^i} n_i(a) \ [\sigma(a)]_{\lambda,i}^{\text{abs}} \ da \tag{2.25}$$

where NDS is the number of dust sorts in the dust model. Likewise we can find $\sigma_\lambda^{\text{tot(sca)}}$ and consequently $\sigma_\lambda^{\text{tot(rad)}}$.

When calculating the radiative acceleration, it would be easier to work with general densities, ratios, and mean values rather than certain masses or volumes. Looking at the equation 2.22 we can write

$$\frac{\sigma_\lambda^{\text{tot(rad)}}}{M_{\text{clump}}} = \frac{M_{\text{dust}}}{M_{\text{clump}}} \ \frac{\sigma_\lambda^{\text{tot(rad)}}}{M_{\text{dust}}} = \frac{\Psi}{1+\Psi} \ K_\lambda^{\text{rad}} \tag{2.26}$$

where K_λ^{rad} is the total opacity of the clump given by

$$K_\lambda^{\text{rad}} = K_\lambda^{\text{abs}} + 2K_\lambda^{\text{sca}} \tag{2.27}$$

where

$$K_\lambda^{\text{j}} = \frac{1}{\Psi} \sum_{i=1}^{\text{NDS}} K_{\lambda,i}^{\text{j}} \Psi_i \tag{2.28}$$

where

$$K_{\lambda,i}^{\text{j}} = \frac{\sigma_{\lambda,i}^{\text{tot(j)}}}{M_{\text{dust},i}} = \frac{1}{\rho_{\text{dust},i}} \ \int_{a_-^i}^{a_+^i} n_i(a) \ [\sigma(a)]_{\lambda,i}^{\text{j}} \ da \tag{2.29}$$

where j stands for (rad), (abs), or (sca); and Ψ is dust-to-gas mass ratio given by

$$\Psi = \frac{M_{\text{dust}}}{M_{\text{gas}}} = \frac{\rho_{\text{dust}}}{\rho_{\text{gas}}} = \sum_{i=1}^{\text{NDS}} \Psi_i = \frac{\sum_{i=1}^{\text{NDS}} \int_{a_-^i}^{a_+^i} n_i(a) \ 4/3\pi a^3 \rho_{\text{b},i} \ da}{nm_H} = \frac{\sum_{i=1}^{\text{NDS}} \int_{a_-^i}^{a_+^i} f_i(a) \ 4/3\pi a^3 \rho_{\text{b},i} \ da}{m_H} \tag{2.30}$$

where $\rho_{\text{b},i}$ is the bulk dust density of sort i, and m_H is the mass of H nuclei.

2.4 Radiative acceleration of a dusty clump under the effect of SS disk

Now, following the equation 2.15, the total radiative acceleration of the dusty clump can then be written as

$$\mathbf{a}_{\text{clump}}^{\text{rad}} = \frac{\Psi}{1+\Psi} \frac{z}{c} \int_{\lambda_i}^{\lambda_f} \int_{\varphi_{min}}^{\varphi_{max}} \int_{R_{min}}^{R_{max}} I_\lambda \ K_\lambda^{\text{rad}} \ \frac{(\rho - R \ \cos\varphi) \ \hat{\rho} + z \ \hat{\mathbf{z}}}{(r^2 + R^2 - 2 \ \rho \ R \ \cos\varphi)^2} \ R \ dR \ d\varphi \ d\lambda \tag{2.31}$$

where Ψ is the clump dust-to-gas ratio, and K_λ^{rad} is the mean total cross-section per dust mass which resembles the definition of opacity

As the SS disk emits thermal radiation that follows a blackbody spectrum, we take $I_\lambda = B_\lambda$,

$$B_\lambda(T) = \frac{2hc^2}{\lambda^5} \frac{1}{\exp\left(\dfrac{hc}{\lambda \ k_B \ T}\right) - 1} \tag{2.32}$$

we have

$$\mathbf{a}_{\text{clump}}^{\text{rad}} = \frac{\Psi}{1+\Psi} \ 2hc \ z \iiint \frac{K_{\text{sca}}(\lambda)}{\lambda^5} \frac{1}{\exp\left(\dfrac{hc}{\lambda k_B \ T_{\text{eff}}(R)}\right) - 1} \frac{(\rho - R \ \cos\varphi) \ \hat{\rho} + z \ \hat{\mathbf{z}}}{(r^2 + R^2 - 2 \ \rho \ R \ \cos\varphi)^2} \ R \ dR \ d\varphi \ d\lambda \tag{2.33}$$

For a radiatively efficient disk, the outcoming flux of energy is given by the corresponding formulae of Shakura & Sunyaev (1973) and Novikov & Thorne (1973), which can be used to obtain the radial profile of the effective temperature. For the non-relativistic SS disk it is given as

$$\mathbb{F}(R) = \sigma_{SB} \ T_{\text{eff}}^4(R) = \frac{3GM\dot{M}}{8\pi R^3} \left(1 - \sqrt{\frac{R_{\text{in}}}{R}}\right) \tag{2.34}$$

where R_{in} is the inner radius of the disk defined as

$$R_{\text{in}} = 6 \ r_{\text{g}} = \frac{6GM}{c^2} \tag{2.35}$$

The final form of the radiative acceleration is then given by plugging $T_{\text{eff}}(R)$ from 2.34 into equation 2.33.

2.5 Dust sublimation

Assuming instantaneous re-emission of the absorbed radiation by dust in the form of an isotropic blackbody radiation, if the amount of heat absorbed by dusty content of the clump increases its temperature to that of sublimation, the radiative engine of motion of the clump switches off. So the criterion for sublimation of dusty content is

$$E_{\text{abs}} = E_{\text{emit}}(T_{\text{s}}) \tag{2.36}$$

The total radiative energy by definition is

$$E = \int I_\lambda(\mathbf{r}, \hat{\mathbf{n}}) \ \cos(\alpha) \ d\lambda \ dA \ d\Omega \ dt \tag{2.37}$$

So the radiative energy absorbed by dust is

$$E_{\text{abs}} = \int I_\lambda \; \sigma_\lambda^{\text{tot(abs)}} \; d\lambda \; d\Omega \; dt \tag{2.38}$$

and the energy re-emitted by dust at the sublimation temperature (T_{s}) is

$$E_{\text{emit}}(T_{\text{s}}) = 4\pi \int B_\lambda(T_{\text{s}}) \; \sigma_\lambda^{\text{tot(abs)}} \; d\lambda \; dt \tag{2.39}$$

Dividing both sides of the equation 2.36 by dt and M_{dust} we can introduce Q (the total power per dust mass) so we have

$$Q_{\text{abs}} = Q_{\text{emit}}(T_{\text{s}}) \tag{2.40}$$

as the dust sublimation condition where

$$Q_{\text{emit}}(T_{\text{s}}) = 4\pi \int B_\lambda(T_{\text{s}}) \; K_\lambda^{\text{abs}} \; d\lambda \tag{2.41}$$

$$Q_{\text{abs}} = \int I_\lambda \; K_\lambda^{\text{abs}} \; d\lambda \; d\Omega \tag{2.42}$$

so we have

$$Q_{\text{abs}} = z \int_{\lambda_i}^{\lambda_f} \int_{\varphi_{min}}^{\varphi_{max}} \int_{R_{min}}^{R_{max}} \frac{I_\lambda \; K_\lambda^{\text{abs}}}{(r^2 + R^2 - 2 \; \rho \; R \; \cos\varphi)^{3/2}} \; R \; dR \; d\varphi \; d\lambda \tag{2.43}$$

2.6 Shielding effect

According to radiatively-driven wind models, launching an efficient outflow in not possible if the launching region is not shielded from irradiation by the central source, as firstly modelled by Murray et al. (1995). This issue is discussed in detail in Paper I and Paper II. In our model, we treat the shielding effect through a geometrical proxy. We consider that the cloud is exposed only to the radiation from the small part (a polar patch) of the disk, and the size of the patch is always proportional to the actual height of the cloud. Thus the position and the size of the patch varies as the cloud moves. A cloud very high above the disk is exposed to a large fraction of the disk. This geometry is illustrated in figure 2.4.

In order to include the geometrical treatment of the shielding effect into our computations, equations 2.44 below should be introduced in equations 2.33, and 2.43 as the upper/lower limits of integrals. The ratio of the cloud height to the patch size is determined by a parameter, α, which is fixed during the cloud motion.

$$\begin{aligned}
R_{\text{min}} &= \rho - \alpha z \\
R_{\text{max}} &= \rho + \alpha z \\
\varphi_{\text{min}} &= -\pi \left(\frac{\alpha z}{\rho - R_{\text{in}}} \right) \\
\varphi_{\text{max}} &= \pi \left(\frac{\alpha z}{\rho - R_{\text{in}}} \right)
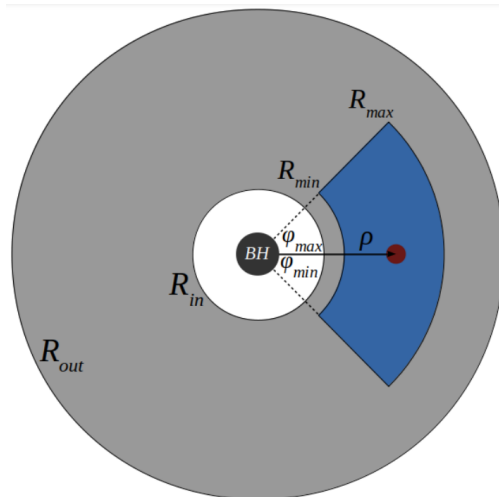\end{aligned} \tag{2.44}$$

.

Figure 2.4: Geometrical proxy for shielding effect.

2.7 General Setup

There are eventually two main forces, i.e. gravity of central black hole and disk radiation pressure acting on a dusty clump.

$$\mathbf{a}_{\text{net}} = \mathbf{a}_{\text{gravity}} + \mathbf{a}_{\text{radiation}} \tag{2.45}$$

where

$$\mathbf{a}_{\text{gravity}} = -\frac{GM_{\text{BH}}\ \mathbf{r}}{r^3} \tag{2.46}$$

and $\mathbf{a}_{\text{radiation}}$ is given by the equation 2.33.

In the 2.5D FRADO model that I developed, the code is fed by the main global parameters of a given source (the black hole mass, accretion rate, and dust-to-gas mass ratio), and it basically solves the equation of motion while the angular momentum at a given cloud orbit is conserved.

The advanced values of wavelength-dependent dust opacities are taken from the code by Szczerba et al. (1997); Röllig et al. (2013). Throughout this thesis the sublimation temperature of dust is kept at 1500 K as in Baskin & Laor (2018). More details on the dust modelling is available in Paper I.

A given cloud in Keplerian motion around the black hole starts its vertical motion under the effect of disk radiation pressure from the disk surface at a given radius which is calculated from the code developed by Różańska (1999); The code gives the one-dimensional shape of accretion disk as a function of radius. At any given step, the condition of dust sublimation, as in equation 2.40, is checked, and if met, the radiative force is switched off, hence there will be only a ballistic motion under the gravity of central black hole.

General relativistic effects are also neglected due large distance of the dust-dominated region of accretion disk from the central black hole.

The dimensions of disk in our computations is as below

$$
\begin{aligned}
R_{\text{in}} &= 6\ r_{\text{g}} &&\text{(inner radius of disk)}\\
R_{\text{out}} &= 10^6\ r_{\text{g}} &&\text{(outer radius of disk)}
\end{aligned}
$$

where r_{g} is the gravitational radius. However, due to shielding effect, only a small polar patch of the disk is eventually considered, the size of which is a function of the location of a lifted cloud.

Chapter 3

Paper I: The picture of BLR in 2.5D FRADO: Dynamics and Geometry

CrossMark

The Picture of BLR in 2.5D FRADO: Dynamics and Geometry

Mohammad-Hassan Naddaf[1,2] , Bożena Czerny[1] , and Ryszard Szczerba[3]
[1] Center for Theoretical Physics, Polish Academy of Sciences, Lotnikow 32/46, 02-668 Warsaw, Poland; naddaf@cft.edu.pl
[2] Nicolaus Copernicus Astronomical Center, Polish Academy of Sciences, Bartycka 18, 00-716 Warsaw, Poland
[3] Nicolaus Copernicus Astronomical Center, Polish Academy of Sciences, Rabianska 8, 87-100 Torun, Poland

Abstract

The dynamics of the broad line region (BLR) in active galaxies is an open question; direct observational constraints suggest a predominantly Keplerian motion, with possible traces of inflow or outflow. In this paper we study in detail the physically motivated BLR model of Czerny & Hryniewicz based on the radiation pressure acting on dust at the surface layers of the accretion disk (AD). We consider here a nonhydrodynamical approach to the dynamics of the dusty cloud under the influence of radiation coming from the entire AD. We use here a realistic description of the dust opacity, and we introduce two simple geometrical models of the local shielding of the dusty cloud. We show that the radiation pressure acting on dusty clouds is strong enough to lead to dynamical outflow from the AD surface, so the BLR has a dynamical character of a (mostly failed) outflow. The dynamics strongly depends on the Eddington ratio of the source. Large Eddington ratio sources show a complex velocity field and large vertical velocities with respect to the AD surface, while for lower Eddington ratio sources vertical velocities are small and most of the emission originates close to the AD surface. Cloud dynamics thus determines the 3D geometry of the BLR.

Unified Astronomy Thesaurus concepts: Galaxy accretion disks (562); Radiative processes (2055); Broad-absorption line quasar (183); Quasars (1319); Astrophysical dust processes (99); Gas-to-dust ratio (638); Active galactic nuclei (16); Active galaxies (17); Reverberation mapping (2019); Supermassive black holes (1663); Galaxy winds (626); Dust continuum emission (412)

1. Introduction

Broad emission lines are the most characteristic features of the optical/UV spectra of most active galaxies. They were the motivation of the study by Seyfert (1943), and they provided the clue to the puzzle of the quasar phenomenon (Schmidt 1963). The intense emission of broad line regions (BLRs) from the X-ray to optical to infrared has been studied for years (Boroson & Green 1992; Lawrence et al. 1997; Reeves & Turner 2000; Sulentic et al. 2000; Gaskell 2009; Le & Woo 2019; Raimundo et al. 2020). These studies rely on the analysis of the spectra and their time dependence because the region is messy, turbulent, and not yet easily spatially resolvable. Line shapes and the photoionization conditions of their formation imply that BLR emission consists of two line categories: high-ionization lines (HIL) and low ionization lines (LIL; Collin-Souffrin et al. 1988). Further research brought a wealth of information on the spatial distribution of the medium, its motion, and the thermal and ionization state of the material (for a detailed review, see Netzer 2013), but did not bring a definite answer to the question of the origin of the material located in the BLR.

The reverberation mapping (RM) approach based on the delayed response of BLR material to variations of the active galactic nucleus (AGN) continuum (Blandford & McKee 1982; Peterson 1993) enabled us to precisely measure the spectral-dependent radius of BLRs (Wandel et al. 1999). It also brought us an insight into the motion of the BLR (Peterson et al. 1998), showing that its dynamics is a composition of a Keplerian motion around the black hole (BH), and a turbulent motion that gives overall a complex velocity field (Shapovalova et al. 2010; Grier et al. 2013).

That said, the presence of observational signatures of inflow/outflow (e.g., Brotherton et al. 1994; Done & Krolik 1996) makes the origin of this material puzzling. Reasonable possible origins of the material are the accretion disk (AD) and the interstellar medium. The recently confirmed flattened geometry of the BLR, resolved observationally for the first time in two sources (Gravity Collaboration et al. 2018, 2021), may favor the first possibility, i.e., the material originates from the AD; and also recent observation-based studies (Leftley et al. 2019; Mas-Ribas 2019; Mas-Ribas & Mauland 2019) show that radiation pressure, likely on the multiphase medium, is the prevalent mechanism responsible for the outflows in quasars.

There have been many attempts by different researchers to explain the formation and dynamics of BLR clouds in a theoretical context over last 50 years. The first attempt was to simply model the emission line formation by studying the photoionization equilibrium (Osterbrock 1978), which did not explain the BLR formation mechanism and dynamics (Capriotti et al. 1980). The idea of magnetically driven winds was then initiated by Blandford & Payne (1982), in which the magnetocentrifugal force was responsible for driving the outflow to explain the BLR formation. Although the mechanism requiring a strong large-scale poloidal component of the magnetic field was not self-consistent (Balbus & Hawley 1991), dusty molecular torus and X-ray absorption features could be explained (Elitzur & Shlosman 2006; Fukumura et al. 2015; Huang et al. 2020). It was then proposed by Begelman et al. (1983) that the outer disk that is irradiated by central source to the Inverse Compton temperature can give rise to the formation of thermally driven winds that could be the origin of BLR. This also required additional elements to be assumed, such as a hot corona above the disk or an inner hot flow (Witt et al. 1997; Blandford & Begelman 1999). Radiatively line-driven winds as a mechanism for BLR formation, first studied by Murray et al. (1995), was the next theoretically based attempt that was particularly/exceptionally successful at predicting the line

profile shapes. This model most likely explains the HIL part of BLR emission, where line profiles show signatures of outflow. However, even a line-driven wind does not always escape, and a failed wind may form at some range of radii (Risaliti & Elvis 2010), thus complicating the line profile predictions. Inflow models (Done & Krolik 1996, followed by others, e.g., Hu et al. 2008 and Wang et al. 2017), in which the flow of material from large radii was considered to be responsible for BLR formation, also came under attention, but they lack predictive power. BLR formation due to disk instabilities, also known as formation in situ, has also been given attention for years (Collin & Zahn 1999, 2008; Wang et al. 2011, 2012b).

Radiatively dust-driven models are the newest models for BLR formation focusing on the radiation pressure of the AD, and also the presence of dust at large radii. The latter is hinted at in a number of papers (Rees et al. 1969; Rieke 1978; Barvainis 1987; Dong et al. 2008). This dust is usually considered to constitute the dusty/molecular torus, but dust can exist also closer in, if shielded, and may play a role in BLR formation. The models in this category are the Failed Radiatively Accelerated Dusty Outflow (FRADO) model (Czerny & Hryniewicz 2011), and a model by Baskin & Laor (2018) in which the static disk is inflated due to irradiation in the dusty part (hereafter BL18). In this work, we intend to study the dynamics of the BLR based on the FRADO model. Here, we concentrate on the semi-analytical description of the cloud motion that will later allow one to calculate the BLR transfer function and line shapes, and to compare these predictions to parametric models assuming an arbitrary cloud distribution. In this way we aim to test whether FRADO is a viable model of the LIL part of the BLR.

Due to various motivations such as estimating the central BH mass, simulating the dynamics of BLR material due to radiation pressure, either in lines or on dust, has been of high interest for researchers (e.g., Marconi et al. 2008; Netzer & Marziani 2010; Wang et al. 2012a; Plewa et al. 2013; Shadmehri 2015; Khajenabi 2016). Different geometries, and even the time-dependent case of the radiation field have been investigated in the existing literature (e.g., Saslaw 1978; Mioc & Radu 1992; Krause et al. 2011; Liu & Zhang 2011). Some studies based on radiation pressure including hydrodynamical (HD) ones do not use a realistic prescription for the radiation field of the AD. Either the disk has been initially considered as a point-like source with a luminosity (e.g., Donea & Protheroe 2002; Mosallanezhad et al. 2019), or it is treated as an extended object with only the radial component of the force (in spherical coordinates) used in the computations (e.g., Risaliti & Elvis 2010). Both cases result in the radiation field being proportional to the inverse square of the distance, so the radiation field ultimately has the form of a repelling central force and never produces a strong vertical component close to the disk surface to lift the material sufficiently before being repelled outward. This can be applicable if the BLR extends far beyond the outer radius of the AD, e.g., in BLR models based on cloud inflow from larger radii (Wang et al. 2017), but this scenario is not firmly established. Instead, there are arguments that the BLR instead overlaps with the AD (e.g., Czerny et al. 2004b). There are also a number of studies (e.g., Proga et al. 1998, 2000; Proga & Kallman 2004; Nomura et al. 2020; Mizumoto et al. 2021) that address the full disk radiation field but focus on the line-driving force in which the element of dust is missing.

Intuitively, the radiation force acting on clouds in the vicinity of the AD is not radial but almost plane-parallel. This case has been investigated in the FRADO model analytically, but only in one dimension and for a very local flux (Czerny et al. 2015, 2017). This 1D model roughly reproduces the overall BLR position without including the arbitrary parameters, but the line shapes based on this local model always showed traces of the double-peaked structure, the vertical acceleration was not as efficient as required, and they did not show the characteristic Lorentzian wings observed in high Eddington ratio sources. The line shapes improved when a much higher wavelength-averaged dust opacity was used instead of the standard $\kappa = 8 \, (\mathrm{cm^2 \, g^{-1}})$, but it was not clear that such opacity requirements were realistic. Thus, the issue of the radiation field of an extended disk must be addressed for which the net radiation force is a complex function of cloud position. Reaching a realistic prescription for the radiation of an AGN and the resulting outflow will be of high importance, not only particularly in the physics of the BLR, but also generally in AGN feedback and in star formation in host galaxies (Croton et al. 2006; Raouf et al. 2019).

The radiation field of an extended luminous disk was first calculated by Icke (1980) in a wavelength-averaged form. The method was only then followed in some papers (Pereyra et al. 1997; Proga et al. 1998, 1999; Feldmeier & Shlosman 1999; Watarai & Fukue 1999; Proga et al. 2000; Hirai & Fukue 2001; Proga & Kallman 2004; Nomura et al. 2020). We present a detailed note on the calculation of radiation field of an extended disk in the Appendix of this paper and in a very generic form capable of being folded with wavelength-dependent dust opacities.

Although the proposed theoretical attempts mentioned above could somehow explain the formation of the BLR along with some features of an AGN's spectrum, they have not been able to self-consistently explain the dynamical behavior of the BLR and its geometry altogether, which we have from observational data, especially RM-based data. Hence, approaching a unified self-consistent theoretically based model that can explain the formation, geometry, and dynamics of the BLR is highly required. The 3D FRADO model is expected to recover observationally known features of a BLR, i.e., the radius or equivalently the time-delay, the complex velocity field, and line profiles, all self-consistently without the need of any arbitrary parameter(s). In this work we especially focus on the dynamics and geometry of the BLR as the first step.

We therefore introduce our 3D FRADO model in detail in Section 2. The model does not go through HD calculations, so the effects of the pressure gradients are neglected. However, based on our results provided in Section 3, most of the time clouds (assumed to be pressure confined) move at supersonic velocities (likely along with the surrounding medium due to dynamical coupling), so we preferably limit ourselves to the relatively simple and computationally efficient non-HD version of our model. We will then test in the next paper how much the model successfully catches the overall dynamical properties and explains the observational properties of the BLR, such as line shapes, average time delays and transfer functions for LIL lines such as Hβ and Mg II. The results are then followed by a discussion in the last Section 4, where the advantages of our approach over other available BLR models including parametric models and hydro models are also addressed.

2. 3D FRADO Model With Wavelength-dependent Opacity

The basic FRADO model (Czerny & Hryniewicz 2011; Czerny et al. 2015, 2016, 2017) described the failed dusty wind motion in a 1D approximation; i.e., the motion vertical to the disk plane was included, apart from the rotational velocity. In addition, the wavelength-averaged dust opacity was used. The radiation from the central region was only included in computations of the dust evaporation and neglected in the dynamics, which was determined only by the local flux of the AD. This approximation was necessary to formulate a semi-analytical model of the dynamics. However, the radiation pressure from the entire disk in this model is not properly represented, and the proper description of the dust interaction with the radiation field is also critical for the model.

In this paper we formulate the full 3D model describing the motion of the initially dusty clouds under the radiation pressure coming from the entire AD and the gravity of a central supermassive black hole. We assume that the mass of the AD is much smaller than the BH mass and its gravitational field is negligible. The net radiation force is neither radial nor vertical, but instead a complex combination of both, and the clouds before being accelerated have a circular motion along a local Keplerian orbit at the disk surface layers, so the resulting motion of a cloud forms a complex 3D trajectory. The net acceleration is

$$\boldsymbol{a}^{\mathrm{net}} = \boldsymbol{a}^{\mathrm{gra}} + \boldsymbol{a}^{\mathrm{rad}}(< T_{\mathrm{s}}) \tag{1}$$

where $\boldsymbol{a}^{\mathrm{gra}}$ stands for the gravitational field of the central BH, and $\boldsymbol{a}^{\mathrm{rad}}$ is the acceleration due to radiation pressure of the AD given in its general form (find the detailed version in the Appendix: Equation (A15)) by

$$\int_{\lambda_i}^{\lambda_f} \int_{S} f(I_\lambda, K_\lambda^{\mathrm{abs}}, K_\lambda^{\mathrm{sca}}, \Psi, \boldsymbol{r}, \cdots) d\boldsymbol{S} \; d\lambda \tag{2}$$

where I_λ is the radiation intensity of the AD specified in Section 2.1; Ψ, K_λ^{abs}, and K_λ^{sca} are the dust-to-gas ratio, total absorption opacity, and total scattering opacity of the clump, respectively (see (A22)–(A25)), and λ_i and λ_f define the range of effective wavelengths for an adopted dust model, all addressed in Section 2.2; $\boldsymbol{r}$ is the position vector of the clump; $(< T_{\mathrm{s}})$ implies that the radiative acceleration is available as long as the dust temperature calculated in the cloud along the trajectory is less than that of the dust sublimation temperature T_{s}, otherwise dust evaporates and the cloud performs later just a ballistic motion in the gravitational field of the BH (Section 2.3); and $\boldsymbol{S}$ is the surface of the AD or part of it, as discussed in Section 2.4 on the shielding effect.

2.1. Properties of Underlying AD−BH System

We assume the source of the radiation field is represented by an extended optically thick, geometrically thin disk, described by the Shakura & Sunyaev (1973) standard model (SS73). The inner disk radius is set at $R_{\mathrm{in}} = 6R_g$, and the outer radius is located at $R_{\mathrm{out}} = 10^6 R_g$ in all models, where R_g is the gravitational radius of the BH defined as $R_g = GM_{\mathrm{BH}}/c^2$. The flux density is locally described as in SS73, including the no-torque inner boundary conditions

$$\mathbb{F}(R) = \frac{3GM_{\mathrm{edd}}}{8\pi} \frac{M_{\mathrm{BH}} \; \dot{m}}{R^3} \left(1 - \sqrt{\frac{R_{\mathrm{in}}}{R}} \right), \tag{3}$$

and the locally emitted flux is represented as blackbody emission; i.e., the intensity is given by the Planck function

$$I_\lambda = B_\lambda(T(R, \varphi)). \tag{4}$$

The AD flux is thus described by the central BH mass, set as $M_{\mathrm{BH}} = 10^8 M_\odot$, corresponding to the mean value in the quasars catalog of Shen et al. (2011), for which

$$R_g = 4.7867 \times 10^{-6} \; (\mathrm{pc}) = 0.0057 \; (\mathrm{lt\text{-}day}) \tag{5}$$

and the dimensionless accretion rate, $\dot{m}$, is normalized to the Eddington value for the adopted M_{BH}

$$\dot{M}_{\mathrm{edd}} = 1.399 \times 10^{26} \; (\mathrm{g \; s^{-1}}). \tag{6}$$

In this paper, we stick to three values of the dimensionless accretion rate: $\dot{m} = 0.01$ and 0.1 (low Eddington ratios), and $\dot{m} = 1$ (high Eddington ratio).

The description of SS73 for the flux of a nonrelativistic radiatively efficient AD provides us with an azimuthally symmetric profile for the effective temperature of the AD as a function of radius R, since

$$\mathbb{F} = \sigma_{\mathrm{SB}} \; T_{\mathrm{eff}}^4(R), \tag{7}$$

where σ_{SB} is the Stefan−Boltzmann constant; so

$$T(R, \varphi) = T_{\mathrm{eff}}(R). \tag{8}$$

2.2. Dust Opacity

In general, the radiation pressure acting on a BLR cloud should be a combination of absorption in lines and absorption/scattering on dust. In the FRADO model, aimed at modeling the LIL part of the BLR, we assume that the dust processes dominate. In this case, in contrast to the line-driven winds in which the Doppler effect is important, the absorption efficiency does not depend on the cloud velocity, and the equations given in the Appendix include this assumption. However, the effect depends on the assumption of the dust chemical composition, grain sizes, and the dust-to-gas mass ratio.

The value of K_λ can be obtained using prescriptions from Röllig et al. (2013) and Szczerba et al. (1997) for different dust models with a given distribution of dust types and grain sizes. See Equation (A24) for details on how to find K_λ assuming a given dust model with a certain distribution. We further assume the classical MRN dust model appropriate for the interstellar medium (Mathis et al. 1977), as also used in the BL18 model. This simple model consists of silicate and graphite grains. Signatures of silicate in AGNs are seen (Netzer et al. 2007), and the equilibrium temperature of the grains implies the presence of graphite (Clavel et al. 1989). However, amorphous carbon grains rather than graphite are most likely expected based on UV spectra (Czerny et al. 2004a), and/or the grain size range is not typical (Gaskell et al. 2004), as the overall extinction curve is more similar to an SMC curve than to the typical graphite-dominated Milky Way curve (e.g., Richards et al. 2003; Hopkins et al. 2004; Zafar et al. 2015). The actual content of the AGN dust is still under vigorous study (Chau Giang & Hoang 2020), but we adopt here the classical approach. The grain size distribution in the MRN model is

identical and given by

$$dn_i(a) = n \, A_i \, a^{-3.5} \, da, \qquad 0.005 \leqslant a \leqslant 0.25 \; (\mu m) \quad (9)$$

where a is the grain size (radius), i stands for the dust type, and A_i is the normalization constant that determines the overall abundances of the grain type, which directly leads to a unique value for the dust-to-gas mass ratio Ψ (see Equation (A25)). For example, setting $A_{silicate} = 10^{-25.10}$ and $A_{graphite} = 10^{-25.13}$ (Weingartner & Draine 2001) in the MRN dust model, one can obtain $\Psi = 0.00955$ (Röllig et al. 2013). We set $\Psi = 0.005$, thus adopting the mean value of the Milky Way (Mathis et al. 1977). The dust-to-gas ratio in quasars has not been yet sufficiently studied, so a firm value or range of values in this context is not yet available. However, a value of almost 0.008 is estimated for an AGN sample (Shangguan et al. 2018), and also a recent study by Jun et al. (2021) has addressed the dust-to-gas ratio in obscured quasars. K_λ is independent of dust type and abundances. The MRN dust model is taken for simplicity and realistic modeling of AGN dust content must be addressed in future studies.

Here, we assume that the coupling between the dust and the gas is strong. The friction thus prevents dust from moving faster than the gas and momentum is transferred to the gas, so the dusty/gaseous cloud moves as a single entity. The coupling is generally quite effective in dense media, for example, in star-forming molecular clouds (e.g., Hosseinirad et al. 2018; Reissl et al. 2018). The local gas number density (n_H) of the BLR clouds is rather high, with most recent estimates for the LIL BLR of order 10^{12} cm^{-3} (e.g., Adhikari et al. 2016; Panda et al. 2018, 2019a, 2019b, 2020a, 2020b; Panda 2020), so this assumption should be satisfied.

2.2.1. The Possibility of Outflow Launching in FRADO

We first test if the AD surface can be a source of the wind outflow under the effect of radiation pressure. Czerny et al. (2015, 2017) argued that in the upper part of the AD atmosphere the Planck mean opacity is much larger than the Rosseland mean opacity used in the disk interior, so the disk is not considerably puffed up, and this larger Planck value, appropriate for wind driving, will lead to an outflow. However, BL18 postulated that the AD atmosphere, with dust included, will remain static. So, first we check whether indeed the condition postulated by the FRADO model is satisfied if the realistic description of the opacity is included.

For this purpose, we calculated the value of the Planck mean opacity as a function of the AD radius (or, equivalently, as a function of the AD effective temperature) for the typical values of the model global parameters: $\dot{m} = 0.1$ and $M_{BH} = 10^8 M_\odot$, as shown in the Figure 1. We integrated the wavelength-dependent dust opacity in the whole wavelength range, from $\lambda_i = 6.1995$ (nm) to $\lambda_f = 1.2399$ (mm). The aim was to compare it with the Rosseland mean, which was used to determine the AD vertical structure needed to get the AD height.

The Rosseland mean was calculated for the same range of radii, at the position of the bottom of the AD photosphere, $\tau = 2/3$. This Rosseland mean, depending on density and temperature, comes from the tables that include dust, molecules, atomic opacities, and Thomson scattering (for details, see Różańska et al. 1999).
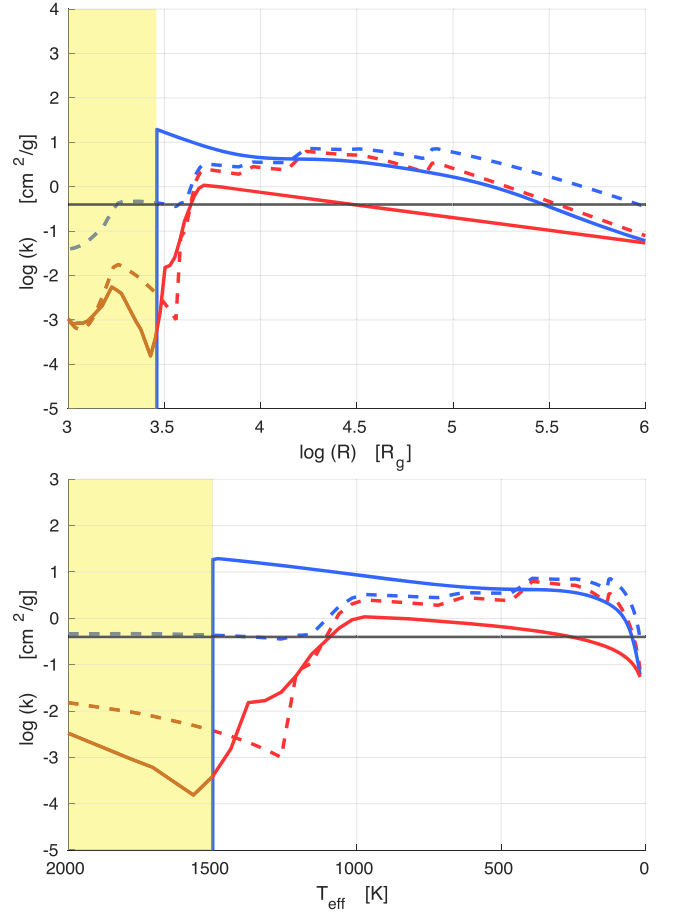

Figure 1. The upper panel shows the radial dependence of the Planck mean (blue solid line) and the Rosseland mean (red solid line) for $\dot{m} = 0.1$ and $M_{BH} = 10^8 M_\odot$ as used in the paper. The viscosity for the calculation of the Rosseland mean is set to be 0.02. The Planck (blue dashed line) and Rosseland (red dashed line) mean from the code of Semenov et al. (2003) for the density profile from the disk atmosphere are compared to our values. The lower panel displays the values in terms of the equivalent effective temperature of the AD. The black solid lines in both panels show the ratio of the Thompson cross section to the mass of a proton. The regions shaded in yellow show where the temperature is above that of dust sublimation.

In our calculation of the Planck mean, we multiply the result by Ψ because, due to gas−dust coupling, the gas content of the clump hitchhikes with the dust. However, as the gas contribution to the opacity is not included, the Planck mean formally shows a sudden drop to zero at the dust sublimation temperature. We see that the Planck mean is always higher than the Rosseland mean, which provides an argument in favor of the scenario in which the dusty wind launches from the AD surface.

Since our opacities are not the most accurate, we check this result using the code[4] described in Semenov et al. (2003) and calculating the Planck and Rosseland mean for the dust and gas material. We used the gas number density profile (n_H) from the AD atmosphere, which varied from 1.37×10^{14} cm^{-3} to 3.88×10^9 cm^{-3} at the outer radius. These computations also imply that the Planck mean is higher than the Rosseland mean, and the idea of the dynamical character of the BLR is well supported.

---

[4] https://www2.mpia-hd.mpg.de/~semenov/Opacities/opacities.html

We have to stress, however, that the use of Planck mean values of the opacity does not fully represent the driving force due to radiation pressure, as given by Equation (A15). In the actual computations we use the wavelength-dependent opacity, and the force acting on the particle is calculated by folding this opacity with the radius-dependent and spectral-dependent radiation flux.

2.3. Dust Temperature

If the dust in the cloud is overheated, it evaporates rapidly. Therefore, at each cloud position we calculate the dust mean temperature by integrating the heat absorbed by the grains embedded in the cloud and comparing it to the total cooling of all of the grains, independent of their size.

Dust cools down by instantaneous re-emission of the absorbed radiation in the form of isotropic blackbody radiation, as long as the dust temperature is below that of sublimation, so

$$Q_{\mathrm{abs}} = Q_{\mathrm{emit}}(<T_{\mathrm{s}}). \qquad (10)$$

Once $Q_{\mathrm{abs}} = Q_{\mathrm{emit}}(T_{\mathrm{s}})$ the dust content of the clump evaporates and the clump follows a subsequent ballistic motion falling back to the disk surface. See the Appendix (A.3) for details. This is a certain simplification, since the carefully calculated dust temperature depends on the grain type and grain size. However, as we have to perform the temperature computations for each point of each cloud trajectory, this much less time-consuming approximation is justified.

We later assume the fixed specific value of the dust evaporation temperature of 1500 K (e.g., Barvainis 1987; Li 2007; Figaredo et al. 2020; Huang et al. 2020), for all species and sizes, and we assume that the process happens instantaneously. The evaporation is indeed fast, of order 1 day (see BL18). Although the temperature of 1500 K is a sort of mean value for all grain sizes and species, the assumption of a single temperature is much less justified (BL18, Tazaki et al. 2020; Temple et al. 2020) and has to be treated as a first approximation. However, in our dynamical model, computations of the selective evaporation would be too time consuming, though it could have been done in the BL18 model.

2.4. Shielding Effect

According to radiatively driven wind models, launching an efficient outflow is not possible if the launching region is not shielded from irradiation by the central source (see, e.g., Gallagher & Everett 2007; Proga 2007; Higginbottom et al. 2014). This protection from intense central radiation, the so-called shielding effect, was first generally postulated by Shlosman et al. (1985) and later by Voit (1992) to justify the presence of polycyclic aromatic hydrocarbons (PAHs) in AGNs. It was first modeled by Murray et al. (1995), who assumed a bulk of dense gas at the inner edge of the line-wind launching region to block soft X-rays.

The shielding can be naturally caused by other phenomena: other clouds (Kartje et al. 1999); the wind itself because of the high-ionization parameter and high column density at the inner edge of the wind known as a "warm absorber" (Murray & Chiang 1995); a magnetocentrifugal wind (Everett 2005); the innermost failed winds first found in hydrodynamical simulations by Proga et al. (2000); or the disk itself (Wang et al. 2014). Thus the apparently necessary shielding, particularly close to the disk surface, protects the wind medium from becoming over-ionized and likely prevents the radiation from the central parts to reach the distant disk regions (Miniutti et al. 2013).
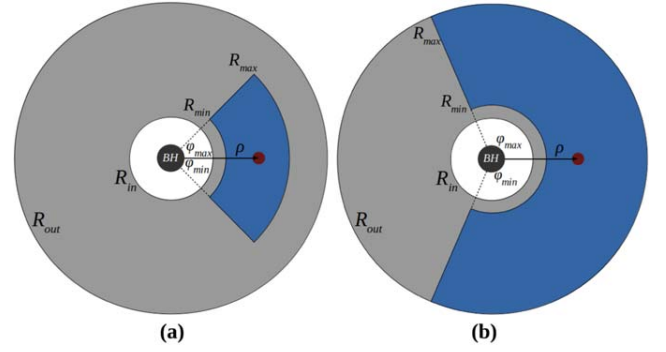

Figure 2. Geometry of (a) the α-patch and (b) the β-patch shielding models. The cloud is exposed to a part of the disk radiation marked in blue. The size and location of these blue regions change as the cloud moves. The integral of the radiation pressure to calculate the radiative force is integrated over the area of the disk shaded in blue, depending on the shielding model adopted.

There are many studies that hint at the importance of the shielding effect and model it (see, e.g., Proga & Kallman 2004; Risaliti & Elvis 2010; Sim et al. 2010; Higginbottom et al. 2013; Nomura et al. 2013; Hagino et al. 2015; Mizumoto et al. 2019).

In order to incorporate the shielding effect into our model, or indeed to mimic the physical action of the complex multiphase surroundings, we introduce two simple geometries. In our preliminary study of the shielding effect (Naddaf et al. 2020), we found that these two models conveniently catch the required properties. However, in this paper we reintroduce them with some changes to their names and geometrical properties to make them mathematically and intuitively more intelligible.

2.4.1. The α-patch Model

As the simplest form of shielding, we consider the contribution from a small polar patch to the radiation pressure acting on the clump. We assume here that the cloud is exposed only to the radiation from the small part of the disk, centered below the cloud position, and the size of the patch is always proportional to the actual height of the cloud. Thus the position and the size of the patch varies as the cloud moves. A cloud very high above the disk is exposed to a large fraction of the disk. This approach mimics the fact that a given cloud is actually embedded in the rising clumpy wind, and this clumpy wind is much denser close to the disk surface, so the radiation cannot easily penetrate the medium in the direction roughly horizontal to the disk plane. This geometry is illustrated in Figure 2(a). As a model parameter, α, we introduce the ratio of the cloud height to the patch size, which is fixed during the cloud motion.

In order to incorporate this model into our computations, we apply the below upper and lower limits in the calculation of the integral of the radiative force:

$$R_{\mathrm{min}} = \rho - \alpha z$$
$$R_{\mathrm{max}} = \rho + \alpha z$$
$$\varphi_{\mathrm{min}} = -\pi \left(\frac{\alpha z}{\rho - R_{\mathrm{in}}} \right)$$
$$\varphi_{\mathrm{max}} = \pi \left(\frac{\alpha z}{\rho - R_{\mathrm{in}}} \right). \qquad (11)$$

2.4.2. The β-patch Model

In this shielding model, the contribution of radiation pressure from a wider field of view is considered, compared to that in the α-patch model. Although we still have a polar patch acting on the clump, we examine how the consideration of a wider azimuthal angle and also of the outer part of the AD affects the motion of clumps and the overall shape of the BLR. We intend with this model to mimic the possible asymmetry of the shielding; i.e., the fact that the outer part of the disk and the azimuthally extended region excluding the central disk may be visible to the cloud. In this model, the outer radius of the patch is always $R_{\rm out}$ of the AD, the inner radius is proportional to the actual height of the cloud, and the patch is azimuthally extended by $\pi/2$. This geometry is shown in Figure 2(b). The geometrical properties of the patch varies as the cloud moves. So, in this model, again the increasing cloud height implies an increasing exposure to the disk radiation.

Therefore, the upper and lower limits for the integral of radiative force are:

$$R_{\rm min} = \rho - \beta z$$
$$R_{\rm max} = R_{\rm out}$$
$$\varphi_{\rm min} = -\frac{\pi}{2}\left(1 + \frac{\beta z}{\rho - R_{\rm in}}\right)$$
$$\varphi_{\rm max} = \frac{\pi}{2}\left(1 + \frac{\beta z}{\rho - R_{\rm in}}\right). \tag{12}$$

The computation of the radiative force acting on the cloud presented in the Appendix (Equation (A15)) is general. If the shielding effect is assumed, the integration is performed only for a fraction of the disk surface as set in Equations (11) and (12). In order to neglect the shielding, one needs to set

$$R_{\rm min} = R_{\rm in} = 6\,R_g$$
$$R_{\rm max} = R_{\rm out} = 10^6\,R_g$$
$$\varphi_{\rm min} = 0$$
$$\varphi_{\rm max} = 2\pi. \tag{13}$$

2.5. Cloud Dynamics

In the present model we neglect the effects of general relativity and use just Newtonian dynamics because, at the distance of the BLR, these effects are usually relatively unimportant.

The clouds are not allowed to cross the disk surface, so we also calculate the AD shape as a function of radius. We do that using the code from Różańska et al. (1999), neglecting the effects of self-gravity on the disk structure (see, e.g., Czerny et al. 2016, and the references therein). The disk thickness depends on the viscosity parameter, which we set as visc. = 0.02 in our computations, motivated by the variability studies of AGNs (Grzedzielski et al. 2017, and the references therein).

Clouds can be practically launched either from the disk surface or above it; the second approach illustrates the possible effects of cloud collisions. We only focus on launching from the disk surface (with zero vertical velocity). Clouds can be launched at an arbitrarily large radius, but basically we set the launching radius to be lower than the outer disk radius so that the clouds see the radiation field of the whole extended disk, and the radiation force—its direction and value—has to be calculated by integration over the disk surface. We consider models in which the clouds see all of the disk emission, but also we

formulate models with the shielding effect included. The inner radius for launching the clouds from the disk surface is actually the site of the onset of the BLR, shown in Figure 3 as BLR$_{\rm in}$, or in other words, the inner radius of the BLR for specified values of $M_{\rm BH}$ and $\dot m$ is set by the condition that a cloud can be launched.

3. Results

We formulated the 3D version of the FRADO model of the BLR. Our model does not (almost) have arbitrary parameters, apart from the values of the BH mass, $M_{\rm BH}$, and the accretion rate, $\dot m$ in Eddington units. The basic remaining free parameter is the dust sublimation temperature, $T_{\rm s}$. These three values of $M_{\rm BH}$, $\dot m$, and $T_{\rm s}$ determine the geometrical properties of the BLR and the 3D motion of the clouds. The disk height value needed for the vertical position of cloud launching depends on the viscosity parameter in the SS73 model, and if shielding is considered, one more parameter characterizes its geometry. In the present paper, we have concentrated on the tests of the dynamical aspects of the model and the resulting geometry of the BLR.

For this purpose, we have set the model parameters as below:

$$M_{\rm BH} = 10^8\,M_\odot$$
$$\dot m = 1 \text{ (High Eddington rate)}$$
$$\dot m = 0.1,\ 0.01 \text{ (Low Eddington rates)}$$
$$T_{\rm s} = 1500 \text{ (K)}$$
$$\text{visc.} = 0.02$$
$$\alpha = 3,\ 5$$
$$\beta = 3,\ 5$$
$$\Psi = 0.005 \text{ (MRN).} \tag{14}$$

3.1. Sublimation Location

Calculating the geometrical location at which the relation $Q_{\rm abs} = Q_{\rm emit}(T_{\rm s})$ holds, called the *sublimation location* and denoted by $S(R)$, we divide the space above the disk into two regions of *dust sublimation* and *dust surviving*, as shown in Figure 3. The crossing radius of the $S(R)$ and disk surface yields the radius at which dust gets sublimated at the disk surface, known as BLR$_{\rm in}$. It sets the inner radius for the launching of the clouds, as shown in Figure 3. Theoretically, BLR material can be present up to a radius known as BLR$_{\rm out}$, which is shown in Figure 3 and defined by the condition that dust can survive irradiation by the entire disk if the radiation field is spherical.

Without inclusion of the shielding effect, the function $S(R)$ has a bowl-like form (when viewed in 3D; e.g., Kawaguchi & Mori 2010, 2011; Czerny & Hryniewicz 2011; Goad et al. 2012; Oknyansky et al. 2015; Figaredo et al. 2020), while including shielding results in a more funnel-like shape.

These two values of BLR$_{\rm in}$ and BLR$_{\rm out}$ set the radial domain of our computations of the motion and trajectories of clouds. We have previously computed them and the function of $S(R)$, as available in Naddaf et al. (2020) for different values of α (or β) and also for the case with no shielding. Note that due to our change in the mathematical illustration of shielding models, the previous β behaves like $1/\beta$.

3.2. Examples of 3D Motion of a Cloud

When the clouds are initially located at the disk surface, dusty wind is not launched without a shielding effect, as the disk surface, without any protection, becomes overheated.
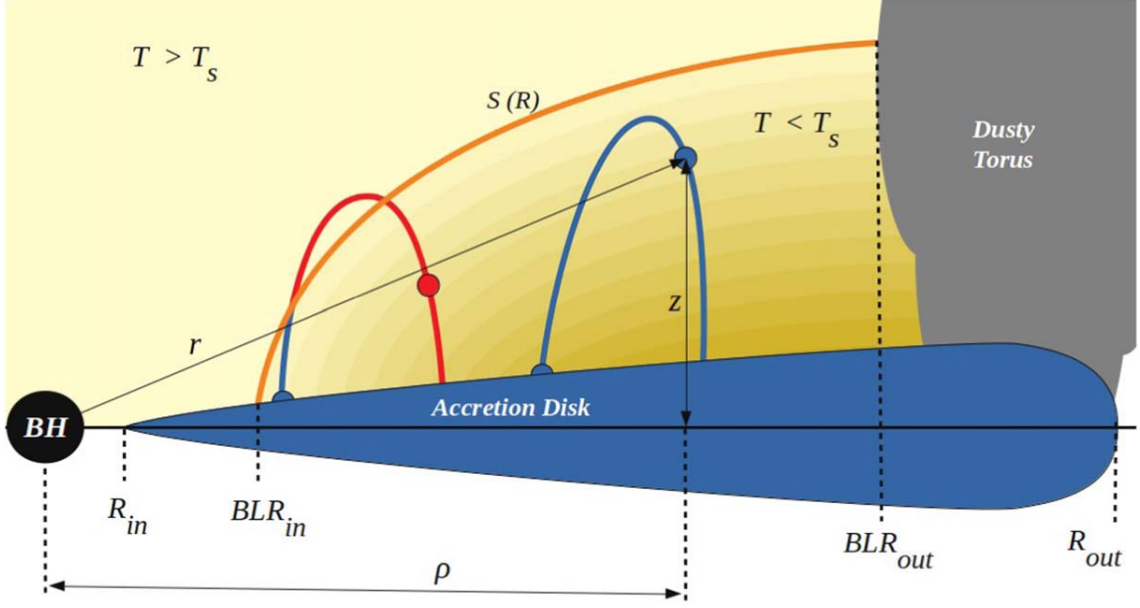
Figure 3. Schematic illustration of the 3D FRADO mechanism. The inner and outer radius of the AD are denoted by R_{in} and R_{out}, respectively. The curved line in orange represents the *sublimation location*, $S(R)$; above this, marked by ($T > T_s$), is the region where dust disappears due to intense radiation from the central parts of the AD and is called the *dust sublimation* region. The region restricted between the disk surface and $S(R)$ marked by ($T < T_s$) is called the *dust surviving* region, where the temperature of the dust is below that of sublimation. The onset of the BLR, BLR_{in}, is an innermost radius from which a cloud can be launched. BLR_{out} sets the inner radius of the *conceptual* torus and the outer radius of the BLR. A dusty clump being launched from the AD surface remains dusty (trajectory in blue) unless it reaches to $S(R)$, where it then loses the dust content and follows a ballistic motion (trajectory in red). Due to azimuthal symmetry, the position of the clump is described in the cylindrical coordinates. The radial position of the clump is denoted by ρ to make it distinguishable from the integrand component of R of the AD in the calculation of the radiation pressure (see the Appendix: Figure 10(b), and Equation (A15)). However, ρ and R are the same in nature, so for simplicity, we use R or *Radius* in all plots. The vertical position of the clump denoted by z is measured from the equatorial plane, to which we refer by z or *Height* in all plots.
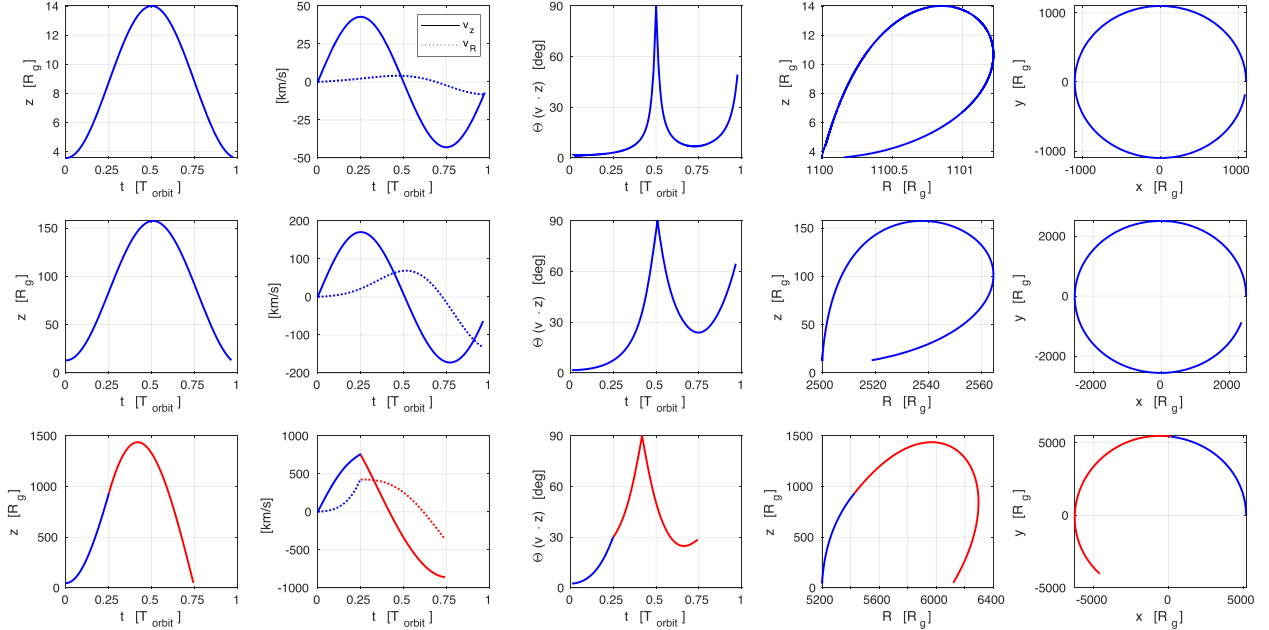

Figure 4. Examples of motion for the α-patch model with $\alpha = 3$. The results are shown for $\dot{m}=0.01$ (upper panels), 0.1 (middle panels), and 1 (lower panels). The disk surface is not depicted. The motion of the dusty cloud is shown in blue. Once the dust content of the cloud is sublimated, the subsequent ballistic motion is shown in red. Variables x and y are coordinates in the equatorial plane of the AD, so that $R^2 = x^2 + y^2$. The actual radial and vertical position and velocity of the model cloud in cylindrical coordinates are denoted by R, z, v_R, and v_z, respectively. The temporal axis is denoted by t in units of local Keplerian orbital time (T_{Orbit}). The middle column of panels shows the angle between the velocity vector of the cloud and the normal vector of equatorial plane in the frame locally co-moving with the disk. For these exemplary motions, an arbitrary launching radius of $R = 1100R_g$, $2500R_g$, and $5200R_g$ are chosen for $\dot{m} = 0.01$, 0.1, and 1, respectively.

However, if shielding is postulated, the initial outflow is easily launched. In Figure 4 we show several examples of individual cloud trajectories. The path covered by a dusty cloud is marked in blue, and in cases where the cloud was exposed enough to cause dust sublimation, the corresponding part of the trajectory is plotted in red. This part of the motion is just a
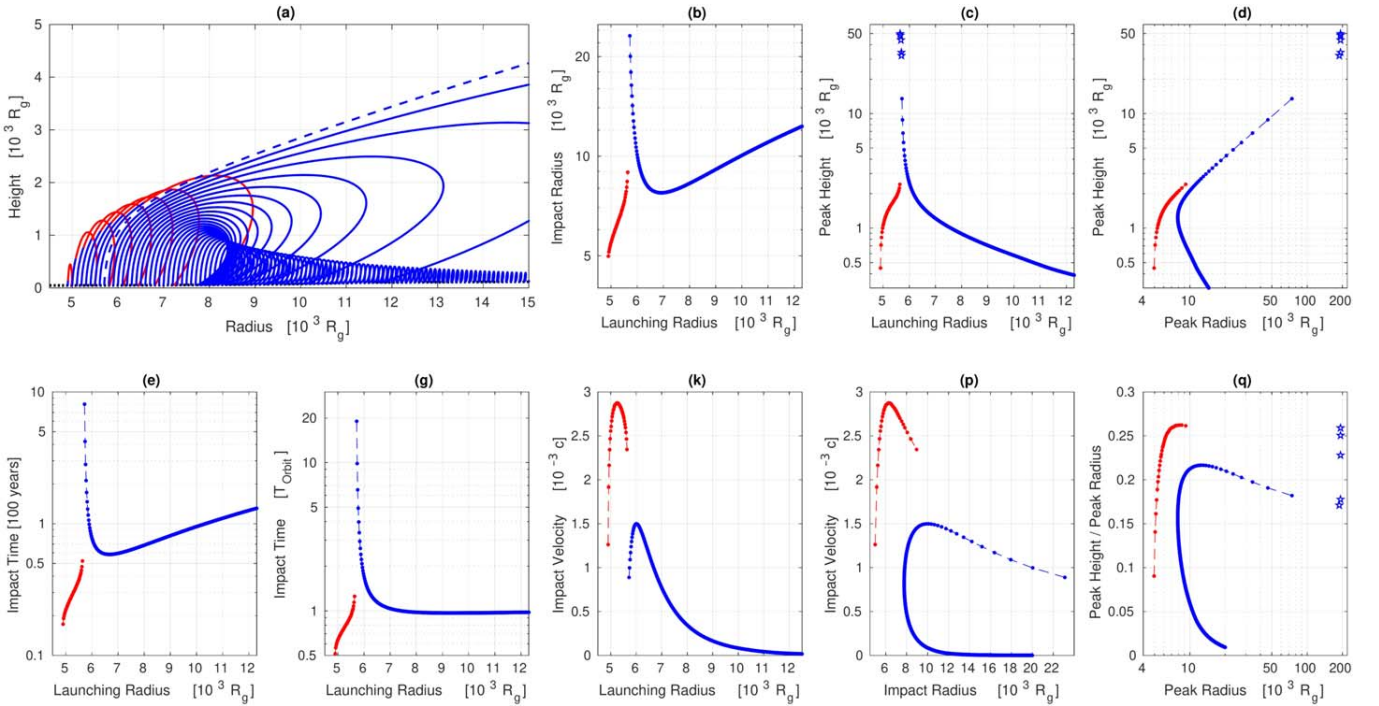
Figure 5. Global parameters of the cloud motion for $\dot{m} = 1$ in the α-patch model with $\alpha = 3$. Escaping clouds are represented by asterisks. (a) The full trajectories of model clouds. Those trajectories in the inner radii starting in blue and followed by red represent those clouds that reach the sublimation location, where they lose their dust content, and subsequently follow a ballistic motion. The trajectories fully in blue are the clouds that remain dusty throughout their time-of-flight. The blue dashed line represents the trajectory of a dusty escaping cloud. (b) The radii at which a launched cloud from a certain radius impacts the disk surface. As can be seen, there is a narrow range of launching radii from which the launched clouds can travel radially very long distances to finally impact the disk surface or even escape. (c) The maximum height a launched cloud from a certain radius can attain. For the same narrow radial range as in the previous subplot, clouds can reach to very high heights or even escape. (d) This can be considered as the shape of the BLR if all clouds are at their highest vertical position. The Peak Radius means the radius at which the cloud is at the maximum height. (e) The time-of-flight of clouds in units of a hundred years, which shows the timescale for the lifetime of BLR clouds. (g) The time-of-flight of BLR clouds in units of local Keplerian orbital time ($T_{\rm Orbit}$). (k) The velocity at which the clouds impact the disk surface. It shows that the clouds launched from inner radii can severely disturb the disk when they hit it. (p) The impact velocity of clouds in terms of where they hit the disk surface. Obviously, the whole radial range from which a cloud can be effectively launched is hit by the falling-back clouds with impact velocities ranging almost from 300 km s^{-1} to 1000 km s^{-1}. (q) The aspect ratio (Peak Height/Peak Radius) as a proxy for the opening angle of the location of the BLR clouds in terms of a point of view from outside. The larger the aspect ratio and the smaller the Peak Radius, the easier the clouds are to be detected from outside. Note that in all subplots from (b) to (q), the actual situation of clouds are color-coded by blue and red for dusty and dustless, respectively.

ballistic motion in the gravitational field of the central BH, without a radiation pressure force. In the dustless falling clouds, the dust cannot form again during ballistic motion until it hits the disk surface, due to the short timescale and low pressure (Elvis et al. 2002). Clouds also perform an orbital motion, and they preserve the original angular momentum they had at the launching radius. We show different perspectives of their trajectories, where the z-axis is perpendicular to the disk plane and the axes x and y are in the plane. We see already from this plot that the character of the motion strongly depends on the Eddington ratio.

3.2.1. Characteristics of Motion at the High Eddington Rate

To show the character of the cloud motion in more representative way, we plot the global parameters of the cloud motion for $\dot{m} = 1$ (high Eddington ratio), as displayed in Figure 5. As before, we code with the red color the clouds that end their evolution without dust. Those subplots show whether the clump is dusty or dustless at the time it hits the disk surface or reaches the peak height. The red color does not mean a cloud was dustless at the time of launching. The majority of clouds complete the motion in less than the local Keplerian timescale and return to the disk, although at a different radius than the launching radius.

As can be seen from Figure 5(a), clouds launched in the outer part of the disk (more than $7 \times 10^3 R_g$) do not rise very high above the disk, and they fall back at the radius not much larger than their starting position. The maximum height is a strong decreasing function of the initial radius in the outer disk. The impact velocity in this region is below 300 (km s^{-1}), but nevertheless it is not negligible. The impact of the failed wind clouds creates additional mechanical heating at the disk surface, which was postulated by many authors unable to model the LIL part of the BLR by just radiative heating (e.g., Joly 1987; Baldwin et al. 2004; Panda et al. 2018, 2020a).

Clouds launched at intermediate radii (roughly within 6–$7 \times 10^3 R_g$) complete very extended trajectories; they achieve a considerable height and large radii, but finally they return to much smaller radii again after performing a quasi-elliptic motion because their motion is limited by the conservation of angular momentum set at the launching radius. The impact velocity of these clouds lies within 300–450 km s^{-1}.

Clouds launched from the inner region (roughly within 5–$6 \times 10^3 R_g$) are soon exposed to irradiation strong enough to cause dust sublimation. Although their ballistic motion still brings them to relatively large heights, the radial extension of those orbits is not as large as those of the orbits of the clouds
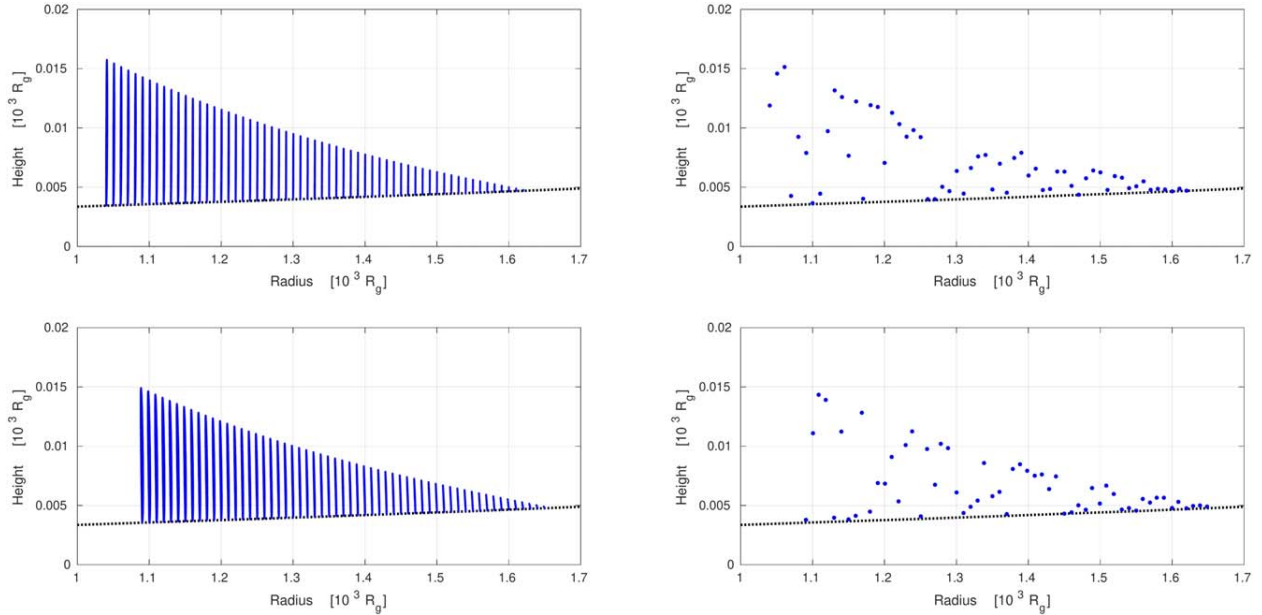
Figure 6. The trajectories of BLR clouds (left panels) and the shape of the BLR in the form of a time snapshot (right panels) calculated from the FRADO model for $\dot{m} = 0.01$. Upper panels: α-patch model of $\alpha = 3$. Lower panels: β-patch model of $\beta = 3$. The black dotted line represents the disk surface.

launched at intermediate radii. The impact velocity of these clouds is the highest, of order 1000 km s^{-1}.

The most interesting orbits are those of clouds launched within a narrow range between the innermost region and the quasi-elliptic motion region, the so-called *escaping zone*. For more details, see Section 3.2.3.

3.2.2. Comparison to Low Eddington Rates

We see from Figure 5 that the character of the motion for the high Eddington ratio depends critically on the launching radius, unlike for the low Eddington ratios, which qualitatively show a simple up and down motion (see Figures 6 and 7). Due to the simplicity of the motion for low Eddington ratios, the results are provided in this paper only for the shielding parameters of α (or β) equal to 3. The Figure 4 shows that sublimation happens mostly at the high Eddington ratio. This also can be seen in Figures 6–9.

As can be seen from Figures 4, 6, and 7, in the case of the low Eddington ratios, the departure of the clouds from the disk surface and the radial extensions of their orbits are not considerable. However, from Figures 4 and 5, for the high Eddington ratio, the height reached and radial range covered by an individual cloud are a significant fraction of the launching radius, and the motion is far more complex. Unlike the cases of low Eddington ratios that show a very simple motion, the case of the high Eddington ratio shows two interesting features due to the complex pattern of motion. They are the formation of a stream of escaping material and also the enhancement of the accretion process at the disk surface due to the complex profile of the landing/launching radius, as described in the following.

The apparently simple motion of the outer dusty clouds at the high Eddington ratio, or all dusty clouds at low Eddington rates, in general have an interesting aspect. Although these clouds do not show a considerable radial motion, their impact onto the disk surface happens at a relatively high angle with respect to the disk (see the third column of Figure 4). This is related to the fact that the vertical velocity before the impact is

slowed down by the radiation pressure (see the second column of the same plot), the angular momentum of the cloud is conserved, and the clouds complete almost one local Keplerian orbit, so the cloud takes a trajectory that brings it close to the starting radius. Thus, the impact of the clouds in all cases (not only for innermost clouds in the high Eddington solution) happens at some grazing angle. This could contribute considerably to the development of turbulence in the disk outer layers. It is not clear if such details are resolved in numerical HD simulations because the scale height of this part of the trajectory is quite small.

3.2.3. Stream of Escaping Clouds

The clouds launched within the *escaping zone* escape the radial domain of the computations, set as BLR$_{out}$, or the inner radius of the dusty torus by definition. More precisely, they do not return to the disk and directly go to torus. This stream of escaping material is relatively narrow, for the model with $\alpha = 3$ the width of the *escaping zone* is $\Delta R = 51\,R_g$, and the zone starts at the distance of $R_{stream} = 5650\,R_g$. It shows a surprising similarity to the stream postulated purely empirically based on direct observational arguments by Elvis (2000; hereafter EL00). This is also similar to the fast escaping streams in non-HD models (Risaliti & Elvis 2010; Nomura et al. 2013) and HD ones (Proga et al. 1998, 1999, 2000; Proga & Kallman 2004; Sim et al. 2010; Nomura et al. 2020).

Our ratio of the stream width to the distance is indeed very small, ~ 0.01 for the adopted parameters, but if the funnel-like structure is densely filled with the BLR clouds, and the cloud's gas number density is $\sim 10^{12}$ cm^{-3}, as argued in the BL18 model and a number of studies (e.g., Adhikari et al. 2016; Panda et al. 2018; Adhikari 2019), the total column density $N_H = n_H \times \Delta R$ across the stream measured close to the disk surface could be as high as 7.5×10^{26} cm^{-2}. Of course, this is only the firm upper limit, as the stream content depends on the details of the outflow launching (see Section 4 for more discussion). Importantly, however, it seems this can be
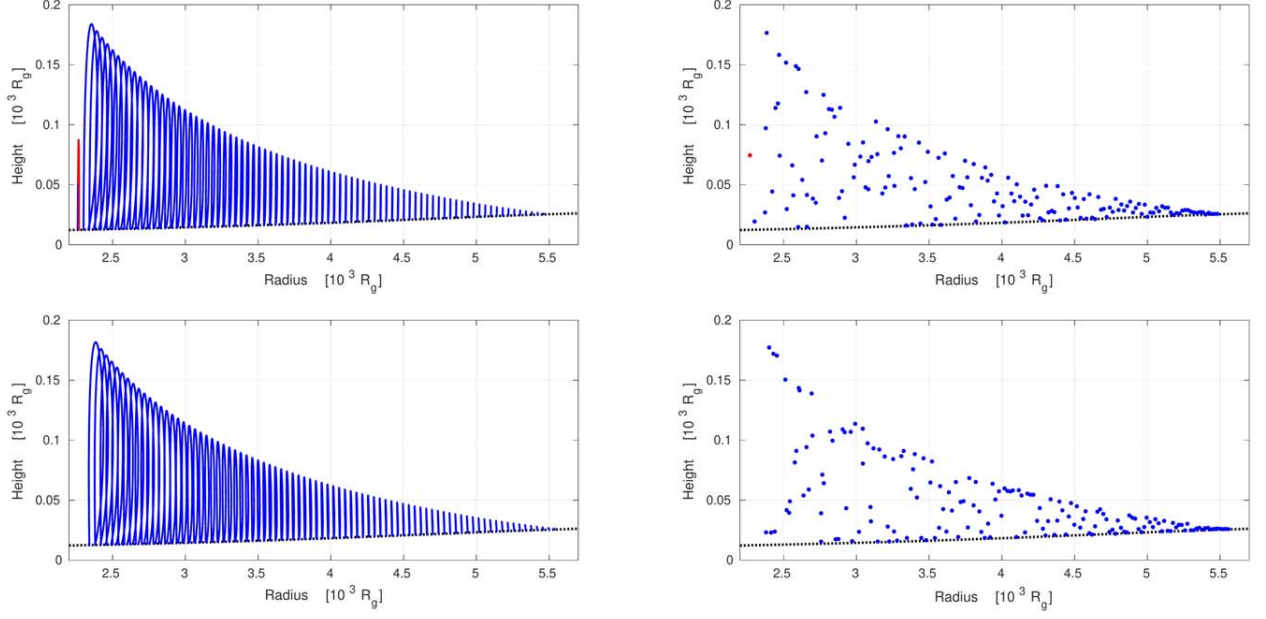
Naddaf, Czerny, & Szczerba

Figure 7. The trajectories of BLR clouds (left panels) and the shape of the BLR in the form of a time snapshot (right panels) calculated from the FRADO model for $\dot{m} = 0.1$. Upper panels: α-patch model of $\alpha = 3$. Lower panels: β-patch model of $\beta = 3$. The black dotted line represents the disk surface.
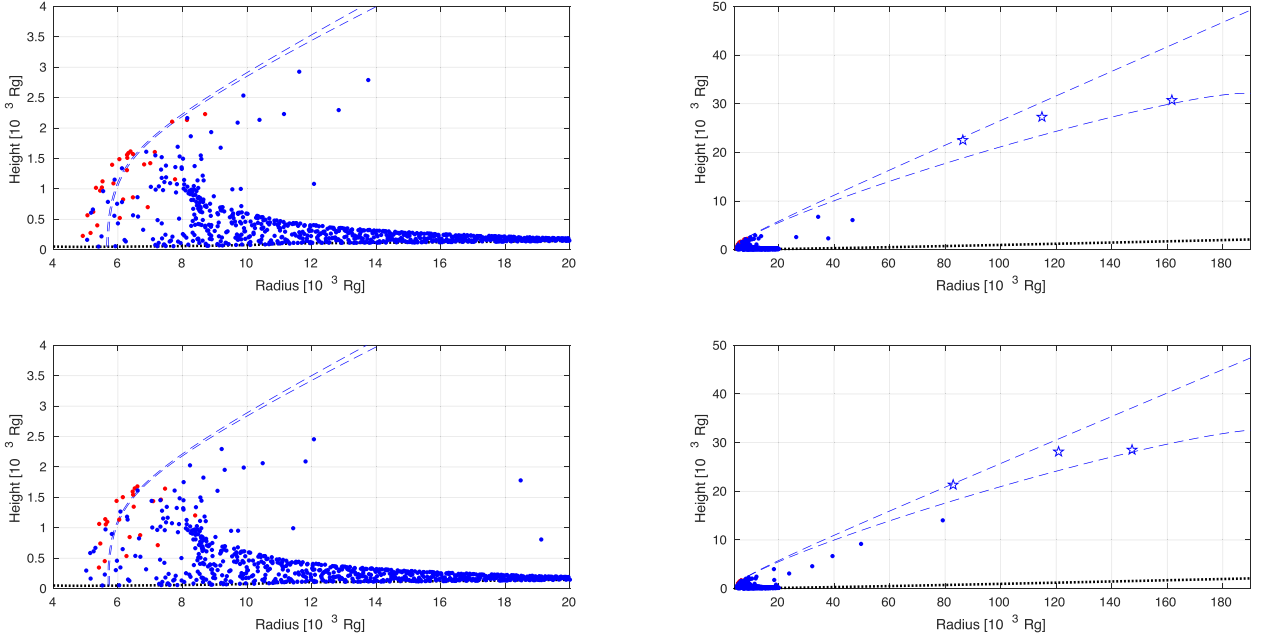

Figure 8. The shape of the BLR calculated from the FRADO model for $\dot{m} = 1$ in the form of a time snapshot. Upper panels: α-patch model of $\alpha = 3$. Lower panels: β-patch model of $\beta = 3$. Right panels are the zoom-out version of the left panels in order to show the extension of the stream up to the torus. The black dotted line represents the disk surface. Escaping clouds are represented by asterisks, and the area covered by escaping clouds is confined within the two blue dashed lines.

evidence that, in the failed wind scenario, the local radiation pressure of the AD can support dusty clumps with very large column densities (Netzer 2015). The asymptotic shape of the stream can be roughly described as a straight line in a 2D perspective in Figures 8 and 9. The inclination angle predicted by the model are around $\sim 74°$ and $\sim 79°$ for α (or β) equal 3 and 5, respectively. These are not much higher than that in EL00 with $\sim 60°$. The line-driven wind models also frequently predict wind that is more focused toward the disk plane (e.g., Higginbottom et al. 2014). The lower part of the

stream of material may not ultimately escape, as it shows a decrease in vertical velocity at the outer radius of the computational grid, i.e., BLR_{out}, where we stop the computations. But the upper part of the stream totally escapes because the vertical velocity of material close to BLR_{out} remains constant and its vertical position monotonically increases. This happens due to the fact that we define the torus to be a wall in the outer disk. So if the clouds with highly radially extended trajectories hit the wall (or, equivalently, cross BLR_{out}), they are considered to be the escaping stream. In other words, the
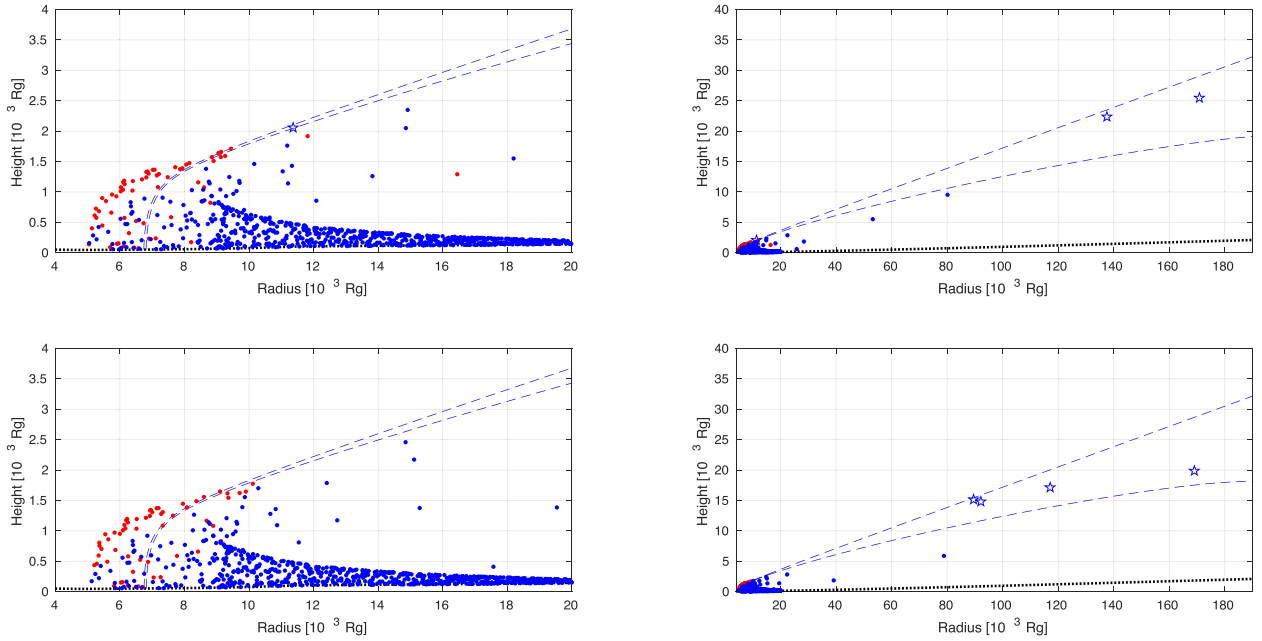
Figure 9. The shape of the BLR calculated from the FRADO model for $\dot{m} = 1$ in the form of a time snapshot. Upper panels: α-patch model of $\alpha = 5$. Lower panels: β-patch model of $\beta = 5$. Right panels are the zoom-out version of the left panels in order to show the extension of the stream up to the torus. The black dotted line represents the disk surface. Escaping clouds are represented by asterisks, and the area covered by escaping clouds is confined within the two blue dashed lines.

condition is based on the location of torus, not on the escape velocity of clouds. As can be seen from Figures 8 and 9, the inclination angle of the stream slightly increases with α (or β).

3.2.4. Landing versus Launching Radius

We notice that, due to part of the radiation pressure coming from the innermost region, the clouds are systematically pushed outwards. This effect is particularly strong in the case of the high accretion rate.

We show the ratio of the landing to starting radius for an exemplary model in Figure 5(b). This systematic return of the clouds to the disk, but at a larger radius, has considerable consequences. First, the cloud motion is calculated assuming a conservation of angular momentum, so the cloud returning to the disk has lower angular momentum than the Keplerian angular momentum at the landing point. This newly arrived lower angular momentum material does not immediately accrete because it gets mixed up with the disk material at the impact, but the net angular momentum at the disk surface (the clumps do not likely enter deeply into the disk) is lower than Keplerian, so the accretion at the disk surface can get enhanced.

3.3. The Shape of the BLR

In parametric models, the BLR is usually represented as a cone filled with the clumps, and the radial and azimuthal cloud densities are assumed to follow a power law and exponential law, respectively (Netzer & Laor 1993; Ward et al. 2014; Adhikari et al. 2016, 2018; Gravity Collaboration et al. 2018).

In our model the shape is determined by the kinematics, and in particular by the maximum height achieved by any cloud for a given initial radius. This shape does not resemble a cone; it rises up relatively fast just after the onset of the BLR, and then the height becomes shallower. The net effect strongly depends on the accretion rate as well as the free parameters of the shielding models.

In order to show the distribution of BLR clouds, we have taken a time snapshot. For this purpose, a flat random number generator is used to choose a random position of a cloud during its flight. Each dot in the Figures 6–9 correspond to a moving cloud in the BLR.

When the accretion rate is low, the height of the BLR is not high, so the clouds remain close to the disk surface, the Keplerian motion remains dominant, and the role of the vertical velocity is small (see Figures 6, 7). We see that for low accretion rates the BLR is close to the disk surface, and in practise such a model cannot be easily distinguished from the irradiated disk surface. Such a model is practically equivalent to the BL18 model. In the present paper we do not yet perform the computations of the shapes of emission lines, but the simple consequence of a small vertical height and small vertical velocity is the expected disk-like line profile. It is interesting to note that this trend is consistent with observational data: low accretion rate sources show frequently double-peak emission lines.

However, when the accretion rate is high, the vertical motion of the clouds is important. The aspect ratio (i.e., the ratio of the local BLR height to that radius) shown in Figure 5(q) reaches 0.27 for dustless clouds and 0.22 for dusty clouds. This maximum aspect ratio is not at the outer radius, but relatively close to the inner radius. We see from Figures 8 and 9 that the overall shape, particularly for the high accretion rate, is very complex. It does not resemble the simple shapes adopted in many numerical BLR models like disks, rings, or shells (Pancoast et al. 2011), or even more complicated but still regular patterns (e.g., Pancoast et al. 2014). It clearly does not support the previously mentioned conical geometry. Instead, for the high accretion rate, a shallowing tail can be seen in Figures 8 and 9 in the shape of the BLR at the outer disk where the Keplerian motion is dominant. This again resembles the results of BL18.

Overall, the calculated BLR shape in our model is similar to that of BL18. However, the FRADO model can also predict the part of the BLR shape missing in BL18 due to the loss of a static solution. Moreover, for the high accretion rate, the model also predicts the stream of escaping material proposed by EL00.

4. Discussion

In this work aimed at developing a dynamical model based on the dust-driven outflow, we followed a non-HD semi-analytical approach to the physics of the BLR. Compared to that in HD models, the description of the dynamics is simplified through approximations described in Section 4.1. Our motivation for this non-HD method is that it allows us to perform a reasonably fast test of the model for a wide range of initial parameters. This advantageous flexibility of our model versus HD models helps later to provide a large dense table grid that can be used for data fitting. Combining the results with a line formation prescription in the next paper, we will be able to compare it to the observational data (mean time delays, line shapes, and transfer functions) for the low ionization part of the BLR.

Our model, though simplified for the purpose of this test, relies on the relatively accurate description of dust-driven dynamics, and later, when combined with outflow rates and line production efficiency, can provide us with a better insight into the BLR and distribution of material than purely parametric models with the density distribution of BLR clouds predetermined as an arbitrary function of the radius and distance from the equatorial plane (e.g., Pancoast et al. 2014; Gravity Collaboration et al. 2020), although some of these models are quite complex (e.g., Matthews et al. 2020), involving a conical outflow and a simple description of clumpiness. Such purely parametric models do not easily test the driving mechanisms. Our model does not have all of the properties of the fully hydrodynamical studies; however, those studies are computationally very expensive. Moreover, before being implemented in an HD context, any model should be tested in an analytical/semi-analytical form. In the following subsections, we will discuss different aspects of the model, compare our results with other BLR studies including HD ones, and address the supporting observational facts.

In this work we calculated the 3D structure of the BLR model within the frame of the FRADO model scenario. This dynamical model of the BLR is based on careful computations of the radiation pressure force acting on clouds launched from the disk surface. We included only the radiation pressure acting on dust and so far have neglected line driving; but, aimed at modeling the LIL part of BLR, this approach may be a good approximation. However, we included the radiation force coming from the extended disk (not the frequently used assumption of a point-like source), and we included a description of the shielding necessary to launch the wind.

Our predicted shape of the BLR depends most significantly on the Eddington ratio. For the high Eddington rate, the launched clouds are accelerated to high velocities at small launch radii, and some of them form a stream of material that is outflowing. At larger radii, a simple failed wind is formed. This outflowing stream shows a striking similarity to the geometrical model of EL00, which is based on observational constraints. At low Eddington ratios, only a failed wind forms in the entire radial range, and vertical velocities and clouds maximum

heights are smaller. Despite the presence of turbulence due to the clouds' impact velocity (which is approximately a monotonically decreasing function of radius starting around 110 km s^{-1} (9 km s^{-1}) for $\dot{m} = 0.1$ ($\dot{m} = 0.01$) in the inner BLR down to less than 1 km s^{-1} for the last possible trajectory corresponding to the last lifting radius), the BLR resembles somehow a static disk surface. Therefore it shows a considerable similarity to the static BL18 model, in which clouds perform only an orbital motion, while here clouds also have vertical velocities.

The 3D dynamical model is time consuming, so currently some processes are described in a simplified way. This can be improved later on, and here also we do not yet perform a detailed comparison to observational constraints.

4.1. Approximations in the 3D Model

According to the column density of a BLR single cloud (Bianchi et al. 2012), which is of order 10^{23} cm^{-2}, the clouds are moderately optically thick. This is also an assumption of our model, since we use a single-scattering approximation (see the Appendix). If the clouds are optically thick, radiative transfer calculations should be incorporated into our computations, which is beyond the scope of this work. Notably, despite considering the single-scattering approximation, the model produces a powerful and fast outflow, contradicting the results by Costa et al. (2018), who argue an extreme or unrealistic luminosity is required to launch an outflow if single scattering is assumed. It is due to the fact that Costa et al. (2018) consider only the infrared part of the AD spectrum, while in the 3D FRADO model, a broad range of frequencies from the X-ray to UV to infrared contribute to the radiation pressure acting on dust, depending on the actual position of the dusty cloud.

Moreover, the clouds in our model are considered to be very compact, i.e., almost point-like (see the Appendix), while they are loose, extended objects (Bianchi et al. 2012). We do not address the possible collisions between clouds, however, later in Section 4.8 we show it can be a reasonable assumption. The friction with the ambient medium and the instability of clouds due to HD processes are also neglected. However, we discuss our method of treatment of clouds and interactions with the intercloud medium in Section 4.4.

Moreover, our description of the opacity is simpler than the one used in the BL18 model. We assume a fixed single dust sublimation temperature, independent from the grain size and chemical composition. In reality, as in the BL18 model, this temperature depends on the grain size, so the dust evaporation should proceed more slowly as the cloud moves, with smaller grains disappearing first and large grains still providing some radiation force support to the cloud against gravity. This is not yet incorporated in our model.

4.2. Shielding Parameters

We adopted arbitrary values for the two free parameters of α and β in our shielding models. That was due to the fact that we only wanted to test and perceive an overall view of the dynamics of the BLR material and its geometry in the 3D FRADO model with a rough shielding effect included. Obviously, from Figures 6–9, the shape of the BLR depends on the value of the α (or β) parameter, although this dependence is very weak for low Eddington ratios. But the adoptions of the two presented shielding models, either the

α-patch or β-patch, are not clearly distinguishable in terms of the resultant BLR shape. Taking a close look at these figures, it can be seen that, by adopting the β-patch model, the overall shape of the BLR shifts a bit outwards compared to that for the α-patch model. This implies that the wider azimuthal angle in the β-patch model contributes to the total radiative force significantly, while the presence of the outer radii of the disk in the β-patch model is not significant in terms of radiation pressure. So the contribution from large radii can be neglected in the β-patch model as it is in the α-patch model. Thus the α-patch and β-patch models are slightly different only due to the different ranges of azimuthal angles they cover. The α model, however, has an advantage over the β model because it clearly shows that the locally limited radiation pressure of the AD alone is able to lift the material. The α model is consistent with the fact that the field of view of a cloud above the AD is limited due to presence of the ambient medium. The β model takes into account the density gradient in the ambient medium and may be an attractive alternative to the α model when a detailed quantitative comparison with some observational data is done. The results of these models presented in this paper can help us to approach a realistic prescription for the shielding effect in a more physically motivated way, which we aim at in the next papers.

4.3. Static versus Dynamical BLR Model

We stressed in the previous sections that our dynamical model for low Eddington ratios gives qualitatively similar results to BL18. However, some similarities with BL18 exist also for the high Eddington ratio, so only the basic approaches of BL18 and FRADO are different. For the high Eddington ratio, apart from the similar shallowing tail at the outer BLR, BL18 also notice a loss of hydrostatic equilibrium at small radii, and they expect the formation of a wind where their static model does not fully work. The difference is that we follow the dynamical character of the BLR under radiation pressure, while BL18 only report the inability to obtain the static solution. Qualitatively, the loss of the static solution in BL18 happens at a similar location to the location of the *escaping zone* in our model, at about 0.03 pc (see Figure 9 of BL18 and Figures 5, 8, and 9 in this paper). A quantitative comparison is not possible since BL18 use in their Figure 9 a super-solar metallicity ($Z/Z_\odot = 5$), while we perform computations assuming a dust-to-gas ratio roughly corresponding to solar metallicity. The important comparison could be done in the future, when line profiles are calculated, and then the difference between the static model and the dynamic model would be likely quite clear.

4.4. Cloud Formation and Stability

The dynamical picture of the clumpy BLR model requires a physical justification of the assumed clumpiness of the medium. This is, however, a complex issue. Wind outflow from the disk is formally launched as a continuous medium, although in the case of a failed wind some level of clumpiness may appear already close to the disk surface. Stellar winds (escaping winds) develop clumpiness at some distance from the star (e.g., Muijres et al. 2011), most likely due to the development of a thermal instability in the irradiated medium. Expectations of the clumpiness were broadly discussed in various contexts (see, e.g., McCourt et al. 2018; Gronke & Oh 2020, and the references

therein), and hydrodynamical simulations of this effect are difficult. In the context of AGNs, spontaneous cloud formation from the wind in numerical simulations was reported by Proga & Waters (2015), Waters & Proga (2016, 2019), and Waters et al. (2021), but the cold clumps falling down were found only in the last paper, which studies much larger radii of accretion flow (well within the dusty torus), but still excludes the dust content. So, the situation in the context of the BLR clouds at the expected distances is not clear.

As for the stability, the simple evaluation of the destruction (due to ablation or evaporation) of the clouds, taking into account the electron conduction and irradiation (A. L. Müller et al. 2021, in preparation), gives timescales of order 100 yr, which is comparable to the orbital timescales. That said, some very short episodes of X-ray absorption have been identified in individual BLR clouds (Risaliti et al. 2011; Torricelli-Ciamponi et al. 2014), most likely those exceptionally high above the disk surface so they were still along the line of sight toward the observer. The observational constraints for the clouds from eclipse (Pietrini et al. 2019) imply cloud sizes of 10^{13} cm for a $10^8 M_\odot$ BH mass. Other reports of the AGN clumpy medium such as that by Markowitz et al. (2014) contain a mixture of shorter events caused by the BLR clouds and longer events related to the dusty/molecular torus clouds, which prevents one from drawing a firm observational conclusion. Most of the clouds located very close to the disk are never seen in absorption since their presence (potentially visible in highly inclined sources) is hidden from the observer by a dusty torus.

Clouds are also unstable due to the Kelvin–Helmholtz (KH) process, for which a characteristic timescale can be estimated (see, e.g., Peißker et al. 2020). The timescale for the growth of KH instabilities (for clouds of the size as in our model) is of order a few days (A. L. Müller et al. 2021, in preparation). This is much shorter than the flight time of clouds, implying the likely complete destruction of clouds before landing; however, magnetized clouds can cope with KH instabilities (McCourt et al. 2015) and survive longer (Shin et al. 2008). In addition, there are also a number of HD simulations that show an efficient acceleration of dusty material and a longer survival time despite the destructive role of such instabilities (see, e.g., Davis et al. 2014; Tsang & Milosavljević 2015; Zhang & Davis 2017; Zhang et al. 2018).

4.5. The Effects of Cloud−disk Collisions

Failed wind clouds returning to the disk bring several additional aspects that are not deeply discussed in the current paper. We briefly discussed in Section 3.2.4 the landing issue in our model, in terms of angular momentum. The impact radius of the cloud is always larger than the formation radius, which is due to the larger radiation flux from smaller disk radii. Since clouds preserve angular momentum, in this way we have a systematic departure from the strictly Keplerian angular momentum at the disk surface due to the cloud impact. This may enhance the surface layer accretion, since the effective angular momentum there becomes sub-Keplerian.

The next effect is due to the mechanical impact, which is considerable in the case of clouds on elongated orbits, so called *nonlocal clouds*, present in the $\dot{m} = 1$ solution and less important for clouds with landing radii close to the starting radius. We can estimate the depth at which the cloud material is

deposited inside the disk by a simple comparison of the ram pressure with the gas pressure inside the disk, knowing the disk vertical structure including the density, temperature, and pressure profile. For models discussed in this paper and an Eddington ratio of 0.01, the clouds are stopped at a height of order 10–20% lower than the total disk height, while for *nonlocal clouds* and an Eddington ratio of 1.0 clouds graze at up to ~50% of the total disk height. The impact leads to shock formation and nonthermal emission from particles accelerated in these shocks (A. L. Müller et al. 2021, in preparation).

The impact will lead to the destruction of the dust in the inner part of the BLR region, where the surface temperature of the unperturbed disk is below the dust sublimation temperature, but clouds penetrating the disk reach layers where the temperature is higher. High velocity clouds impacting occasionally at larger radii can do that as well. The dust there is destroyed by the mechanical heating at the impact. However, the medium at the impact is rather dense, with the local number density $n_{\rm impact}$ of the plasma above 10^{15} cm^{-3}, so it cools efficiently. If we use the cooling function $\Lambda(T)$ provided by Gnat & Ferland (2012), we can see that the kinetic energy of impact, of order $n_{cl} m_p v_{\rm impact}^2$ per unit mass, can be re-emitted in a timescale of order seconds

$$t_{\rm cool} = \frac{n_{cl}\, m_p\, v_{\rm impact}^2}{\Lambda(T)\, n_{\rm impact}^2} \sim 1 \ (\rm s) \qquad (15)$$

assuming the gas temperature T is of order 10^4 K and assuming that the cooling medium is still optically thin, as is the whole cloud. The key issue is then the origin of the dust. If the dust must arrive from larger radii (e.g., from the outer dusty/ molecular torus), then of course the accretion process would be very long. However, as was argued by Elvis et al. (2002) and used in the proposed FRADO model of Czerny & Hryniewicz (2011), the conditions in the outer layers of the disk are perfect for the dust formation in situ. Efficient dust formation requires well-defined pressure and temperature conditions, and high densities in the disk allow for these conditions to be satisfied. The conditions of dust formation are best studied in the case of stars; the details of the early stage of the dust formation are still unclear (the issue of dust seeds—see, e.g., Ventura et al. 2012), but dust formation actually happens in the stellar wind, at distances of up to a few stellar radii, so the timescales must correspond to the wind outflow timescales, set by the wind velocity, of order a few tens of km s^{-1} (e.g., Goldman et al. 2017), which is of order days up to a year. Such a timescale is much shorter than the time separation between the two cloud impacts at a given location, since the cloud impact events are separated by the timescale of order fraction of the local orbital (Keplerian) timescale, which is about 100 yr. Therefore, the dust destruction is only temporary, and the dust content in the disk atmosphere is recovered between impacts.

4.6. The Fast Outflow Stream

High velocities of escaping material, which can extend to very large distances triggered by disk radiation pressure, have been addressed in a number of papers (Hopkins & Elvis 2010; Harrison et al. 2014; Ishibashi & Fabian 2015; Thompson et al. 2015; Ishibashi et al. 2017; Costa et al. 2020).

The stream-like feature of the outflow predicted empirically by El00 was previously shown in HD simulations by Proga et al. (1998, 1999, 2000). More studies later also showed the development of such a feature in an HD context (see, e.g., Proga & Kallman 2004; Sim et al. 2010; Nomura et al. 2020) and even in non-HD models (Risaliti & Elvis 2010; Nomura et al. 2013).

While the models mentioned above focus on line-force on the BLR gas, which most likely corresponds to the HIL of the BLR, this work is the first study to hint at the development of such a feature also at larger distances, in the LIL BLR (not the torus), as a result of radiation pressure acting on dust. The stream is highly inclined and focused more toward the AD with an inclination of ~70–80°, consistent with observations (Gravity Collaboration et al. 2018) and sophisticated HD models (e.g., Proga et al. 2000; Proga & Kallman 2004; Nomura et al. 2020). However, it initiates at larger radii of few $10^3 R_g$ responsible for the LIL BLR, compared to a few $10^2 R_g$ in HD studies (also see Sim et al. 2010; Higginbottom et al. 2014) where the HIL BLR develops. The feature in our model is seen only for the case of the high Eddington rate, but an enhancement of the metallicity and the dust-to-gas ratio to more typical super-solar values in AGNs can give rise to the same feature even in lower accretion rate sources. Thus, we would expect two separate streams of material, at two different distances from the BHs.

4.7. FRADO Predictions versus Observations

As discussed above, our reasonably justified model is also fast enough compared to HD models to produce results for a large grid of initial physical parameters. We believe that the negligence of hydro effects is not very important. As argued by Risaliti & Elvis (2010), the motion in the radiative acceleration phase and later the motion of the clump in the medium are highly supersonic, so the effect of the pressure gradient to change the density and the internal pressure of the clouds can be neglected. The fact that our simple description recovers the motion complexity seems to support this view. Thus, an approximate description may be good enough for testing if indeed the radiation pressure acting on dust drives the motion of the BLR clouds.

4.7.1. RL Relation

The FRADO model well predicts the basic location of the LIL BLR (Czerny & Hryniewicz 2011; Czerny et al. 2017), and the estimates using shielding allowed us to recover the radius −luminosity (RL) relation, including the dispersion (Naddaf et al. 2020). The earlier studies indicated a rather tight relation, but new reverberation mapping results indicate considerable dispersion in the RL relation (Czerny et al. 2019; Du & Wang 2019; Fonseca Alvarez et al. 2020; Martínez-Aldama et al. 2020). This dispersion, which is apparently different depending on the broad line that is adopted as the indicator (Zhang et al. 2021), is most likely related to a spread in the Eddington ratio (e.g., Du et al. 2016; Naddaf et al. 2020; Zajaček et al. 2020, 2021), which reflects the spread in the optical/UV spectral energy distribution and the available ionizing flux (Fonseca Alvarez et al. 2020).

A preliminary test of our results with observations can be done as follows. For the high Eddington rate, we consider the radius most densely impacted with falling clouds, covering a

broad range of aspect ratios, i.e., $8000R_g$, as shown in Figures 5(p) and (q), to be the location of the BLR. As for the low Eddington rates, the location of the BLR is taken to be where the highest peak is attained by clouds, most likely to be visible to the observer, which is around $2400R_g$ and $1100R_g$ as shown in Figures 6 and 7 for rates of 0.1 and 0.01, respectively. We calculate the time delays for the viewing angle of $i = 39.2°$ (Lawrence & Elvis 2010) and for both the clouds located in the [closer—farther] side of the AD relative to the observer using

$$\tau = \frac{R_{BLR}}{c}(\sqrt{1 + q^2} \pm \sin i - q \cos i) \tag{16}$$

where q is the aspect ratio, as in Figure 5(q). The value of q is negligible for low Eddington rates, while for the high rate we take the median value of $q = 0.15$. It gives [4.57–20.42], [10–44.67], and [23.44–138] days for the Eddington rates of 0.01, 0.1, and 1, respectively. We can compare these limits with the transfer function for the Hβ line determined observationally. For example, the transfer function in Mrk 817, with a BH mass of $(4.9 \pm 0.8) \times 10^7$ (Peterson & Horne 2004) and an Eddington ratio of 0.14 (Li et al. 2016), mostly peaks in the range of 10–30 days (Li et al. 2016), which seems to be consistent with our predictions given above for these accretion parameters. It must be stressed here again that in our model the location of the BLR depends only on the assumption of the dust sublimation temperature, and gives the location of the LIL part of the BLR. A detailed study of the RL relation and the transfer function measurements based on the model will be addressed in the next paper.

4.7.2. Line Shapes and Ratios

In the current paper we do not address the issue of the line shapes and ratios, since this requires a complex approach, such as those in typical parametric models (e.g., Pancoast et al. 2014). Our model predicts the radiation flux seen by the clouds, but indeed the cloud density will have to be parameterized. We can start from the assumption of a constant cloud density, since its quite universal value is supported by the line ratio fitting in the LIL BLR (e.g., Adhikari et al. 2016; Panda et al. 2018; Adhikari 2019). Later we can limit the freedom by assuming the power-law radial distribution of the density of the hot intercloud medium, and then determine the cloud density as a function of the radius from the pressure balance or pressure confinement (Różańska et al. 2006; Baskin & Laor 2018). We expect that our more complex dynamics will give single-peak Lorentzian profiles not only for extremely low viewing angles (e.g., Goad et al. 2012), but also for moderate inclinations in the case of high Eddington ratio objects.

4.7.3. BLR and Torus

It has been matter of debate, due to many studies based on interferometry (e.g., Clavel et al. 1989; Swain et al. 2003; Kishimoto et al. 2009, 2011; Pott et al. 2010; Gravity Collaboration et al. 2020) and RM (e.g., Suganuma et al. 2006; Koshida et al. 2014; Schnülle et al. 2015; Minezaki et al. 2019), whether dust is located within the BLR radii or it only sets the outer radius of the BLR, defining the *dusty torus*. Our new sophisticated 3D FRADO model predicts the launch of dusty material from the disk due to AD radiation pressure as the mechanism of formation of the BLR whose trajectories can

extend to large radii and high altitudes that can be responsible for the formation of torus. The results of complex flying material above the disk surface are consistent with the findings of studies by Goad et al. (2012) and Figaredo et al. (2020). It also shows that the emission of the BLR and dusty region are interrelated, as confirmed by Wang et al. (2013).

The dusty torus has been introduced for masking the central disk from observation at high inclinations due to presence of a large amount of dust of high column densities extending from the equatorial plane to high altitudes (Antonucci & Miller 1985). The structure is not likely to be static, but a possible scenario involves the interaction between the outflows and inflows to form a geometrically thick torus (Wada 2012). Lawrence & Elvis (2010) suggested distorted/misaligned disks as the obscurer.

In most scenarios proposed so far for the formation of dusty torus, a sublimation radius is defined based on the condition of surviving dust from the spherical AD radiation field. The radius sets the onset of the dusty torus, the first radius from which dust survives the intense radiation of the whole AD at any altitude above the disk. However, the question is what brings the dusty material to those high altitudes. Therefore, a dynamical model of the wind was proposed for the torus itself (e.g., Konigl & Kartje 1994; Elitzur & Shlosman 2006; Gallagher et al. 2015), but this was not a failed wind. The dust location is constrained in an interesting observational study by Markowitz et al. (2014) covering mostly high Eddington rate sources. It gives a radial domain spanning $0.3–140 \times 10^4\, R_g$ for the location of BLR clouds. This implies that clouds are partially in the outer dusty torus, but partially in the BLR. However, the outflow of BLR clouds toward the torus, as in our results for the high Eddington rate, and in other studies (e.g., Kawaguchi & Mori 2010, 2011; Goad et al. 2012; Hönig 2019; Figaredo et al. 2020), can provide some momentum to the claim that the dusty torus is a posterior to the BLR and is indeed part of it; however, this view is far from being widely and firmly accepted.

4.7.4. The Mass Outflow Rate

In order to estimate the ejected mass from the AD due to radiation pressure within the *escaping zone*, we assume that the clouds are optically thin at the time of launching. So the optical depth of the cloud, τ, in the vertical direction can be of order one. The Planck mean at sublimation radius is almost 50 times the Thompson value (see Figure 1). One can obtain the column density of $N_H^{vert} = 3 \times 10^{22}\, cm^{-2}$ in the vertical direction, according to $\tau = N_H^{vert} \times \sigma_{Pl}$ where σ_{Pl} is the Planck mean opacity. It is much higher than the column density in the horizontal direction, as discussed in Section 3.2. We are thus able to approximate the total flow of the vertically ejected mass as

$$\dot{M}_{outflow} = \frac{2\pi\, R_l\, \Delta R\, N_H}{t_{exit}} = 1.1152 \times 10^{23}\, g\, s^{-1} \tag{17}$$

where $R_l = 5680\, R_g$ is a launching radius within the *escaping zone*, $\Delta R = 51\, R_g$ is the width of the *escaping zone*, and $t_{exit} = 1.79 \times 10^8$ s is the time it takes for the ejected material at R_l to leave the *escaping zone*. Compared to the whole accretion rate of $\dot{M}_{edd} = 1.399 \times 10^{26}\, g\, s^{-1}$ for accretion rate of $\dot{m} = 1$ and the adopted $M_{BH} = 10^8 M_\odot$, the value is small. Although it does not perturb the whole accretion process, it is not negligible, either. However, this implies the modeled stream

of material does not explain the BAL QSO flow (Borguet et al. 2013) where the outflow is massive. So the huge amount of material must come from somewhere else, most probably from some circumnuclear rings, etc.

4.8. Number of Clouds and Probable Collisions

Taking an upper limit for the mass-loss rate of the entire disk at the high Eddington rate, i.e., 10^{24} g s^{-1}, one can simply estimate the total number of BLR clouds at any given moment, and also the mean flight time between two successive direct collisions of clouds. The mass of BLR clouds of typical size 10^{12}–10^{13} cm and typical density 10^{12} up to 10^{13} cm^{-3} lies in the range of 10^{24}–10^{28} g, which corresponds to the launching of 10^{-4} up to 1 cloud per second. Combining with the flight time of clouds of around several tens of years (as implied by Figure 5), we obtain a total number of 10^5–10^9 clouds building the BLR.

A simple formula from thermodynamics yields the collision timescale of clouds as

$$\tau_{\mathrm{coll}} = \frac{\lambda}{\overline{v}} = \frac{1}{\sqrt{2}\ n_{\mathrm{cl}}\ \sigma\ \overline{v}} \qquad (18)$$

where $\overline{v}$ is the average velocity of clouds, which in this case is of order 1000 km s^{-1}, and λ is the *mean free path* where n_{cl} is the volume number density of clouds, and σ is their collision cross section. It can be rewritten as

$$\tau_{\mathrm{coll}} \simeq 0.1\ \frac{R_{\mathrm{BLR}}^3\ n_{\mathrm{H}}\ m_{\mathrm{p}}\ R_{\mathrm{cloud}}}{\dot{M}_{\mathrm{outflow}}\ t_{\mathrm{flight}}\ \overline{v}} \qquad (19)$$

for a very geometrically flattened, shallow BLR, with a height of order 0.1 times its radial size. Recasting it for a BLR of typical radial size 10^{17} cm, we have

$$\tau_{\mathrm{coll}} \simeq 20 \left(\frac{n_{\mathrm{H}}}{10^{12}\ \mathrm{cm}^{-3}}\right)\left(\frac{R_{\mathrm{cloud}}}{10^{12}\ \mathrm{cm}}\right)\left(\frac{100\ \mathrm{yr}}{t_{\mathrm{flight}}}\right)\mathrm{yr}. \qquad (20)$$

This is almost the minimum value for the collision timescale, since the flight times of clouds are mostly less than 100 yr (see Figure 5(e)), and also a minimum value for n_{H} or R_{cloud} and an upper limit for the disk mass-loss rate are adopted. It therefore implies that direct encounters are not highly probable, such that the clouds may experience one collision during a full orbit. So neglect of the adjustment of a given cloud trajectory due to adjacent trajectories is a relatively safe assumption in our calculation.

4.9. Dusty BLR Studies in an HD Context

Our description of the dynamics relying on the presence of dust and the important role of dust driving in the BLR, although simplified, shows good potential to address observational features, as discussed in Section 4.7. However, the results for the dynamics from our model cannot be compared yet with HD simulations, since these simulations did not aim to address the dusty BLR. Instead, there is a long list of HD studies and/or advanced physically based studies aimed to model the dusty torus (e.g., Konigl & Kartje 1994; Dorodnitsyn et al. 2012; Wada 2012; Chan & Krolik 2016, 2017; Hönig 2019; Williamson et al. 2019; Huang et al. 2020) or assuming the line-driven mechanism (e.g., Murray et al. 1995; Proga et al. 2000; Higginbottom et al. 2014; Waters et al. 2016, 2021; Waters & Proga 2016). Torus-modeling

papers assume the inner radius of their structure at the location with dust sublimation temperature calculated from the total bolometric flux, so the temperature of the medium is lower than in the BLR. We know from observations that this region is a factor of ~5 larger than the BLR radius measured from the Hβ line delay (Koshida et al. 2014). Papers based on line-driven winds predict a BLR radius that is too small for LIL such as Hβ. For example, in Proga et al. (2000), the outflowing stream starts at 7 light days (for a BH mass of 10^8 $M_\odot$ and an Eddington ratio of 0.5), which is rather more appropriate for HIL lines (also see Waters & Proga 2016), while our dust-based model gives 27 days, as expected for Hβ. We therefore have to look forward to future HD models that incorporate dust-related mechanisms in BLR dynamics.

The future development of realistic HD models for the dusty BLR will be certainly difficult, as hinted at by rather advanced dust/gas dynamics modeling done in the context of proto-planetary disks (see, e.g., Vinković & Čemeljić 2021). Another important issue in HD simulations is that the clumps in current simulations, either dusty or gaseous, are of very low density, very large size, and/or very far from the center (e.g., Waters et al. 2021) compared to dense small BLR clouds of size 10^{12} up to 10^{13} cm (e.g., Risaliti et al. 2011; Pietrini et al. 2019) located closer to the central irradiating source. Regarding the typical size of a BLR of order 10^{17} cm, one needs to have a spatial resolution of $\sim 10^{-4}$ or better in order to resolve a single BLR cloud, which has not yet been reached by highly time- and computational-expensive 2D or 3D HD simulations. Alternatively, we can just rely on the observational facts to test the model, and this is the path we plan to take in the near future.

5. Summary

We tested the dynamics of the BLR under the 2.5D non-HD prescription of the FRADO model. In this test we incorporated into the model wavelength-dependent dust opacities and two proposed configurations for the shielding effect.

As the results imply, the model is similar to the BL18 model of a static puffed-up disk, although the FRADO model catches the whole dynamical shape of the BLR, most importantly for the high accretion rate, where BL18 noticed the loss of the static solution. The FRADO model also predicts the thin-funnel-like stream of escaping material proposed in the EL00 model for the high accretion rate.

The shape of the BLR for the high accretion rate seems to be very complicated and does not show any resemblance to the usually adopted shapes for the BLR including disks, rings, shells, or cones. It is intuitively expected to produce single-peak emission profiles for the high accretion rate. However, we expect to have disk-like line profiles (double-peak emission lines) for low accretion rates due to simple up/down motions of clouds with small vertical heights and velocities. We will calculate the shape of line profiles and examine their dependence on accretion rates and other parameters in the next paper.

The model shows that it may account for the LIL part of the BLR. We previously performed a preliminary test of the model with the radius−luminosity (RL) relation. It was successful in explaining the observed dispersion in the Hβ RL relation based on the Eddington ratio. In our next paper, we will consider time-delay measurements resulting from the 3D FRADO model in full detail.

Appendix
Physical Calculations

A.1. Radiation Pressure from an Extended Luminous Disk Acting on a Single Cloud

The computations of the dusty cloud motion are based on the determination of the radiation pressure from the extended accretion disk. Our approach is basically similar to the computations done by Icke (1980), but the medium opacity there was described by a wavelength-independent Thomson cross section for electron scattering, which reduces the problem considerably. Here, we use a complex description of the opacity, and the computation of the force from a given disk part depends not only on the relative geometrical position of the disk/cloud system, but also on the disk local temperature. Computations of the radiative force from the line-driven wind in a number of papers (e.g., Pereyra et al. 1997; Proga et al. 1998; Feldmeier & Shlosman 1999) were also done by integrating the force over the extended disk, but in these papers no integration is performed over the wavelength for a specific contribution from the disk, and only the local disk flux is important, not the spectral shape. Moreover, the line-driven force indeed depends on the velocity gradient, which complicates considerably the dynamical computations. In the case of dust radiation pressure, no coupling with velocity is present, but the wavelength integration, grain size distribution, and chemical composition are important, as it allows automatically for the inclusion of the UV and infrared force component. We also take care of the effects of scattering and absorption separately. Since this integration over wavelength is an important aspect of the computations, we present the details of the method below.

The time-independent radiation pressure due to absorption and scattering by definition (Mihalas 1978) are

$$P^{\text{abs}} = \frac{1}{c} \int \int I_\lambda(\boldsymbol{r}, \hat{\boldsymbol{s}}) \cos \alpha \; d\Omega \; d\lambda \tag{A1}$$

$$P^{\text{sca}} = \frac{2}{c} \int \int I_\lambda(\boldsymbol{r}, \hat{\boldsymbol{s}}) \cos^2 \alpha \; d\Omega \; d\lambda \tag{A2}$$

where I is the intensity of the radiating object, c the speed of light, and α is the angle between the unit vector $\hat{\boldsymbol{s}}$ and the normal to the area element $\hat{\boldsymbol{n}}_A$ shown in Figure 10(a). Therefore the absorption- and scattering-driven radiative acceleration of an infinitesimal object (dA) irradiated by an infinitesimal emitter (dB) shown in Figure 10(a) are

$$\boldsymbol{a}^{\text{abs}} = \frac{1}{Mc} \int \int I_\lambda \; \sigma_\lambda^{\text{abs}} \cos \alpha \; \hat{\boldsymbol{s}} \; d\Omega \; d\lambda \tag{A3}$$

$$\boldsymbol{a}^{\text{sca}} = \frac{2}{Mc} (-\hat{\boldsymbol{n}}_A) \int \int I_\lambda \; \sigma_\lambda^{\text{sca}} \cos^2 \alpha \; d\Omega \; d\lambda \tag{A4}$$

where M is the mass of irradiated object (the receiver), and σ_ν is the cross section of the irradiated object for absorption or scattering, which in general is frequency dependent. It should be noted that we have used σ_ν rather than dA, which is applicable provided that the gradient of radiation pressure across the irradiated object (receiver) is negligible. It implies a small receiver (or, equivalently, grains with small values of cross sections).

Assuming the effective cross section of the receiver to be always perpendicular to $\hat{\boldsymbol{s}}$, so $\alpha = 0$, and we have

$$\boldsymbol{a}_{\text{grain}}^{\text{abs}} = \frac{1}{M_{\text{grain}}} \frac{1}{c} \int \int I_\lambda \; \sigma_\lambda^{\text{abs}} \; \hat{\boldsymbol{s}} \; d\Omega \; d\lambda \tag{A5}$$

$$\boldsymbol{a}_{\text{grain}}^{\text{sca}} = \frac{1}{M_{\text{grain}}} \frac{2}{c} \int \int I_\lambda \; \sigma_\lambda^{\text{sca}} \; \hat{\boldsymbol{s}} \; d\Omega \; d\lambda \tag{A6}$$

so the total radiative acceleration of the object is

$$\boldsymbol{a}_{\text{grain}}^{\text{rad}} = \frac{1}{M_{\text{grain}}} \frac{1}{c} \int \int I_\lambda \; \sigma_\lambda^{\text{rad}} \; \hat{\boldsymbol{s}} \; d\Omega \; d\lambda \tag{A7}$$

where $\sigma_\lambda^{\text{rad}} = \sigma_\lambda^{\text{abs}} + 2\sigma_\lambda^{\text{sca}}$.
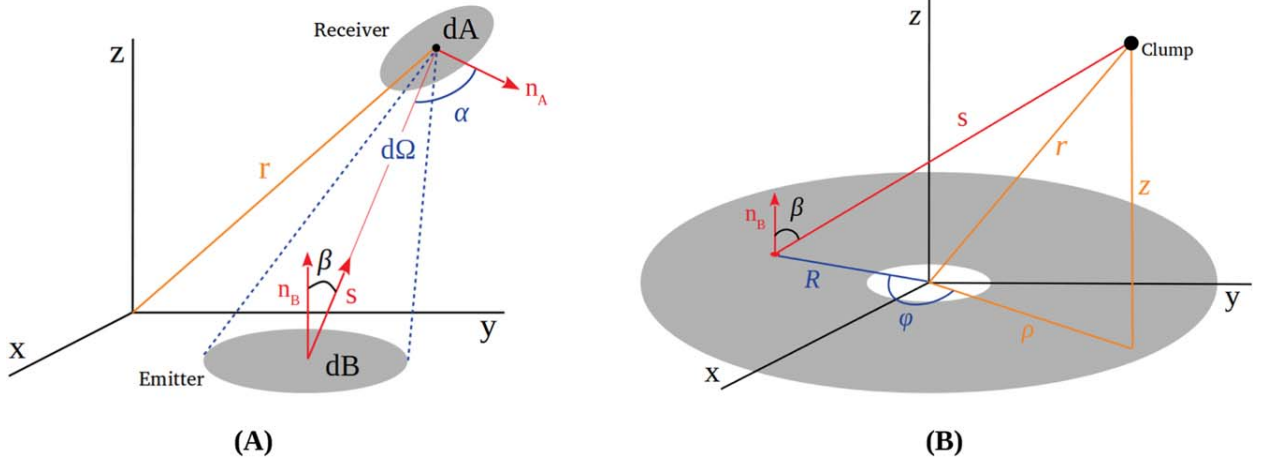

Figure 10. (a) Geometry of the emitter−receiver system, which resembles the disk−cloud system for a differential (infinitesimal) segment of the disk. (b) Geometry of the disk−cloud system.

Using the definition of solid angle, we consider an extended disk-like radiating surface shown in Figure 10(a) in gray, where the red spot is the area element in polar coordinates, dB, shown in the Figure 10(b), and $\hat{n}_B$ is the unit vector normal to dB. So we have

$$d\Omega = \frac{\cos\beta}{s^2} R \, dR \, d\varphi \qquad (A8)$$

where $\cos\beta = z/s$, and $\hat{s} = s/s$. So we have

$$a_{\text{grain}}^{\text{rad}} = \frac{1}{M_{\text{grain}}} \frac{z}{c} \iiint I_\lambda \, \sigma_\lambda^{\text{rad}} \frac{s}{s^4} R \, dR \, d\varphi \, d\lambda. \qquad (A9)$$

Knowing that $s = r - R$, using the below definitions

$$\begin{cases} r = & \rho & \hat{\rho} + & z & \hat{z} \\ R = & R\cos\varphi & \hat{\rho} + & R\sin\varphi & \hat{\rho}_\perp \end{cases} \qquad (A10)$$

we can obtain the vector s and its length as

$$s = (\rho - R\cos\varphi)\,\hat{\rho} - R\sin\varphi\,\hat{\rho}_\perp + z\,\hat{z} \qquad (A11)$$

$$s^2 = r^2 + R^2 - 2\,\rho\,R\cos\varphi. \qquad (A12)$$

Due to azimuthal symmetry, the summation over the second term of s would give zero, so we have

$$a_{\text{grain}}^{\text{rad}} = \frac{1}{M_{\text{grain}}} \frac{z}{c} \iiint I_\lambda \, \sigma_\lambda^{\text{rad}}$$
$$\times \frac{(\rho - R\cos\varphi)\,\hat{\rho} + z\,\hat{z}}{(r^2 + R^2 - 2\rho R\cos\varphi)^2} R \, dR \, d\varphi \, d\lambda \qquad (A13)$$

for which one can have the components in Cartesian coordinates just using $\hat{\rho} = (x\,\hat{x} + y\,\hat{y})/\rho$.

This is different from the approach of Icke (1980) in terms of the denominator. In the definition of $\hat{s} = s/s$, we can remove the second term of $\hat{s}$ due to azimuthal symmetry, but it can not be removed from s (the magnitude of $\hat{s}$). However, this mistake did not propagate in the literature.

This gives the net radiative acceleration for a single grain of a specific size and certain type of material. But for a dusty clump, i.e., a distribution of dust particles (with different materials and different sizes) embedded in and strongly coupled with a volume of gas, the radiative acceleration can be obtained by summation over the type and size of dust particles as below

$$a_{\text{clump}}^{\text{rad}} = \frac{1}{M_{\text{clump}}} \frac{z}{c} \iiint I_\lambda \, \sigma_\lambda^{\text{tot(rad)}}$$
$$\times \frac{(\rho - R\cos\varphi)\,\hat{\rho} + z\,\hat{z}}{(r^2 + R^2 - 2\rho R\cos\varphi)^2} R \, dR \, d\varphi \, d\lambda \qquad (A14)$$

where $M_{\text{clump}} = M_{\text{dust}} + M_{\text{gas}}$.

The final form of radiative acceleration for the dusty clump is

$$a_{\text{clump}}^{\text{rad}} = \frac{\Psi}{1+\Psi} \frac{z}{c} \int_{\lambda_i}^{\lambda_f} \int_{\varphi_{\min}}^{\varphi_{\max}}$$
$$\times \int_{R_{\min}}^{R_{\max}} I_\lambda \, K_\lambda^{\text{rad}} \frac{(\rho - R\cos\varphi)\,\hat{\rho} + z\,\hat{z}}{(r^2 + R^2 - 2\,\rho\,R\cos\varphi)^2} R \, dR \, d\varphi \, d\lambda \qquad (A15)$$

where Ψ is the clump dust-to-gas ratio, and K_λ^{rad} is the mean total cross section per dust mass, which resembles the definition of opacity (see Appendix A.2 for details).

Incorporating the radiation pressure on w-percent ionized gas, one can generally write

$$a_{\text{clump}}^{\text{rad}} = \frac{1}{M_{\text{clump}}} \frac{F}{c} (\sigma_{\text{dust}}^{\text{tot}} + \sigma_{\text{T}}^{\text{tot}}) \qquad (A16)$$

which can be rewritten as

$$a_{\text{clump}}^{\text{rad}} = \frac{\mathbb{F}}{c} \left(\frac{\Psi}{1+\Psi} K_{\text{dust}}^{\text{rad}} + \frac{w}{1+\Psi} \frac{\sigma_{\text{T}}^{\text{tot}}}{M_{\text{ion.gas}}} \right)$$
$$\approx \frac{\mathbb{F}}{c} \left(\Psi \, K_{\text{dust}}^{\text{rad}} + w \, \frac{\sigma_{\text{T}}}{m_{\text{p}}} \right) \qquad (A17)$$

so if the first term dominates the second term, the radiation pressure due to Thompson electron scattering can be neglected (see Figure 1).

It should be noted that we have considered the strong-coupling approximation. So the clump is a unified rigid body within which the embedded spherical dust particles and the volume of gas are spatially fixed as if wired or connected to each other. Also the clump is not of a large size, or the dust particles are mostly concentrated around its center. Otherwise, randomly oriented acceleration vectors of dust particles located at random positions within a large volume of gas will result in a different net acceleration vector. This becomes worse if there is no dust−gas strong coupling, which results in deformation, disintegration, and fragmentation of the clump.

A.2. Dust Opacity and Dust-to-gas Ratio

In order to find $\sigma_\lambda^{\text{tot(rad)}}$, assuming a dust model with a population of dust types with a given grain size distribution, we proceed with a general relation valid for grains with radius $a_- \leqslant a \leqslant a_+$ as below

$$dn_i(a) = n f_i(a) \, da = n_i(a) \, da \qquad (A18)$$

where $n_i(a)$ is the number density of grains and n is the number density of H nuclei ($n = n_{\text{H}} + 2n_{H_2}$), i stands for the dust type, and f_i is a modular function. Now one can write, for example, the total absorption cross section (the same applies to the total scattering cross section) for a given dust type as

$$\sigma_{\lambda,i}^{\text{tot(abs)}} = V_{\text{clump}} \int_{a_-^i}^{a_+^i} n_i(a) \, [\sigma(a)]_{\lambda,i}^{\text{abs}} \, da \qquad (A19)$$

where $[\sigma(a)]_{\lambda,i}^{\text{abs}}$ is the absorption cross section of a single grain of a certain sort of size a (radius) at wavelength λ, and V_{clump} is the volume of the clump. Summation over types of dust gives

$$\sigma_\lambda^{\text{tot(abs)}} = \sum_{i=1}^{\text{NDS}} \sigma_{\lambda,i}^{\text{tot(abs)}}$$
$$= V_{\text{clump}} \sum_{i=1}^{\text{NDS}} \int_{a_-^i}^{a_+^i} n_i(a) \, [\sigma(a)]_{\lambda,i}^{\text{abs}} \, da \qquad (A20)$$

where NDS is the number of dust types in the dust model. Likewise we can find $\sigma_\lambda^{\text{tot(sca)}}$ and consequently $\sigma_\lambda^{\text{tot(rad)}}$.

When calculating the radiative acceleration, it would be easier to work with general densities, ratios, and mean values rather than certain masses or volumes. Looking at Equation (A14) we can write

$$\frac{\sigma_\lambda^{\text{tot(rad)}}}{M_{\text{clump}}} = \frac{M_{\text{dust}}}{M_{\text{clump}}} \frac{\sigma_\lambda^{\text{tot(rad)}}}{M_{\text{dust}}} = \frac{\Psi}{1+\Psi} K_\lambda^{\text{rad}} \qquad (A21)$$

where K_λ^{rad} is the total opacity of the clump given by

$$K_\lambda^{\mathrm{rad}} = K_\lambda^{\mathrm{abs}} + 2K_\lambda^{\mathrm{sca}} \tag{A22}$$

where

$$K_\lambda^j = \frac{1}{\Psi} \sum_{i=1}^{\mathrm{NDS}} K_{\lambda,i}^j \Psi_i \tag{A23}$$

where

$$
\begin{aligned}
K_{\lambda,i}^j &= \frac{\sigma_{\lambda,i}^{\mathrm{tot}(j)}}{M_{\mathrm{dust},i}} \\
&= \frac{1}{\rho_{\mathrm{dust},i}} \int_{a_-^i}^{a_+^i} n_i(a) \, [\sigma(a)]_{\lambda,i}^j \, da
\end{aligned} \tag{A24}
$$

where j stands for (rad), (abs), or (sca); and Ψ is dust-to-gas mass ratio given by

$$
\begin{aligned}
\Psi &= \frac{M_{\mathrm{dust}}}{M_{\mathrm{gas}}} = \frac{\rho_{\mathrm{dust}}}{\rho_{\mathrm{gas}}} = \sum_{i=1}^{\mathrm{NDS}} \Psi_i \\
&= \frac{\sum_{i=1}^{\mathrm{NDS}} \int_{a_-^i}^{a_+^i} n_i(a) \, 4/3\pi a^3 \rho_{b,i} \, da}{n m_{\mathrm{H}}} \\
&= \frac{\sum_{i=1}^{\mathrm{NDS}} \int_{a_-^i}^{a_+^i} f_i(a) \, 4/3\pi a^3 \rho_{b,i} \, da}{m_{\mathrm{H}}}
\end{aligned} \tag{A25}
$$

where $\rho_{b,i}$ is the bulk dust density of type i, and m_{H} is the mass of H nuclei.

A.3. Dust Sublimation

Assuming instantaneous re-emission of the absorbed radiation by dust in the form of isotropic blackbody radiation, if the amount of heat absorbed by the dusty content of the clump increases its temperature to that of sublimation, the radiative engine of motion of the clump switches off. So the criterion for the sublimation of dusty content is

$$E_{\mathrm{abs}} = E_{\mathrm{emit}}(T_s). \tag{A26}$$

The total radiative energy by definition (Mihalas 1978) is

$$E = \int I_\lambda(\mathbf{r}, \hat{\mathbf{n}}) \cos(\alpha) \, d\lambda \, dA \, d\Omega \, dt. \tag{A27}$$

So the radiative energy absorbed by dust is

$$E_{\mathrm{abs}} = \int I_\lambda \, \sigma_\lambda^{\mathrm{tot}(\mathrm{abs})} \, d\lambda \, d\Omega \, dt \tag{A28}$$

and the energy re-emitted by dust (Loska et al. 1993) at the sublimation temperature (T_s) is

$$E_{\mathrm{emit}}(T_s) = 4\pi \int B_\lambda(T_s) \, \sigma_\lambda^{\mathrm{tot}(\mathrm{abs})} \, d\lambda \, dt. \tag{A29}$$

Dividing both sides of Equation (A26) by dt and M_{dust} we can introduce Q (the total power per dust mass), so we have $Q_{\mathrm{abs}} = Q_{\mathrm{emit}}(T_s)$ for the sublimation criterion where

$$Q_{\mathrm{emit}}(T_s) = 4\pi \int B_\lambda(T_s) \, K_\lambda^{\mathrm{abs}} \, d\lambda \tag{A30}$$

$$Q_{\mathrm{abs}} = \int I_\lambda \, K_\lambda^{\mathrm{abs}} \, d\lambda \, d\Omega \tag{A31}$$

so we have

$$
\begin{aligned}
Q_{\mathrm{abs}} = {}& z \int_{\lambda_i}^{\lambda_f} \int_{\varphi_{\min}}^{\varphi_{\max}} \int_{R_{\min}}^{R_{\max}} \frac{I_\lambda \, K_\lambda^{\mathrm{abs}}}{(r^2 + R^2 - 2\rho R \cos\varphi)^{3/2}} \\
& \times R \, dR \, d\varphi \, d\lambda.
\end{aligned} \tag{A32}
$$

ORCID iDs

Mohammad-Hassan Naddaf ⬤ https://orcid.org/0000-0002-7604-9594
Bożena Czerny ⬤ https://orcid.org/0000-0001-5848-4333
Ryszard Szczerba ⬤ https://orcid.org/0000-0003-2886-4460

References

Adhikari, T. P. 2019, Photoionization Modelling as a Density Diagnostic of Line Emitting/Absorbing Regions in Active Galactic Nuclei (Cham: Springer International Publishing)
Adhikari, T. P., Hryniewicz, K., Różańska, A., Czerny, B., & Ferland, G. J. 2018, ApJ, 856, 78
Adhikari, T. P., Różańska, A., Czerny, B., Hryniewicz, K., & Ferland, G. J. 2016, ApJ, 831, 68
Antonucci, R. R. J., & Miller, J. S. 1985, ApJ, 297, 621
Balbus, S. A., & Hawley, J. F. 1991, ApJ, 376, 214
Baldwin, J. A., Ferland, G. J., Korista, K. T., Hamann, F., & LaCluyzé, A. 2004, ApJ, 615, 610
Barvainis, R. 1987, ApJ, 320, 537
Baskin, A., & Laor, A. 2018, MNRAS, 474, 1970
Begelman, M. C., McKee, C. F., & Shields, G. A. 1983, ApJ, 271, 70
Bianchi, S., Maiolino, R., & Risaliti, G. 2012, AdAst, 2012, 782030
Blandford, R. D., & Begelman, M. C. 1999, MNRAS, 303, L1
Blandford, R. D., & McKee, C. F. 1982, ApJ, 255, 419
Blandford, R. D., & Payne, D. G. 1982, MNRAS, 199, 883
Borguet, B. C. J., Arav, N., Edmonds, D., Chamberlain, C., & Benn, C. 2013, ApJ, 762, 49
Boroson, T. A., & Green, R. F. 1992, ApJS, 80, 109
Brotherton, M. S., Wills, B. J., Steidel, C. C., & Sargent, W. L. W. 1994, ApJ, 423, 131
Capriotti, E., Foltz, C., & Byard, P. 1980, ApJ, 241, 903
Chan, C.-H., & Krolik, J. H. 2016, ApJ, 825, 67
Chan, C.-H., & Krolik, J. H. 2017, ApJ, 843, 58
Chau Giang, N., & Hoang, T. 2020, arXiv:2009.06958
Clavel, J., Wamsteker, W., & Glass, I. S. 1989, ApJ, 337, 236
Collin, S., & Zahn, J.-P. 1999, A&A, 344, 433
Collin, S., & Zahn, J. P. 2008, A&A, 477, 419
Collin-Souffrin, S., Dyson, J. E., McDowell, J. C., & Perry, J. J. 1988, MNRAS, 232, 539
Costa, T., Pakmor, R., & Springel, V. 2020, MNRAS, 497, 5229
Costa, T., Rosdahl, J., Sijacki, D., & Haehnelt, M. G. 2018, MNRAS, 473, 4197
Croton, D. J., Springel, V., White, S. D. M., et al. 2006, MNRAS, 365, 11
Czerny, B., Du, P., Wang, J.-M., & Karas, V. 2016, ApJ, 832, 15
Czerny, B., & Hryniewicz, K. 2011, A&A, 525, L8
Czerny, B., Li, J., Loska, Z., & Szczerba, R. 2004a, MNRAS, 348, L54
Czerny, B., Li, Y.-R., Hryniewicz, K., et al. 2017, ApJ, 846, 154
Czerny, B., Modzelewska, J., Petrogalli, F., et al. 2015, AdSpR, 55, 1806
Czerny, B., Olejak, A., Rałowski, M., et al. 2019, ApJ, 880, 46
Czerny, B., Rózańska, A., & Kuraszkiewicz, J. 2004b, A&A, 428, 39
Davis, S. W., Jiang, Y.-F., Stone, J. M., & Murray, N. 2014, ApJ, 796, 107
Done, C., & Krolik, J. H. 1996, ApJ, 463, 144
Donea, A.-C., & Protheroe, R. J. 2002, PASA, 19, 39
Dong, X., Wang, T., Wang, J., et al. 2008, MNRAS, 383, 581
Dorodnitsyn, A., Kallman, T., & Bisnovatyi-Kogan, G. S. 2012, ApJ, 747, 8
Du, P., Lu, K.-X., Zhang, Z.-X., et al. 2016, ApJ, 825, 126
Du, P., & Wang, J.-M. 2019, ApJ, 886, 42
Elitzur, M., & Shlosman, I. 2006, ApJL, 648, L101
Elvis, M. 2000, ApJ, 545, 63
Elvis, M., Marengo, M., & Karovska, M. 2002, ApJL, 567, L107
Everett, J. E. 2005, ApJ, 631, 689
Feldmeier, A., & Shlosman, I. 1999, ApJ, 526, 344

Figaredo, C. S., Haas, M., Ramolla, M., et al. 2020, AJ, 159, 259
Fonseca Alvarez, G., Trump, J. R., Homayouni, Y., et al. 2020, ApJ, 899, 73
Fukumura, K., Tombesi, F., Kazanas, D., et al. 2015, ApJ, 805, 17
Gallagher, S. C., & Everett, J. E. 2007, in ASP Conf. Ser. 373, The Central Engine of Active Galactic Nuclei, ed. L. C. Ho & J. W. Wang (San Francisco, CA: ASP), 305
Gallagher, S. C., Everett, J. E., Abado, M. M., & Keating, S. K. 2015, MNRAS, 451, 2991
Gaskell, C. M. 2009, NewAR, 53, 140
Gaskell, C. M., Goosmann, R. W., Antonucci, R. R. J., & Whysong, D. H. 2004, ApJ, 616, 147
Gnat, O., & Ferland, G. J. 2012, ApJS, 199, 20
Goad, M. R., Korista, K. T., & Ruff, A. J. 2012, MNRAS, 426, 3086
Goldman, S. R., van Loon, J. T., Zijlstra, A. A., et al. 2017, MNRAS, 465, 403
Gravity Collaboration, Amorim, A., Bauböck, M., et al. 2021, A&A, 648, A117
Gravity Collaboration, Dexter, J., Shangguan, J., et al. 2020, A&A, 635, A92
Gravity Collaboration, Sturm, E., Dexter, J., et al. 2018, Natur, 563, 657
Grier, C. J., Peterson, B. M., Horne, K., et al. 2013, ApJ, 764, 47
Gronke, M., & Oh, S. P. 2020, MNRAS, 494, L27
Grzedzielski, M., Janiuk, A., Czerny, B., & Wu, Q. 2017, A&A, 603, A110
Hagino, K., Odaka, H., Done, C., et al. 2015, MNRAS, 446, 663
Harrison, C. M., Alexander, D. M., Mullaney, J. R., & Swinbank, A. M. 2014, MNRAS, 441, 3306
Higginbottom, N., Knigge, C., Long, K. S., Sim, S. A., & Matthews, J. H. 2013, MNRAS, 436, 1390
Higginbottom, N., Proga, D., Knigge, C., et al. 2014, ApJ, 789, 19
Hirai, Y., & Fukue, J. 2001, PASJ, 53, 285
Hönig, S. F. 2019, ApJ, 884, 171
Hopkins, P. F., & Elvis, M. 2010, MNRAS, 401, 7
Hopkins, P. F., Strauss, M. A., Hall, P. B., et al. 2004, AJ, 128, 1112
Hosseinirad, M., Abbassi, S., Roshan, M., & Naficy, K. 2018, MNRAS, 475, 2632
Hu, C., Wang, J.-M., Ho, L. C., et al. 2008, ApJ, 687, 78
Huang, X., Davis, S. W., & Zhang, D. 2020, ApJ, 893, 50
Icke, V. 1980, AJ, 85, 329
Ishibashi, W., Banerji, M., & Fabian, A. C. 2017, MNRAS, 469, 1496
Ishibashi, W., & Fabian, A. C. 2015, MNRAS, 451, 93
Joly, M. 1987, A&A, 184, 33
Jun, H. D., Assef, R. J., Carroll, C. M., et al. 2021, ApJ, 906, 21
Kartje, J. F., Königl, A., & Elitzur, M. 1999, ApJ, 513, 180
Kawaguchi, T., & Mori, M. 2010, ApJL, 724, L183
Kawaguchi, T., & Mori, M. 2011, ApJ, 737, 105
Khajenabi, F. 2016, ApJ, 828, 9
Kishimoto, M., Hönig, S. F., Antonucci, R., et al. 2009, A&A, 507, L57
Kishimoto, M., Hönig, S. F., Antonucci, R., et al. 2011, A&A, 527, A121
Konigl, A., & Kartje, J. F. 1994, ApJ, 434, 446
Koshida, S., Minezaki, T., Yoshii, Y., et al. 2014, ApJ, 788, 159
Krause, M., Burkert, A., & Schartmann, M. 2011, MNRAS, 411, 550
Lawrence, A., & Elvis, M. 2010, ApJ, 714, 561
Lawrence, A., Elvis, M., Wilkes, B. J., McHardy, I., & Brandt, N. 1997, MNRAS, 285, 879
Le, H. A. N., & Woo, J.-H. 2019, ApJ, 887, 236
Leftley, J. H., Hönig, S. F., Asmus, D., et al. 2019, ApJ, 886, 55
Li, A. 2007, in ASP Conf. Ser. 373, The Central Engine of Active Galactic Nuclei, ed. L. C. Ho & J. W. Wang (San Francisco, CA: ASP), 561
Li, Y.-R., Wang, J.-M., & Bai, J.-M. 2016, ApJ, 831, 206
Liu, Y., & Zhang, S. N. 2011, ApJL, 728, L44
Loska, Z., Szczerba, R., & Czerny, B. 1993, MNRAS, 261, 63
Marconi, A., Axon, D. J., Maiolino, R., et al. 2008, ApJ, 678, 693
Markowitz, A. G., Krumpe, M., & Nikutta, R. 2014, MNRAS, 439, 1403
Martínez-Aldama, M. L., Zajaček, M., Czerny, B., & Panda, S. 2020, ApJ, 903, 86
Mas-Ribas, L. 2019, ApJ, 885, 95
Mas-Ribas, L., & Mauland, R. 2019, ApJ, 886, 151
Mathis, J. S., Rumpl, W., & Nordsieck, K. H. 1977, ApJ, 217, 425
Matthews, J. H., Knigge, C., Higginbottom, N., et al. 2020, MNRAS, 492, 5540
McCourt, M., Oh, S. P., O'Leary, R., & Madigan, A.-M. 2018, MNRAS, 473, 5407
McCourt, M., O'Leary, R. M., Madigan, A.-M., & Quataert, E. 2015, MNRAS, 449, 2
Mihalas, D. 1978, Stellar Atmospheres (2nd ed.; San Francisco, CA: Freeman)
Minezaki, T., Yoshii, Y., Kobayashi, Y., et al. 2019, ApJ, 886, 150
Miniutti, G., Saxton, R. D., Rodríguez-Pascual, P. M., et al. 2013, MNRAS, 433, 1764

Mioc, V., & Radu, E. 1992, AN, 313, 353
Mizumoto, M., Done, C., Tomaru, R., & Edwards, I. 2019, MNRAS, 489, 1152
Mizumoto, M., Nomura, M., Done, C., Ohsuga, K., & Odaka, H. 2021, MNRAS, 503, 1442
Mosallanezhad, A., Yuan, F., Ostriker, J. P., Zeraatgari, F. Z., & Bu, D.-F. 2019, MNRAS, 490, 2567
Muijres, L. E., de Koter, A., Vink, J. S., et al. 2011, A&A, 526, A32
Murray, N., & Chiang, J. 1995, ApJL, 454, L105
Murray, N., Chiang, J., Grossman, S. A., & Voit, G. M. 1995, ApJ, 451, 498
Naddaf, M.-H., Czerny, B., & Szczerba, R. 2020, FrASS, 7, 15
Netzer, H. 2013, The Physics and Evolution of Active Galactic Nuclei (Cambridge: Cambridge University Press)
Netzer, H. 2015, ARA&A, 53, 365
Netzer, H., & Laor, A. 1993, ApJL, 404, L51
Netzer, H., Lutz, D., Schweitzer, M., et al. 2007, ApJ, 666, 806
Netzer, H., & Marziani, P. 2010, ApJ, 724, 318
Nomura, M., Ohsuga, K., & Done, C. 2020, MNRAS, 494, 3616
Nomura, M., Ohsuga, K., Wada, K., Susa, H., & Misawa, T. 2013, PASJ, 65, 40
Oknyansky, V. L., Gaskell, C. M., & Shimanovskaya, E. V. 2015, OAP, 28, 175
Osterbrock, D. E. 1978, PhyS, 17, 285
Pancoast, A., Brewer, B. J., & Treu, T. 2011, ApJ, 730, 139
Pancoast, A., Brewer, B. J., & Treu, T. 2014, MNRAS, 445, 3055
Panda, S. 2020, A&A, 650, A154
Panda, S., Czerny, B., Adhikari, T. P., et al. 2018, ApJ, 866, 115
Panda, S., Czerny, B., Done, C., & Kubota, A. 2019a, ApJ, 875, 133
Panda, S., Martínez-Aldama, M. L., Marinello, M., et al. 2020a, ApJ, 902, 76
Panda, S., Marziani, P., & Czerny, B. 2019b, ApJ, 882, 79
Panda, S., Marziani, P., & Czerny, B. 2020b, CoSka, 50, 293
Peißker, F., Eckart, A., Sabha, N. B., Zajaček, M., & Bhat, H. 2020, ApJ, 897, 28
Pereyra, N. A., Kallman, T. R., & Blondin, J. M. 1997, ApJ, 477, 368
Peterson, B. M. 1993, PASP, 105, 247
Peterson, B. M., & Horne, K. 2004, AN, 325, 248
Peterson, B. M., Wanders, I., Horne, K., et al. 1998, PASA, 110, 660
Pietrini, P., Torricelli-Ciamponi, G., & Risaliti, G. 2019, A&A, 628, A26
Plewa, P. M., Schartmann, M., & Burkert, A. 2013, MNRAS, 431, L127
Pott, J.-U., Malkan, M. A., Elitzur, M., et al. 2010, ApJ, 715, 736
Proga, D. 2007, ApJ, 661, 693
Proga, D., & Kallman, T. R. 2004, ApJ, 616, 688
Proga, D., Stone, J. M., & Drew, J. E. 1998, MNRAS, 295, 595
Proga, D., Stone, J. M., & Drew, J. E. 1999, MNRAS, 310, 476
Proga, D., Stone, J. M., & Kallman, T. R. 2000, ApJ, 543, 686
Proga, D., & Waters, T. 2015, ApJ, 804, 137
Raimundo, S. I., Vestergaard, M., Goad, M. R., et al. 2020, MNRAS, 493, 1227
Raouf, M., Silk, J., Shabala, S. S., et al. 2019, MNRAS, 486, 1509
Rees, M. J., Silk, J. I., Werner, M. W., & Wickramasinghe, N. C. 1969, Natur, 223, 788
Reeves, J. N., & Turner, M. J. L. 2000, MNRAS, 316, 234
Reissl, S., Klessen, R. S., Mac Low, M.-M., & Pellegrini, E. W. 2018, A&A, 611, A70
Richards, G. T., Hall, P. B., Vanden Berk, D. E., et al. 2003, AJ, 126, 1131
Rieke, G. H. 1978, ApJ, 226, 550
Risaliti, G., & Elvis, M. 2010, A&A, 516, A89
Risaliti, G., Nardini, E., Salvati, M., et al. 2011, MNRAS, 410, 1027
Różańska, A., Czerny, B., Życki, P. T., & Pojmański, G. 1999, MNRAS, 305, 481
Różańska, A., Goosmann, R., Dumont, A. M., & Czerny, B. 2006, A&A, 452, 1
Röllig, M., Szczerba, R., Ossenkopf, V., & Glück, C. 2013, A&A, 549, A85
Saslaw, W. C. 1978, ApJ, 226, 240
Schmidt, M. 1963, Natur, 197, 1040
Schnülle, K., Pott, J. U., Rix, H. W., et al. 2015, A&A, 578, A57
Semenov, D., Henning, T., Helling, C., Ilgner, M., & Sedlmayr, E. 2003, A&A, 410, 611
Seyfert, C. K. 1943, ApJ, 97, 28
Shadmehri, M. 2015, MNRAS, 451, 3671
Shakura, N. I., & Sunyaev, R. A. 1973, A&A, 500, 33
Shangguan, J., Ho, L. C., & Xie, Y. 2018, ApJ, 854, 158
Shapovalova, A. I., Popović, L. Č., Burenkov, A. N., et al. 2010, A&A, 509, A106
Shen, Y., Richards, G. T., Strauss, M. A., et al. 2011, ApJS, 194, 45
Shin, M.-S., Stone, J. M., & Snyder, G. F. 2008, ApJ, 680, 336

Shlosman, I., Vitello, P. A., & Shaviv, G. 1985, ApJ, 294, 96
Sim, S. A., Proga, D., Miller, L., Long, K. S., & Turner, T. J. 2010, MNRAS, 408, 1396
Suganuma, M., Yoshii, Y., Kobayashi, Y., et al. 2006, ApJ, 639, 46
Sulentic, J. W., Marziani, P., & Dultzin-Hacyan, D. 2000, ARA&A, 38, 521
Swain, M., Vasisht, G., Akeson, R., et al. 2003, ApJL, 596, L163
Szczerba, R., Omont, A., Volk, K., Cox, P., & Kwok, S. 1997, A&A, 317, 859
Tazaki, R., Ichikawa, K., & Kokubo, M. 2020, ApJ, 892, 84
Temple, M. J., Banerji, M., Hewett, P. C., Rankine, A. L., & Richards, G. T. 2020, MNRAS, 501, 3061
Thompson, T. A., Fabian, A. C., Quataert, E., & Murray, N. 2015, MNRAS, 449, 147
Torricelli-Ciamponi, G., Pietrini, P., Risaliti, G., & Salvati, M. 2014, MNRAS, 442, 2116
Tsang, B. T. H., & Milosavljević, M. 2015, MNRAS, 453, 1108
Ventura, P., di Criscienzo, M., Schneider, R., et al. 2012, MNRAS, 420, 1442
Vinković, D., & Čemeljić, M. 2021, MNRAS, 500, 506
Voit, G. M. 1992, MNRAS, 258, 841
Wada, K. 2012, ApJ, 758, 66
Wandel, A., Peterson, B. M., & Malkan, M. A. 1999, ApJ, 526, 579
Wang, H., Xing, F., Zhang, K., et al. 2013, ApJL, 776, L15
Wang, J.-M., Cheng, C., & Li, Y.-R. 2012a, ApJ, 748, 147
Wang, J.-M., Du, P., Baldwin, J. A., et al. 2012b, ApJ, 746, 137
Wang, J.-M., Du, P., Brotherton, M. S., et al. 2017, NatAs, 1, 775
Wang, J.-M., Ge, J.-Q., Hu, C., et al. 2011, ApJ, 739, 3
Wang, J.-M., Qiu, J., Du, P., & Ho, L. C. 2014, ApJ, 797, 65
Ward, R. L., Wadsley, J., & Sills, A. 2014, MNRAS, 445, 1575
Watarai, K.-y., & Fukue, J. 1999, PASJ, 51, 725
Waters, T., Kashi, A., Proga, D., et al. 2016, ApJ, 827, 53
Waters, T., & Proga, D. 2016, MNRAS, 460, L79
Waters, T., & Proga, D. 2019, ApJ, 875, 158
Waters, T., Proga, D., & Dannen, R. 2021, ApJ, 914, 62
Weingartner, J. C., & Draine, B. T. 2001, ApJ, 548, 296
Williamson, D., Hönig, S., & Venanzi, M. 2019, ApJ, 876, 137
Witt, H. J., Czerny, B., & Zycki, P. T. 1997, MNRAS, 286, 848
Zafar, T., Møller, P., Watson, D., et al. 2015, A&A, 584, A100
Zajaček, M., Czerny, B., Martinez-Aldama, M. L., et al. 2020, ApJ, 896, 146
Zajaček, M., Czerny, B., Martinez-Aldama, M. L., et al. 2021, ApJ, 912, 10
Zhang, D., & Davis, S. W. 2017, ApJ, 839, 54
Zhang, D., Davis, S. W., Jiang, Y.-F., & Stone, J. M. 2018, ApJ, 854, 110
Zhang, X., He, Z., Wang, T., & Guo, H. 2021, ApJ, 914, 143

Chapter 4

Paper II: BLR size in realistic FRADO model: The role of shielding effect

BLR Size in Realistic FRADO Model: The Role of Shielding Effect

Mohammad-Hassan Naddaf [1,2]*, Bożena Czerny [1] and Ryszard Szczerba [3]

[1] Center for Theoretical Physics, Warsaw, Poland, [2] Nicolaus Copernicus Astronomical Center, Warsaw, Poland, [3] Nicolaus Copernicus Astronomical Center, Torun, Poland

The effective size of broad line region (BLR), so-called the BLR radius, in galaxies with active galactic nuclei (AGN) scales with the source luminosity. Therefore, by determining this location either observationally through reverberation mapping or theoretically, one can use AGNs as an interesting laboratory to test cosmological models. In this article we focus on the theoretical side of BLR based on the Failed Radiatively Accelerated Dusty Outflow (FRADO) model. By simulating the dynamics of matter in BLR through a realistic model of radiation of accretion disk (AD) including the shielding effect, as well as incorporating the proper values of dust opacities, we investigate how the radial extension and geometrical height of the BLR depends on the Eddington ratio [and blackhole mass], and modeling of shielding effect. We show that assuming a range of Eddington ratios and shielding we are able to explain the time-delays in a sample of reverberation-measured AGNs.

Keywords: active galaxies, broad line region, FRADO model, shielding effect, dust opacity

1. INTRODUCTION

The delayed response of BLR to the variation of AGNs continuum is a probe to study the structure of BLR (Peterson et al., 1998). The main discovery is a linear log — log scaling law between the size of BLR and the AGN monochromatic luminosity, so-called the radius-luminosity (RL) relation. It has been observationally discovered (Kaspi et al., 2000; Peterson et al., 2004; Bentz et al., 2009, 2013), and theoretically explained by Czerny and Hryniewicz (2011) who proposed that failed dust-driven wind (FRADO) is responsible for the formation of BLR. However, the departures from the law seen for some sources with high Eddington ratios (Du et al., 2015, 2016, 2018; Grier et al., 2017), obviously requires the structure and extension of BLR to be studied in more detail, not only in observational side via reverberation-mapping (e.g., Panda et al., 2019), but also through theoretically-motivated models. Provided that the RL relation is concretely justified for all already-observed sources (Martínez-Aldama et al., 2019; Rakshit et al., 2019), AGNs can be treated as astronomical candles to be used in cosmology (Haas et al., 2011; Watson et al., 2011).

In this article, we briefly report our pilot numerical study on the size of BLR based on the FRADO model. A concise background on the existing BLR models is addressed in section 2. In section 3 an introduction to FRADO model is provided, followed by section 4 on shielding effect. After a short description of our numerical setup in section 5, the method we adopted to find the BLR size is specified in section 6. We discuss our results and conclude the article in the last two sections.

2. BLR MODELS

Broad Emission Lines are the most characteristic property of the AGN spectra known since many years (for a review, see Netzer, 2015). However, the formation of BLR is not clear and still under debate. Different scenarios about the origin of the BLR material have been discussed during years. The proposed mechanisms can be divided into: Inflow Models (Hu et al., 2008; Wang et al., 2017), Disk Instabilities (Collin and Zahn, 1999, 2008; Wang et al., 2011, 2012), or Disk Winds/Outflows. The latter class of models includes Magnetically-Driven winds (Blandford and Payne, 1982; Emmering et al., 1992; Elitzur et al., 2014), Thermally-Driven winds (Begelman et al., 1983; Czerny and King, 1989; Witt et al., 1997; Blandford and Begelman, 1999), and Radiatively-Driven winds consisting of Line-Driven winds (Murray et al., 1995; Risaliti and Elvis, 2010), and newly-born models of Dust-Driven winds.

The first model in the category of Dust-driven Winds is FRADO model (Czerny and Hryniewicz, 2011; Czerny et al., 2015, 2017). There is only another existing model in this category for the formation of BLR in which the static atmosphere of disk is puffed up by irradiation in the dust-dominated region (Baskin and Laor, 2018). Differently from this static model, FRADO gives a dynamic view of the BLR. The advantage of the FRADO model is that the underlying physics is known, the approximate compensation of the inflow/outflow leads to approximately symmetric lines, and the model is likely to produce also single component line instead of disky profiles if the vertical motion is strong, as expected at higher Eddington ratios. However, the model applies only to Low Ionization Lines (LIL), and for High Ionization Lines (HIL) a line-driven outflow is likely favored.

3. FRADO MODEL

FRADO model is one of the interesting theoretically-based models explaining the formation mechanism of the BLR in AGNs. It is based on the existence of dust at large radii where the AD atmosphere is cold enough (Dong et al., 2008). The dusty material, i.e., clumps composed of dust and gas, is lifted up by the AD local radiation flux. Once reaching considerably high altitudes above the disk surface, dust content of clump gets evaporated by the strong radiation coming from the central parts of an AGN and then follows a subsequent ballistic motion and forms a failed wind.

In the basic 1-D analytical form of FRADO model, only the vertical component of local flux of accretion disk at a given radius was considered. It directly gives the inner/outer radius of BLR. Asymmetry in line profiles can be seen due to the dust evaporation; line shape parameter FWHM/σ is consistent with data; and also the model predicts the dependence of virial factor on blackhole mass (Czerny et al., 2015, 2016, 2017). However, the analytical local flux of Shakura-Sunyaev (S-S) disk (Shakura and Sunyaev, 1973) that is used in this model is constant with height; radiation from other radii and also the radial motion of material are neglected, as well as the inner boundary condition in S-S AD.

In this paper, for the first time we calculate the realistic 3-D radiation pressure of AD in which the radiation coming from other radii is also contributing. The real dust opacities are also

taken into account, and the inner boundary condition of S-S AD is included. The general form of the 3-D equation of motion, considering the forces acting on the clump to be the gravity of central blackhole and radiative force of AD, is thus given as below

$$\frac{d^2\mathbf{r}}{dt^2} = -\frac{GM_{\text{BH}}}{r^3}\mathbf{r} +$$
$$\int_{\lambda_i}^{\lambda_f}\int_{\text{visible area}} f\left(\mathbf{r}, \psi, M_{\text{BH}}, \dot{m}, \kappa_{\text{ext}}(\lambda),\right.$$
$$\left. T_{\text{sub}}, \rho, \varphi, \lambda, C\right) d\mathbf{a}\, d\lambda \qquad (1)$$

where G is the gravitational constant, M_{BH} the blackhole mass, ψ the dust-to-gas mass ratio, κ_{ext} the dust opacity as a function of wavelength, $\dot{m}$ the dimensionless accretion rate, T_{sub} the dust sublimation temperature, and $\mathbf{r} = R\hat{R} + H\hat{z}$ is the vector showing the position of the clump in cylindrical coordinates in which the blackhole is at the origin as shown in **Figure 1A**. The AD for simplicity is mapped onto the equatorial plane ($z = 0$) from which the clump's height is measured. The parameters of ρ and φ show the coordinates of infinitesimal surface areas of AD in polar coordinates, and C stands for some fixed factors and physical constants. The vector radiative force acting on a clump is calculated through a double integral evaluation over AD surface (*visible area* due to shielding effect) and an integral over the effective range of wavelengths for the adopted dust model of the clump.

The effect of the dust evaporation is also included; assuming dust instantly emits the absorbed energy in the form of blackbody radiation, we numerically calculate the irradiated energy absorbed by dust Q_{abs} at each integration step. Once the Q_{abs} for a dusty clump reaching a certain altitude above AD exceeds the level of energy emission corresponding to sublimation temperature of dust $Q_{\text{emit}}(T_{\text{sub}})$, the clump loses its dust content. The radiation pressure force is then immediately switched off and the dustless cloud follows a ballistic motion, finally falling back onto the AD surface. The subsequent motion of ionized dustless gas driven by Thompson electron scattering is neglected.

4. SHIELDING EFFECT

It is well-known from all radiatively-driven wind models that efficient alleviation of the material above the disk is not possible if the wind launching region is irradiated (see e.g., Proga, 2007). Some shielding is necessary, and it can be due to either inner failed Compton-driven wind or cold material forming at the edge between the inner hot ADAF (Advection Dominated Accretion Flow) and a cold disk. This shielding effect protects dusty material from too intense radiation from the central parts of AD, including X-rays. Therefore, it would make the local radiation pressure from the disk to be effective in launching the material upward avoiding too early dust evaporation in the cloud. In order to mimic this effect we model it in the following two configurations:

- Patch Model

    In this model it is assumed that the radiation only comes from a small patch of the disk as shown in **Figure 1A**. The
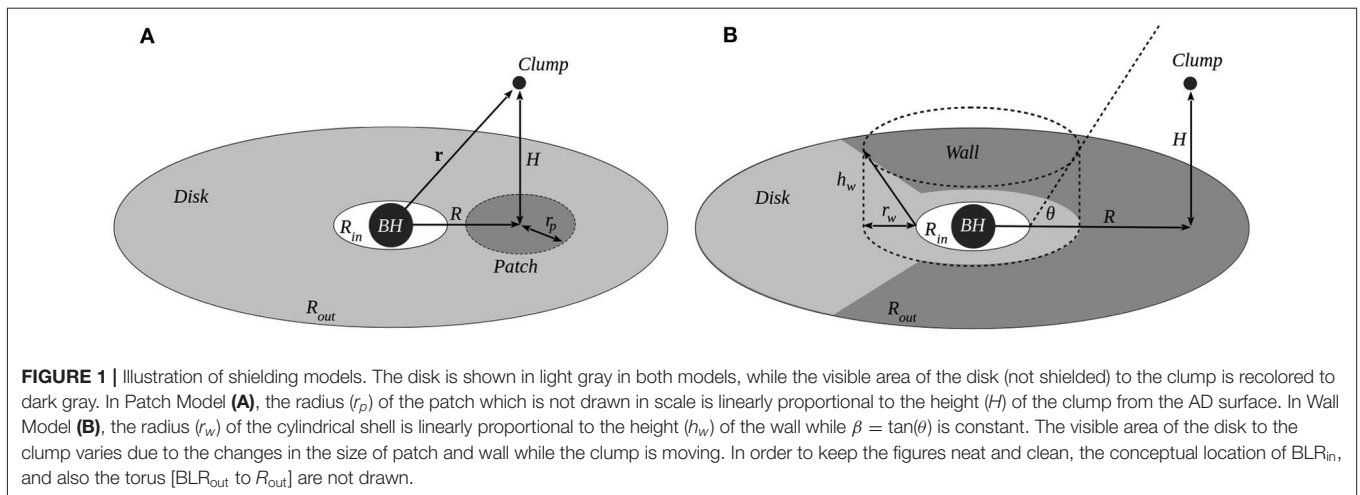
FIGURE 1 | Illustration of shielding models. The disk is shown in light gray in both models, while the visible area of the disk (not shielded) to the clump is recolored to dark gray. In Patch Model **(A)**, the radius (r_p) of the patch which is not drawn in scale is linearly proportional to the height (H) of the clump from the AD surface. In Wall Model **(B)**, the radius (r_w) of the cylindrical shell is linearly proportional to the height (h_w) of the wall while $\beta = \tan(\theta)$ is constant. The visible area of the disk to the clump varies due to the changes in the size of patch and wall while the clump is moving. In order to keep the figures neat and clean, the conceptual location of BLR$_{in}$, and also the torus [BLR$_{out}$ to R_{out}] are not drawn.

radius of patch is proportional to the height of the clump from the disk surface. Mathematically speaking, this dynamically variable radius can be expressed as a function of clump's height as $r_p = \alpha H$ where α is a free constant parameter of the model. The location of patch moves passively with the clump and increases/decreases in size as the cloud goes up/comes down.

- Wall Model

 In this model as shown in **Figure 1B**, as long as the clump is at rest on the AD surface, the radiation due to inner region of AD extending from inner radius of AD (R_{in}) up to half of the radial position of the clump ($R/2$) is shielded. The model can be illustrated as a circular wall barrier (cylindrical shell) surrounding the inner region of the AD whose radius and height are r_w and $h_w = \beta\, r_w$, respectively; where the model constant parameter $\beta = \tan(\theta)$. The range of variation for r_w is $\min(r_w) = R_{in}$ and $\max(r_w) = R_{out}/2$. Moreover, until the clump to be launched, the wall also obscures the radiation of almost half of the AD located behind the wall (viewed from the clump). As the clump flies up, due to an anti-correlation between the wall's radius and the clump's height, the wall shifts inwards while β is constant. As a result the clump sees a larger portion of AD irradiating. The moments when the clump is flying in an altitude $H > \beta R$ above AD, it can be irradiated by the whole AD as if there is no shielding effect.

Obviously, the proposed models of shielding are geometrically different. The results from these models can provide us with useful information about how shielding effect really looks like, and how effective it is in the physics of BLR and its dynamics. We incorporate these shielding models into our computations by imposing proper dynamic upper-lower integral limits while evaluating the radiative force produced by AD.

5. NUMERICAL SETUP

In order to perform the simulation, we consider the following setup. The blackhole mass is set to be of $10^8 M_\odot$ (Panda et al.,

2018) which is almost the mean value of the blackhole mass in quasar catalog of Shen et al. (2011). The underlying disk is the S-S disk model which radiates locally as a blackbody. We consider a range of AD radii from $R_{in} = 6R_g$ to $R_{out} = 10^6 R_g$ where R_g is the gravitational radius of the blackhole defined as $R_g = GM_{BH}/c^2$. The adopted dimensionless accretion rates ($\dot{m} = \dot{M}/\dot{M}_{Edd}$ where $\dot{M}_{Edd}$ is the Eddington accretion rate) are 0.01, 0.1, and 1. Actual values of wavelength-dependent dust opacity are incorporated into our computation. These values are computed using MCDRT (Szczerba et al., 1997) and KOSMA–τ PDR (Röllig et al., 2013) codes which give the mean extinction cross-section per dust mass (equivalent to opacity) for different dust models with a given distribution of dust grain size and different materials. We employ the MRN dust model (Mathis et al., 1977) which consists of silicate and graphite and has an identical grain size distribution for both dust populations. Silicate features are seen in the AGN spectra (e.g., Netzer et al., 2007); graphite is more problematic, we would rather expect amorphous grains at the basis of the UV spectra (see e.g., Czerny et al., 2004), but we use MRN for simplicity. Moreover, having assumed the gas and dust within the clump being strongly coupled we set the parameter ψ equal to 0.005 which is the mean value for Milky Way (Mathis et al., 1977). However, an estimate mean ratio of 0.008 is also adopted by others for a sample of AGNs (Shangguan et al., 2018). It is also assumed that the dust content of clumps sublimates at a temperature of 1500 K which represents approximately the mean value for the different grain species and sizes (see Baskin and Laor, 2018). The clumps in our model are launched with an azimuthal Keplerian velocity and zero vertical velocity from the surface of AD which has a thickness, $D(R)$. The latter, which is function of radius, was computed separately for different initial values of AD size, accretion rate, black hole mass, and viscosity based on Rosseland mean opacity (Różańska et al., 1999; Czerny et al., 2016) without the effect of AD self-gravity being included. This implicitly also means that the height of the clump (H) never vanishes since our mathematically thin disk is at $z = 0$. The Runge-Kutta method is then applied in order to integrate the equations of motion.

TABLE 1 | Output data for the size of BLR for blackhole mass of $10^8 M_\odot$.

							$i = 39.2$	
Shielding model	$\dot{m}$	$\mathrm{BLR_{in}}$	$\mathrm{BLR_{out}}$	P_{peak}	$R(P_{\mathrm{peak}})$	$\log(L_{5100})$	$\log(\tau_{\mathrm{in}})$	$\log(\tau_{\mathrm{peak}})$
	0.01	4.95	112.53	0.027	4.96	43.81	0.9067 >	0.9027
$\alpha = 1.0$	0.10	9.45	356.71	0.105	9.64	44.52	1.1867 >	1.1761
	1.00	18.00	1126.75	0.358	27.42	45.21	1.4639 <	1.5894
	0.01	5.19	112.53	0.031	5.21	43.81	0.9273 >	0.9233
$\alpha = 1.5$	0.10	9.92	356.71	0.117	10.25	44.52	1.2078 >	1.2005
	1.00	18.89	1126.75	0.351	46.97	45.21	1.4853 <	1.8241
	0.01	5.31	112.53	0.032	5.32	43.81	0.9372 >	0.9321
$\alpha = 2.0$	0.10	10.13	356.71	0.122	10.61	44.52	1.2169 >	1.2146
	1.00	19.29	1126.75	0.346	[a]31.72	45.21	1.4944 <	1.6543
$\alpha = 2.0$ $(10^7 M_\odot)$	0.10	2.06	–	0.045	2.07	43.21	0.5256 >	0.5196
$\alpha = 2.0$ $(10^9 M_\odot)$	0.10	49.76	–	0.270	75.25	45.81	1.9067 <	2.0228
	0.01	5.49	112.53	0.034	5.63	43.81	0.9517 <	0.9563
$\beta = 0.3$	0.10	10.48	356.71	0.115	12.71	44.52	1.2319 <	1.2943
	1.00	20.03	1126.75	0.245	[a]39.84	45.21	1.5111 <	1.7682
	0.01	5.49	112.53	0.033	5.64	43.81	0.9517 <	0.9573
$\beta = 0.2$	0.10	10.48	356.71	0.106	13.40	44.52	1.2319 <	1.3190
	1.00	20.03	1126.75	0.199	[a]33.80	45.21	1.5111 <	1.7043
	0.01	5.49	112.53	0.033	5.70	43.81	0.9517 <	0.9619
$\beta = 0.1$	0.10	10.48	356.71	0.079	[a]14.58	44.52	1.2319 <	1.3607
	1.00	20.03	1126.75	0.144	[a]28.02	45.21	1.5111 <	1.6324
	0.01	9.72	112.53	0.007	16.04	43.81	1.2000 <	1.4165
No shielding	0.10	37.90	356.71	...	[b]...	...	...	...
	1.00	155.27	1126.75	...	[b]...	...	...	...
	0.01	7.63	72.08	–	–	–	–	–
[c]Analytical FRADO	0.10	16.44	227.93	–	–	–	–	–
	1.00	35.42	720.79	–	–	–	–	–

Values of L_{5100} are in ergs/s. Other data are in light-days except $\dot{m}$ and P_{peak} being dimensionless. Patch model and Wall model are specified by their characteristic parameters of α and β, respectively.
[a]Reaching the peak with dust-content sublimated: dust-less failed wind.
[b]It never forms a failed wind neither dust-less nor dusty. All clumps just escape to torus.
[c]This row is just added for the purpose of comparison.

6. BLR SHAPE IN FRADO

In order to find the distribution of material above AD we need to determine the radial extension and height of BLR as follows.

The radial extension of BLR is by definition the range confined within $\mathrm{BLR_{in}}$ to $\mathrm{BLR_{out}}$. Theoretically, $\mathrm{BLR_{in}}$ is the onset of BLR where the dust is instantly sublimated upon departure from AD. The outer radius of BLR, i.e., $\mathrm{BLR_{out}}$, is where the dust survives irradiation by the whole disk even in spherically symmetric approximation of the radiation field. We determine this outer radius by finding the position where the sublimation height for a given radius is equal to the radius itself. Obviously, the shielding effect does not play a role at this large height. In order to find these two radial ends of BLR, for each different initial conditions

we introduce a dense grid of (R, H) pairs ranging as $R:[R_{\mathrm{in}}$ to $R_{\mathrm{out}}]$, and $H:[D(R)$ to $R_{\mathrm{out}}]$. We then numerically compute Q_{abs} at each grid point. The geometrical location where $Q_{\mathrm{abs}} = Q_{\mathrm{emit}}(T_{\mathrm{sub}})$ is a curved line called *sublimation location*, $S(R)$, dividing the region above AD into two parts, above which dust can not survive irradiation. The crossing radius of $S(R)$ and $D(R)$ yields the $\mathrm{BLR_{in}}$; and $\mathrm{BLR_{out}}$ can be found by setting $S(R) = R$.

As for the geometrical height of BLR, we observe the trajectory of clumps being launched from a set of logarithmically spaced initial launching radii (R_{init}) ranging from $\mathrm{BLR_{in}}$ to $\mathrm{BLR_{out}}$. Neglecting the relaxation due to probable encounters between clumps and loss/gain of momentum, we find the maximum heights (H_{peak}) the clump can attain per each initial launching radius within the set. However, in order to stress on the

importance of the opening angle of the BLR clouds distribution, introducing the variable ($P = H_{\text{peak}}/R_{\text{peak}}$) where R_{peak} is the maximum height's corresponding radius, we find the maximum of P, i.e., P_{peak}.

Therefore, the shape of BLR is specified by [$\text{BLR}_{\text{in}} - \text{BLR}_{\text{out}}$], and [$D(R) - H_{\text{peak}}(R)$]. The $R(P_{\text{peak}})$ and $H(P_{\text{peak}})$ corresponding to the unique value of P_{peak} represents the effective location of BLR clouds. This is based on the assumption that the parameter $R(P_{\text{peak}})$ marks the region effectively exposed to the irradiation by the central parts of AD.
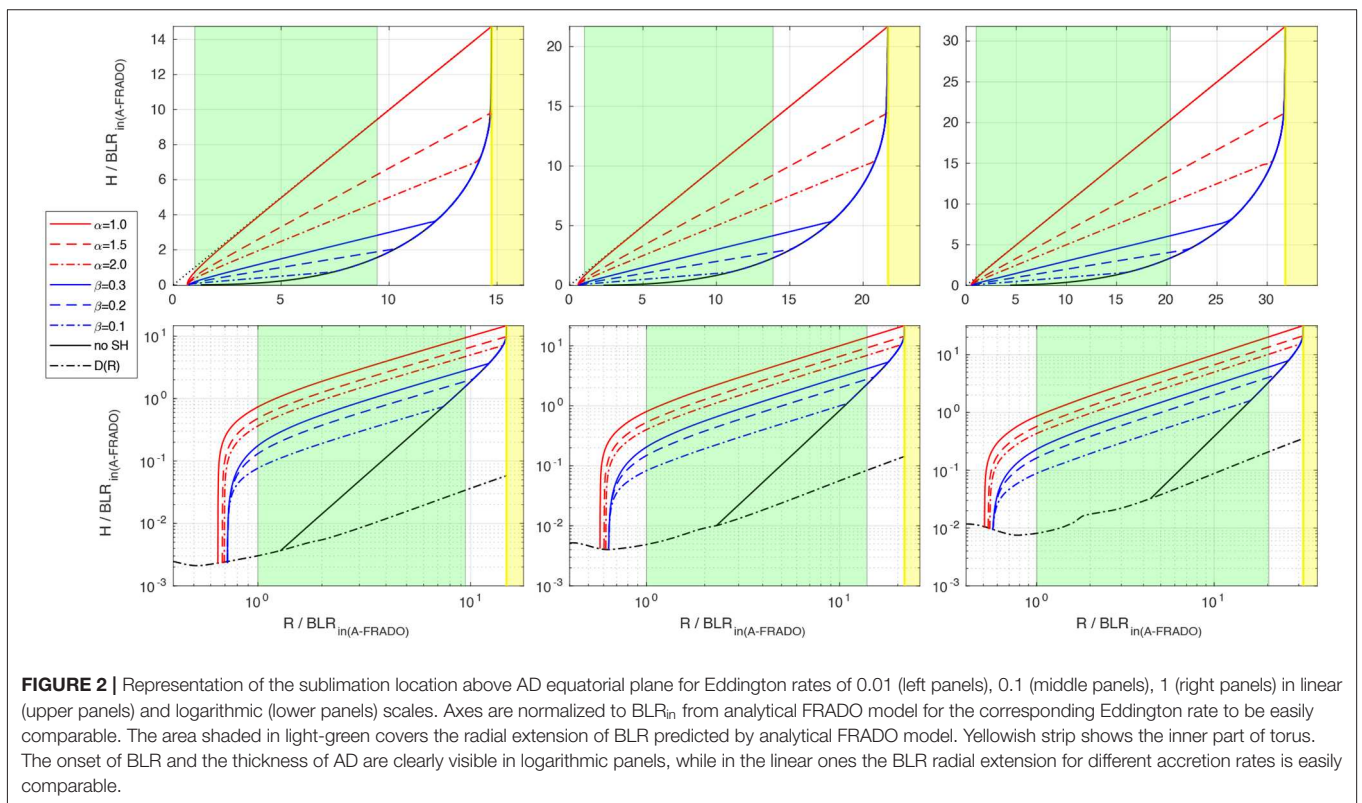
7. RESULTS AND DISCUSSION

Having performed numerical computations for different initial conditions and for both models of shielding, we have obtained values for the size of BLR as collected in **Table 1**. Numerically computed values of the monochromatic luminosity of AD at 5100 Å in erg/s depend only on the accretion rate and blackhole mass; the effects of the shielding and AD self-irradiation are not included (Czerny et al., 2003). Other columns of data listed in **Table 1** are expressed in light-days, except $\dot{m}$ and P_{peak} being dimensionless. The viewing angle for calculating the time-delay τ (equivalent to BLR radius assuming the light speed c propagation of the signals) is set to be $i = 39.2$ (Lawrence and Elvis, 2010).

The sublimation surface, $S(R)$, obtained for all initial conditions and parameters of shielding models in **Table 1** is shown in **Figure 2**. Upper and lower panels show the same plots but in linear and log scale, respectively; in the log plots the onset of BLR and disk thickness is clearly visible while the linear plots

better illustrate the radial extension of BLR for different values of the accretion rate. Obviously, the Patch model provides a stronger shielding than Wall model, and the table is also sorted down based on the strength of shielding. However, it seems that the presented shielding models can behave similarly if certain values of α and β are chosen. For example, based on **Figure 2** one can expect the two shielding models to show very similar patterns for $\alpha = 1/\beta$. The profiles of $S(R)$ in **Figure 2** for all values of α and β show a convergence to the case of no-shielding at BLR_{out}. This is related to the definition of the BLR_{out}, with the requested condition set at large height of the cloud above the disk where the shielding becomes unimportant. In addition the wall model interestingly shows a privilege of unique prediction of BLR_{in} for all values of β that implies the Wall shielding does not work efficiently when the cloud height is small as it happens close to BLR_{in}. However, testing with other values of β is required to firmly determine the model properties.

The two considered shielding models have significantly different geometrical properties, as shown in **Figure 1**. In the Wall model a cloud is exposed to the radiation from a broad range of radii of AD while in the Patch model it is affected only by a local radiation. This may affect the cloud dynamics, and likely will be reflected in the emission-lines shape which is beyond the scope of the current work. However, further studies including the cases with $\alpha = 1/\beta$ are required to highlight the differences between these shielding models properly, and to enable us to make a choice between these two.

As can be seen in **Figure 2**, the ratio of ($\text{BLR}_{\text{out}}/\text{BLR}_{\text{in}}$) increases with Eddington ratio for both analytical and numerical

FIGURE 2 | Representation of the sublimation location above AD equatorial plane for Eddington rates of 0.01 (left panels), 0.1 (middle panels), 1 (right panels) in linear (upper panels) and logarithmic (lower panels) scales. Axes are normalized to BLR_{in} from analytical FRADO model for the corresponding Eddington rate to be easily comparable. The area shaded in light-green covers the radial extension of BLR predicted by analytical FRADO model. Yellowish strip shows the inner part of torus. The onset of BLR and the thickness of AD are clearly visible in logarithmic panels, while in the linear ones the BLR radial extension for different accretion rates is easily comparable.
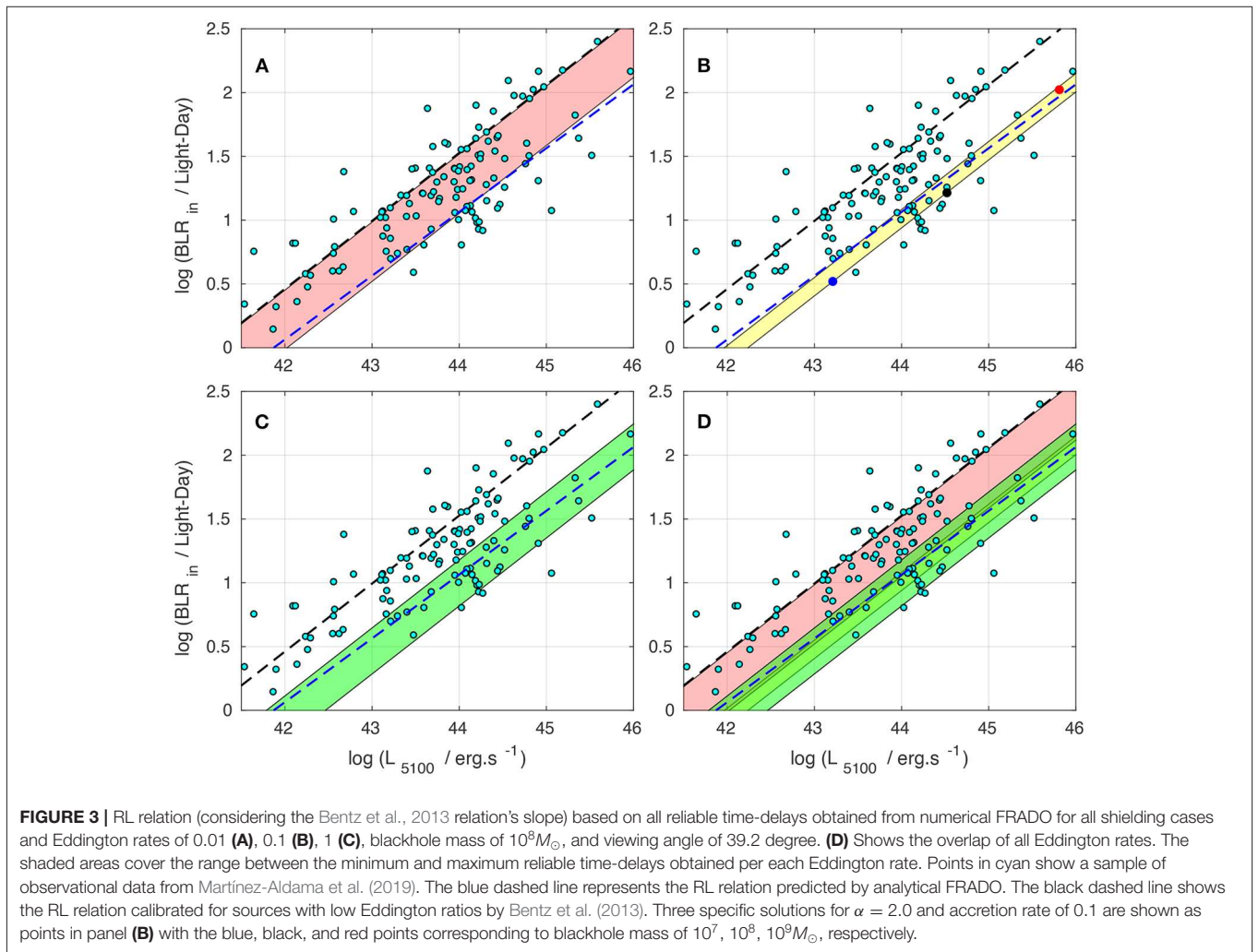
FRADO. However, the BLR size in numerical models with shielding is radially more extended than that of analytical ones which implies longer time-delays from the entire BLR.

According to **Table 1**, in case of no-shielding for accretion rates of 0.1 and 1, all launched clumps only escape to the torus and do not form a failed wind. These cases were omitted due to being out of interest in the current preliminary study. There are cases for accretion rates of 0.01 and 0.1 in Patch model in **Table 1** with $R_{peak} \sim BLR_{in}$ yielding time-delays for BLR_{in}, $\log(\tau_{in})$, being larger than that of R_{peak}, $\log(\tau_{peak})$. They imply the presence of a very sharp cut-off in dynamics of material past the BLR_{in}. These cases can not be considered as reliable. It is while for the accretion rate of 1, all shielding cases give a larger value for $\log(\tau_{peak})$. This means that for high accretion rate the presence of shielding is necessary. In other words, the higher the accretion rate is, the stronger shielding is required. A denser set of bins in the range of values of α and β in future studies will be more indicative.

As explained in section 6, since larger values of opening angle are of our interest, we chose the model showing the maximum P_{peak} among the obtained values for all shielding models per

the arbitrary accretion rate of 0.1 to perform a test with other blackhole masses. The maximum P_{peak} corresponds to $\alpha = 2.0$, however it does not necessarily mean the preference of Patch model over Wall model, or appropriateness of this α. We then repeated the simulation for this model for two other blackhole masses of 10^7, and $10^9 M_\odot$. Interestingly, while the Patch model with the adopted values of α, was too strong as mentioned above to be considered as reliable for accretion rates of 0.01 and 0.1, the consistent time-delay obtained for the blackhole mass of $10^9 M_\odot$ and accretion rate of 0.1 with $\alpha = 2.0$ indicates the dependence of shielding on blackhole mass as well; i.e., the higher the blackhole mass is, the stronger shielding is required.

As for plotting the RL relation, since we only have the data for the blackhole mass of $10^8 M_\odot$ (except the case of $\alpha = 2.0$), we take use of the slope of Bentz et al. (2013) relation. The RL relation based on reliable results for all adopted values of accretion rates are then shown in **Figure 3**, and compared to observational data and analytical FRADO model (see also Naddaf et al., 2019 for RL relation based on τ_{in}). Time-delays are computed assuming the effective reflection of reprocessed radiation of continuum happens for the clouds located in farther side of AD, as in Czerny

FIGURE 3 | RL relation (considering the Bentz et al., 2013 relation's slope) based on all reliable time-delays obtained from numerical FRADO for all shielding cases and Eddington rates of 0.01 **(A)**, 0.1 **(B)**, 1 **(C)**, blackhole mass of $10^8 M_\odot$, and viewing angle of 39.2 degree. **(D)** Shows the overlap of all Eddington rates. The shaded areas cover the range between the minimum and maximum reliable time-delays obtained per each Eddington rate. Points in cyan show a sample of observational data from Martínez-Aldama et al. (2019). The blue dashed line represents the RL relation predicted by analytical FRADO. The black dashed line shows the RL relation calibrated for sources with low Eddington ratios by Bentz et al. (2013). Three specific solutions for $\alpha = 2.0$ and accretion rate of 0.1 are shown as points in panel **(B)** with the blue, black, and red points corresponding to blackhole mass of 10^7, 10^8, $10^9 M_\odot$, respectively.

and Hryniewicz (2011), while the clouds in the closer side are almost self-obscured. As the whole material in the range between the onset of BLR and the maximum height can be irradiated by the continuum, the area between minimum/maximum time-delays corresponding to the minimum BLR_{in}/maximum $R(P_{peak})$ obtained out of all reliable data in **Table 1** for a given accretion rate are shown as shaded patterns in **Figure 3**. While the analytical FRADO only gives a single line, the realistic 3-D approach covers almost the whole sample of observational data. The points corresponding to three blackhole masses for the test case of $\alpha = 2.0$ with accretion rate of 0.1 are also depicted in **Figure 3B** which are located within the yellow strip, and follow the RL trend apparently. However, testing with a wider-denser set of blackhole masses is also required in future studies to provide us with a full insight into the models.

8. CONCLUSIONS

In this preliminary work we theoretically studied the dynamics of matter in the BLR based on a realistic 3-D approach to FRADO model. We introduced two geometrical configurations for shielding effect, and based on the dynamics, we tried to predict the BLR size (radial extension and geometrical height) and its dependence on different Eddington ratios [and blackhole mass] to compare with observational data. The main findings can be concluded as below

- FRADO model can account for the range of measured time-delays of Hβ line in AGNs. The model is expected to work for all LILs like Hbeta and Mg-II (Czerny et al., 2019; Zajaček et al., 2019) but not for HILs which form closer in and come from line-driven wind part.
- The shielding must be included in the model, although low Eddington sources do not require it.

- The role of shielding must increase with the Eddington ratio of the source, as well as with blackhole mass.
- BLR size is predicted to be radially more extended compared to analytical FRADO which implies longer time-delays from the entire BLR.
- Future modeling of the emission line shapes based on the cloud dynamics will bring further constraints to the shielding geometry.

DATA AVAILABILITY STATEMENT

All datasets generated for this study are included in the article/supplementary material.

AUTHOR CONTRIBUTIONS

All authors listed have made a substantial, direct and intellectual contribution to the work, and approved it for publication.

REFERENCES

Baskin, A., and Laor, A. (2018). Dust inflated accretion disc as the origin of the broad line region in active galactic nuclei. *Mon. Not. R. Astron. Soc.* 474, 1970–1994. doi: 10.1093/mnras/stx2850

Begelman, M. C., McKee, C. F., and Shields, G. A. (1983). Compton heated winds and coronae above accretion disks. I. Dynamics. *Astrophys. J.* 271, 70–88. doi: 10.1086/161178

Bentz, M. C., Denney, K. D., Grier, C. J., Barth, A. J., Peterson, B. M., Vestergaard, M., et al. (2013). The low-luminosity end of the radius-luminosity relationship for active galactic nuclei. *Astrophys. J.* 767:149. doi: 10.1088/0004-637X/767/2/149

Bentz, M. C., Walsh, J. L., Barth, A. J., Baliber, N., Bennert, V. N., Canalizo, G., et al. (2009). The lick AGN monitoring project: broad-line region radii and black hole masses from reverberation mapping of Hβ. *Astrophys. J.* 705, 199–217. doi: 10.1088/0004-637X/705/1/199

Blandford, R. D., and Begelman, M. C. (1999). On the fate of gas accreting at a low rate on to a black hole. *Mon. Not. R. Astron. Soc.* 303, L1–L5. doi: 10.1046/j.1365-8711.1999.02358.x

Blandford, R. D., and Payne, D. G. (1982). Hydromagnetic flows from accretion disks and the production of radio jets. *Mon. Not. R. Astron. Soc.* 199, 883–903. doi: 10.1093/mnras/199.4.883

Collin, S., and Zahn, J.-P. (1999). Star formation and evolution in accretion disks around massive black holes. *Astron. Astrophys.* 344, 433–449. doi: 10.1007/978-94-011-4213-7_107

Collin, S., and Zahn, J. P. (2008). Star formation in accretion discs: from the Galactic center to active galactic nuclei. *Astron. Astrophys.* 477, 419–435. doi: 10.1051/0004-6361:20078191

Czerny, B., Du, P., Wang, J.-M., and Karas, V. (2016). A test of the formation mechanism of the broad line region in active galactic nuclei. *Astrophys. J.* 832:15. doi: 10.3847/0004-637X/832/1/15

Czerny, B., and Hryniewicz, K. (2011). The origin of the broad line region in active galactic nuclei. *Astron. Astrophys.* 525:L8. doi: 10.1051/0004-6361/201016025

Czerny, B., Li, J., Loska, Z., and Szczerba, R. (2004). Extinction due to amorphous carbon grains in red quasars from the Sloan Digital Sky Survey. *Mon. Not. R. Astron. Soc.* 348, L54–L57. doi: 10.1111/j.1365-2966.2004.07590.x

Czerny, B., Li, Y.-R., Hryniewicz, K., Panda, S., Wildy, C., Sniegowska, M., et al. (2017). Failed radiatively accelerated dusty outflow model of the broad line region in active galactic nuclei. I. Analytical solution. *Astrophys. J.* 846:154. doi: 10.3847/1538-4357/aa8810

Czerny, B., Modzelewska, J., Petrogalli, F., Pych, W., Adhikari, T. P., Życki, P. T., et al. (2015). The dust origin of the broad line region and the model consequences for AGN unification scheme. *Adv. Space Res.* 55, 1806–1815. doi: 10.1016/j.asr.2015.01.004

Czerny, B., Nikołajuk, M., Różańska, A., Dumont, A. M., Loska, Z., and Zycki, P. T. (2003). Universal spectral shape of high accretion rate AGN. *Astron. Astrophys.* 412, 317–329. doi: 10.1051/0004-6361:20031441

Czerny, B., Olejak, A., Rałowski, M., Kozłowski, S., Loli Martinez Aldama, M., Zajacek, M., et al. (2019). Time delay measurement of Mg II Line in CTS C30.10 with SALT. *Astrophys. J.* 880:46. doi: 10.3847/1538-4357/ab2913

Czerny, M., and King, A. R. (1989). Accretion disc winds and coronae. *Mon. Not. R. Astron. Soc.* 236, 843–850. doi: 10.1093/mnras/236.4.843

Dong, X., Wang, T., Wang, J., Yuan, W., Zhou, H., Dai, H., et al. (2008). Broad-line Balmer decrements in blue active galactic nuclei. *Mon. Not. R. Astron. Soc.* 383, 581–592. doi: 10.1111/j.1365-2966.2007.12560.x

Du, P., Hu, C., Lu, K.-X., Huang, Y.-K., Cheng, C., Qiu, J., et al. (2015). Supermassive black holes with high accretion rates in active galactic nuclei. IV. Hβ time lags and implications for super-Eddington accretion. *Astrophys. J.* 806:22. doi: 10.1088/0004-637X/806/1/22

Du, P., Lu, K.-X., Zhang, Z.-X., Huang, Y.-K., Wang, K., Hu, C., et al. (2016). Supermassive black holes with high accretion rates in active galactic nuclei. V. A new size-luminosity scaling relation for the broad-line region. *Astrophys. J.* 825:126. doi: 10.3847/0004-637X/825/2/126

Du, P., Zhang, Z.-X., Wang, K., Huang, Y.-K., Zhang, Y., Lu, K.-X., et al. (2018). Supermassive black holes with high accretion rates in active galactic nuclei. IX. 10 new observations of reverberation mapping and shortened Hβ lags. *Astrophys. J.* 856:6. doi: 10.3847/1538-4357/aaae6b

Elitzur, M., Ho, L. C., and Trump, J. R. (2014). Evolution of broad-line emission from active galactic nuclei. *Mon. Not. R. Astron. Soc.* 438, 3340–3351. doi: 10.1093/mnras/stt2445

Emmering, R. T., Blandford, R. D., and Shlosman, I. (1992). Magnetic acceleration of broad emission-line clouds in active galactic nuclei. *Astrophys. J.* 385:460. doi: 10.1086/170955

Grier, C. J., Trump, J. R., Shen, Y., Horne, K., Kinemuchi, K., McGreer, I. D., et al. (2017). The Sloan Digital Sky Survey reverberation mapping project: Hα and Hβ reverberation measurements from first-year spectroscopy and photometry. *Astrophys. J.* 851:21. doi: 10.3847/1538-4357/aa98dc

Haas, M., Chini, R., Ramolla, M., Pozo Nuñez, F., Westhues, C., Watermann, R., et al. (2011). Photometric AGN reverberation mapping–an efficient tool for BLR sizes, black hole masses, and host-subtracted AGN luminosities. *Astron. Astrophys.* 535:A73. doi: 10.1051/0004-6361/201117325

Hu, C., Wang, J.-M., Ho, L. C., Chen, Y.-M., Zhang, H.-T., Bian, W.-H., et al. (2008). A systematic analysis of Fe II emission in quasars: evidence for inflow to the central black hole. *Astrophys. J.* 687, 78–96. doi: 10.1086/591838

Kaspi, S., Smith, P. S., Netzer, H., Maoz, D., Jannuzi, B. T., and Giveon, U. (2000). Reverberation measurements for 17 quasars and the size-mass-luminosity relations in active galactic nuclei. *Astrophys. J.* 533, 631–649. doi: 10.1086/308704

Lawrence, A., and Elvis, M. (2010). Misaligned disks as obscurers in active galaxies. *Astrophys. J.* 714, 561–570. doi: 10.1088/0004-637X/714/1/561

Martínez-Aldama, M. L., Czerny, B., Kawka, D., Karas, V., Panda, S., Zajaček, M., et al. (2019). Can reverberation-measured quasars be used for cosmology? *Astrophys. J.* 883:170. doi: 10.3847/1538-4357/ab3728

Mathis, J. S., Rumpl, W., and Nordsieck, K. H. (1977). The size distribution of interstellar grains. *Astrophys. J.* 217, 425–433. doi: 10.1086/155591

Murray, N., Chiang, J., Grossman, S. A., and Voit, G. M. (1995). Accretion disk winds from active galactic nuclei. *Astrophys. J.* 451:498. doi: 10.1086/176238

Naddaf, M.-H., Czerny, B., and Szczerba, R. (2019). R-L relation in realistic FRADO model. *arXiv* 1912.00278.

Netzer, H. (2015). Revisiting the unified model of active galactic nuclei. *Astron. Astrophys.* 53, 365–408. doi: 10.1146/annurev-astro-082214-122302

Netzer, H., Lutz, D., Schweitzer, M., Contursi, A., Sturm, E., Tacconi, L. J., et al. (2007). Spitzer quasar and ULIRG evolution study (QUEST). II. The spectral energy distributions of palomar-green quasars. *Astrophys. J.* 666, 806–816. doi: 10.1086/520716

Panda, S., Czerny, B., Adhikari, T. P., Hryniewicz, K., Wildy, C., Kuraszkiewicz, J., et al. (2018). Modeling of the quasar main sequence in the optical plane. *Astrophys. J.* 866:115. doi: 10.3847/1538-4357/aae209

Panda, S., Martínez-Aldama, M. L., and Zajaček, M. (2019). Current and future applications of reverberation-mapped quasars in cosmology. *Front. Astron. Space Sci.* 6:75. doi: 10.3389/fspas.2019.00075

Peterson, B. M., Ferrarese, L., Gilbert, K. M., Kaspi, S., Malkan, M. A., Maoz, D., et al. (2004). Central masses and broad-line region sizes of active galactic nuclei. II. A homogeneous analysis of a large reverberation-mapping database. *Astrophys. J.* 613, 682–699. doi: 10.1086/423269

Peterson, B. M., Wanders, I., Horne, K., Collier, S., Alexander, T., Kaspi, S., et al. (1998). On uncertainties in cross-correlation lags and the reality of wavelength-dependent continuum lags in active galactic nuclei. *Publ. Astron. Soc. Pac.* 110, 660–670. doi: 10.1086/316177

Proga, D. (2007). Dynamics of accretion flows irradiated by a quasar. *Astrophys. J.* 661, 693–702. doi: 10.1086/515389

Rakshit, S., Woo, J.-H., Gallo, E., Hodges-Kluck, E., Shin, J., Jeon, Y., et al. (2019). The Seoul National University AGN monitoring project. II. BLR size and black hole mass of two AGNs. *Astrophys. J.* 886:93. doi: 10.3847/1538-4357/ab49fd

Risaliti, G., and Elvis, M. (2010). A non-hydrodynamical model for acceleration of line-driven winds in active galactic nuclei. *Astron. Astrophys.* 516:A89. doi: 10.1051/0004-6361/200912579

Różańska, A., Czerny, B., Życki, P. T., and Pojmański, G. (1999). Vertical structure of accretion discs with hot coronae in active galactic nuclei. *Mon. Not. R. Astron. Soc.* 305, 481–491. doi: 10.1046/j.1365-8711.1999.02425.x

Röllig, M., Szczerba, R., Ossenkopf, V., and Glück, C. (2013). Full SED fitting with the KOSMA-τ PDR code. I. Dust modelling. *Astron. Astrophys.* 549:A85. doi: 10.1051/0004-6361/201118190

Shakura, N. I., and Sunyaev, R. A. (1973). Black holes in binary systems. Observational appearance. *Astron. Astrophys.* 500, 33–51. doi: 10.1007/978-94-010-2585-0_13

Shangguan, J., Ho, L. C., and Xie, Y. (2018). On the gas content and efficiency of AGN feedback in low-redshift quasars. *Astrophys. J.* 854:158. doi: 10.3847/1538-4357/aaa9be

Shen, Y., Richards, G. T., Strauss, M. A., Hall, P. B., Schneider, D. P., Snedden, S., et al. (2011). A catalog of quasar properties from Sloan Digital Sky survey data release 7. *Astrophys. J. Suppl.* 194:45. doi: 10.1088/0067-0049/194/2/45

Szczerba, R., Omont, A., Volk, K., Cox, P., and Kwok, S. (1997). IRAS 22272+5435– a source with 30 and 21 μm features. *Astron. Astrophys.* 317, 859–870.

Wang, J.-M., Du, P., Baldwin, J. A., Ge, J.-Q., Hu, C., and Ferland, G. J. (2012). Star formation in self-gravitating disks in active galactic nuclei. II. Episodic formation of broad-line regions. *Astrophys. J.* 746:137. doi: 10.1088/0004-637X/746/2/137

Wang, J.-M., Du, P., Brotherton, M. S., Hu, C., Songsheng, Y.-Y., Li, Y.-R., et al. (2017). Tidally disrupted dusty clumps as the origin of broad emission lines in active galactic nuclei. *Nat. Astron.* 1, 775–783. doi: 10.1038/s41550-017-0264-4

Wang, J.-M., Ge, J.-Q., Hu, C., Baldwin, J. A., Li, Y.-R., Ferland, G. J., et al. (2011). Star formation in self-gravitating disks in active galactic nuclei. I. Metallicity gradients in broad-line regions. *Astrophys. J.* 739:3. doi: 10.1088/0004-637X/739/1/3

Watson, D., Denney, K. D., Vestergaard, M., and Davis, T. M. (2011). A new cosmological distance measure using active galactic nuclei. *Astrophys. J.* 740:L49. doi: 10.1088/2041-8205/740/2/L49

Witt, H. J., Czerny, B., and Zycki, P. T. (1997). Accretion discs with accreting coronae in active galactic nuclei–II. The nuclear wind. *Mon. Not. R. Astron. Soc.* 286, 848–864. doi: 10.1093/mnras/286.4.848

Zajaček, M., Czerny, B., Martínez-Aldama, M. L., and Karas, V. (2019). Reverberation mapping of distant quasars: time lag determination using different methods. *Astron. Nachr.* 340, 577–585. doi: 10.1002/asna.201913659

Chapter 5

Paper III: Radiation pressure on dust explaining the low ionized broad emission lines in AGNs

Astronomy & Astrophysics

Radiation pressure on dust explaining the low ionized broad emission lines in active galactic nuclei

Dust as an important driver of line shape

M. H. Naddaf[1,2] and B. Czerny[1]

[1] Center for Theoretical Physics, Polish Academy of Sciences, Lotników 32/46, 02-668 Warsaw, Poland
e-mail: naddaf@cft.edu.pl
[2] Nicolaus Copernicus Astronomical Center, Polish Academy of Sciences, Bartycka 18, 00-716 Warsaw, Poland

ABSTRACT

Context. Broad emission lines are the most characteristic features in the spectra of galaxies with an active galactic nucleus (AGN). They mostly show either single-peaked or double-peaked profiles and originate from a complex dynamics of the likely discrete clouds moving in a spatially extended region known as the broad line region (BLR).
Aims. In this paper, we present a large grid of results, which is used to test the model based on calculations of the spectral line generic profiles.
Methods. We followed a non-hydrodynamical single-cloud approach to BLR dynamics based on a radiatively dust-driven model. We previously showed in detail that the 2.5D version of the model could provide us with the 3D geometry of the BLR.
Results. We show that the shape of profiles not only depends on the accretion rate of the source, the black hole mass, and the viewing angle, but it is most significantly affected by the adopted dust-to-gas mass ratio regulating the strength of the radiation pressure. We also show that the model can aptly explain the low ionized broad emission lines of the mean spectrum of quasars, such as MgII and Hβ.
Conclusions. The radiatively dust-driving mechanism can appropriately account for the low-ionized part of BLR of AGNs.

Key words. accretion, accretion disks – radiation: dynamics – line: profiles – radiative transfer – galaxies: active – quasars: emission lines

1. Introduction

The broad line region (BLR) in active galaxies is a turbulent and spatially extended region (Wandel et al. 1999; Kaspi et al. 2000; Netzer 2020) that has not yet been fully resolved, except for a few cases of magnified BLR due to gravitational lensing (Sluse et al. 2012; Guerras et al. 2013) as well as the VLR GRAVITY observations in the IR (GRAVITY Collaboration 2018, 2020a, 2021). Hence, studies of broad emission lines stemming from this region have been based on the analysis of the spectra and their time dependence (Boroson & Green 1992; Lawrence et al. 1997; Sulentic et al. 2000; Reeves & Turner 2000; Gaskell 2009; Le & Woo 2019; Raimundo et al. 2020). However, the broad emission lines (BELs) from a BLR are a unique probe that can be used to improve our understanding of the physics of AGNs and, eventually, they can help to measure the mass of the central supermassive black hole. These emission lines are divided into two categories of high ionization lines (HIL) and low ionization lines (LIL) (Collin-Souffrin et al. 1988; Netzer 2013), and they are frequently observed in the form of single-peaked or double-peaked profiles (Osterbrock 1977, 1981; Gezari et al. 2007; Shen et al. 2011; Negrete et al. 2018; Zhang et al. 2019; Lu et al. 2021; Li et al. 2021). The shape of BELs depends on the distribution and dynamics of material within the BLR. There have been two mainstream studies that have been ongoing for years on the theoretical side to recover the observed shape of emission lines: one based on proposing

theoretically motivated mechanisms for the formation of BLR and the other one on the basis of assuming a certain distribution of material in a BLR (i.e., parametric models).

The BLR in parametric models can have different geometries of interest depending on the purpose, for example a ring, a disk, a shell, or a cone filled with clouds in which the density of clouds is assumed to follow a certain function (Netzer & Laor 1993; Ward et al. 2014; Adhikari et al. 2016, 2018; GRAVITY Collaboration 2018). As the name of these models implies, the distribution, density, and other physical properties of clouds in the BLR are parameterized in order to optimize the shape of emission lines and time-delays map (Pancoast et al. 2011, 2014; Li et al. 2013). In order to fit the data, they either infer the transfer function (Blandford & McKee 1982; Horne et al. 1991; Krolik & Done 1995; Li et al. 2016) or provide a quantitative constraints on the dynamics and geometry of BLR (Li et al. 2013; Pancoast et al. 2014). Although these models are useful, providing insights into the connection between the BLR geometry and line shape, while fitting the observational data, they are not intended to provide the theoretically motivated scenario behind the picture.

On the other hand, we previously showed that the failed radiatively accelerated dusty outflow (FRADO) model (Czerny & Hryniewicz 2011), among all other already proposed theoretical mechanisms, may effectively account for the formation and the dynamics of the LIL part of BLR such as Hβ and MgII (Naddaf et al. 2021). A preliminary test of the model
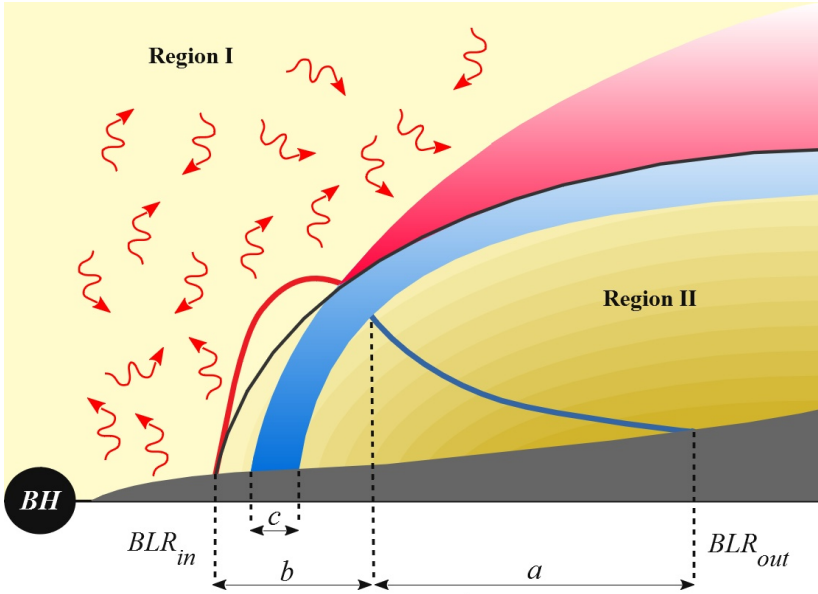
Fig. 1. Schematic illustration of BLR shape and its components in FRADO. The components of BLR are represented as (*a*) an outer tail consisting of dusty failed winds (simple up-and-down motions), (*b*) an inner region with slightly-to-broadly elongated elliptical orbits, and (*c*) a funnel-shaped outflow stream of clouds. The red and blue solid lines show the peak height of the trajectories of dustless and dusty clouds, respectively. The BLR_{in} and BLR_{out} set the two ends of a radial region of the accretion disk within which the material can be lifted due to disk radiation pressure. The black solid line represents the sublimation location. Region I marks the hot region above the sublimation location where dust cannot survive; the central disk UV radiation reaches the clouds via scattering by the hot gas in this region. Region II underneath of the sublimation location and cold enough for dust survival is obscured by the outflow stream; it prevents the BLR material from receiving the scattered ionizing radiation.

also showed that it reproduces the reverberation-known location of the LIL BLR (Peterson et al. 2004; Bentz et al. 2009, 2013) without including any arbitrary parameter; it can also successfully explain the observed dispersion in Hβ radius–luminosity (RL) relation based on the accretion rate (Naddaf et al. 2020). On the other hand, the high ionization lines such as CIV and HeII are located much closer to the center (e.g., Wandel et al. 1999; Grier et al. 2013) where dust cannot form and dust-driving mechanism is not available; thus, they are most likely to be related to line-driven winds (Proga et al. 2000; Dyda & Proga 2018) or thermally driven winds (e.g., Ganguly et al. 2021).

In this paper, we aim to test the model by calculating the line profiles. We begin by introducing a relatively large grid table of results for a range of black hole masses, accretion rates, and dust-to-gas mass ratio of clumps. We briefly explain the physics of BLR dynamics in 2.5D FRADO in Sect. 2. The numerical setup is introduced in Sect. 3. The physics of LIL BLR emission lines and the method behind the line profile calculation is addressed in the Sect. 4. We then present our results in Sect. 5, followed by a discussion in Sect. 6.

2. BLR Dynamics in 2.5D FRADO

The 2.5D FRADO model (see Naddaf et al. 2021, for full details) is a nonhydrodynamical single-cloud approach to LIL BLR dynamics. It is the enhanced version of the basic 1D model of Czerny & Hryniewicz (2011), a model based on the presence of dust in the atmosphere of an accretion disk at large radii, where it is cold enough (Rees et al. 1969; Dong et al. 2008). The FRADO model works on the basis of radiatively dust-driving mechanism, so the disk radiation pressure acting on the initially dusty material (clumps) at the surface layers of the accretion disk leads to a (mostly failed) outflow from the accretion disk. We should stress here that only dust processes do the job in this model, and the line-driving or electron scattering forces are negligible at these radii – rendering this model appropriate for studies of the LIL BLR. General relativistic effect are also negligible at these large radii, so they were neglected.

In the 2.5D FRADO, the model is enhanced with the realistic description of the dust opacities interacting with the radiation field. Geometrical configurations as proxies for the

shielding effect are necessary for launching an efficient outflow, as suggested previously by numerous authors (Shlosman et al. 1985; Voit 1992; Murray et al. 1995; Proga & Kallman 2004; Risaliti & Elvis 2010; Mizumoto et al. 2019). These are incorporated into the model in order to protect the dusty clumps from the intense central disk radiation, avoiding, hence, an overly rapid sublimation of the dust content of the clouds. Most AGNs do not show the double-peaked line profiles expected from the illuminated disk surface, so in order to produce single-peaked line profiles, the material has to reach a high vertical velocity under the continuous radiative force from below. The timescale of the process depend very much on the black hole mass, as the strong radiative force must act for a period being a noticeable fraction of the local Keplerian period. A similar requirement is necessary for line-driving winds responsible for the HIL part of the BLR, where shielding is needed in order to prevent an overionization of the medium and loss of the driving power. Clumps at initially circular local Keplerian orbits are launched (with a zero vertical velocity) from the disk surface by the disk radiation pressure and move under the radiative force from the accretion disk and gravitational field of the central black hole. The radial dependent height of the disk (disk surface) for the grid of initial conditions in our model was calculated using a separate code (Różańska et al. 1999; Czerny et al. 2016). Upon attaining high altitudes, depending on the launching radius, clumps may lose their dust content due to strong radiation from inner radii of the disk and continue their motion in the form of a free-fall in the black hole gravitational field; otherwise, they would remain dusty during the motion. Moreover, depending on the launching location clumps may escape into infinity or return to the disk surface, however, they cannot cross the disk.

The whole pattern of the trajectories of clouds depends on the initial physical parameters, and the geometry of LIL BLR in our model was determined by the kinematics of the clouds. As previously studied (Naddaf et al. 2021), it does not resemble the simple (or complicated) shapes in parametric models. We showed that the overall picture of LIL BLR can be either very complex or just as simple as an up-and-down motion, depending on the accretion rate. The general pattern of motion in FRADO consists of three components, as indicated in Fig. 1: (a) an outer tail consisting of dusty failed winds (simple up-and-down motions) that resembles the static puffed-up irradiated

disk model of Baskin & Laor (2018) – this component is always present regardless of the adopted values of the initial parameters and for the very low values the full BLR is in this form; (b) an inner region with slightly to largely elongated elliptical orbits; and (c) a funnel-shaped stream of escaping clouds similar to empirical picture of AGNs (Elvis 2000). The last two components may develop (or not) depending on the initial parameters, namely, the black hole mass, accretion rate, and metallicity. As previously discussed but not calculated, it can be expected that the first component may give rise to a double-peaked (disky shape) line profile consistent with observational data for low Eddington sources, however, single-peaked profiles are likely expected from the two latter components (see Naddaf et al. 2021, for more details).

In the previous work, aimed at testing the model, the black hole mass was fixed to $10^8 M_\odot$ and we studied the cases with dust-to-gas ratio equivalent to solar metalicity for a range of accretion rates. We did not investigate how changing the black hole mass and other parameters can affect the overall picture. In this paper, we present a large table of results for a relatively wide range of physical parameters of AGNs (introduced in Sect. 3) which we use to test the 2.5D FRADO model, based on calculations of line shapes.

3. Numerical setup

In order to have a relatively broad and comprehensive table of results, the following numerical setup was considered. The main initial physical parameters in this setup, namely, the black hole mass, M_{BH}, dimensionless accretion rate, $\dot{m}$, and dust-to-gas mass ratio Ψ are:

– M_{BH} of $10^6, 10^7, 10^8$, and $10^9 M_\odot$.
– $\dot{m}$ of $0.01, 0.1$ and 1 in Eddington units defined as:

$$\dot{M}_{edd} = \frac{4\pi G M_{BH} m_p}{\mu \sigma_T c}, \tag{1}$$

where μ is the accretion efficiency fixed to 0.1. For a reference, the Eddington value for the black hole mass of $10^6 M_\odot$ is taken as:

$$\dot{M}_{edd(6)} = 1.399 \times 10^{24} \, [\text{g s}^{-1}]. \tag{2}$$

– Ψ of 0.005 and 0.025, equivalent to one and five times the solar metalicity, respectively.

The first two almost cover the observed range of black hole mass and Eddington rate of AGNs (Shen et al. 2011; Panda et al. 2018). On the other hand, many studies indicate that the metallicity in AGNs can super-solar (see e.g., Hamann & Ferland 1992; Artymowicz et al. 1993; Artymowicz 1993; Matteucci & Padovani 1993; Ferland et al. 1996; Hamann 1997; Warner et al. 2002; Dietrich et al. 2003; Castro et al. 2017; Xu et al. 2018; Shangguan et al. 2018; Šniegowska et al. 2021), even though an observational study by Esparza-Arredondo et al. (2021) has shown that the value of the dust-to-gas ratio for the torus can range from 0.01 to 1 times that of the interstellar medium. Studies also show that there is no correlation between the metallicity in AGNs with either the Eddington rate, black hole mass, or total luminosity (see Du et al. 2014, and references therein). Therefore, in this paper, in addition to the solar value adopted in our previous work, we present our results for five times the solar metallicity, as in Baskin & Laor (2018).

The sublimation temperature of dust is kept at 1500 K (Baskin & Laor 2018) as in Naddaf et al. (2021). The values of

wavelength-dependent dust opacities (as before) are based on the prescriptions of Röllig et al. (2013) and Szczerba et al. (1997) for the classical Mathis–Rumpl–Nordsieck (MRN) dust model (Mathis et al. 1977) consisting of silicate and graphite grains. The standard extended optically thick, geometrically thin disk model of Shakura & Sunyaev (1973) is the source of radiation in our model. As our two previously proposed geometrical configurations for the shielding effect did not show any significant difference, we arbitrarily choose the α-patch model, with an α parameter equal to 3 (as before) for the purposes of consistency (Naddaf et al. 2021).

4. LIL BLR line profiles

The observed line profiles reflect the distribution of the BLR material, velocity field, and local emissivity. In our model, the velocity field is determined, but we still need to provide the amount of material along the trajectories and the efficiency of the line formation at each location. In particular, this last aspect is not simple despite many years of study. Reverberation mapping shows that the lines do respond to the irradiation by the central source, and the formation of LIL lines such as Hβ, MgII, or FeII requires incident hard continuum (far UV). However, the response of the medium to irradiation is complex. The dust radiation pressure alleviating the clouds does not guarantee any line formation in a cloud as long as the cloud does not receive some UV radiation from the central parts. Particularly in the case of LIL lines, the density of the medium is high and, in principle, the collisional excitation, self-shielding, dust content, complex coupling between the continuum and line transfer, and local turbulence should be considered (see e.g., Baldwin 1997; Ilić et al. 2012). Such a comprehensive 3D model is still beyond the scope of the current work.

4.1. Calculation of line profile

Given a distribution of position and velocity of clouds within BLR, we can find the overall shape of line emission by the clouds. On the one hand, the emission wavelengths of clouds are shifted from the rest-frame wavelength depending on their velocity component toward or against the observer due to the relativistic Doppler shift. On the other hand, the position of clouds can provide some weight to the amount of central flux they receive, as well as to their transparency to the observer, namely, the amount of flux re-emitted by each cloud in the form of LIL. The emission from the clouds, depending on their location, might be subject to gravitational redshift as well.

The Doppler shift and gravitational redshift together cause the emitted wavelength λ_{emit} of the cloud line emission to shift toward the observed wavelength λ_{obs}. However, as the radial distance of the onset of LIL BLR from the center is large, of order of several 10^2 (in case of the largest black hole mass and the smallest accretion rate) to a few 10^4 r_g (in case of the smallest black hole mass and the largest accretion rate), the gravitational redshift is negligible; hence, we only address the Doppler shift here.

In the current paper, we assume a uniform constant cloud density within the entire LIL BLR as the line fitting in LIL BLR (e.g., Adhikari et al. 2016; Panda et al. 2018) supports the universal value for the cloud density. It can be further enhanced in the future by assuming a certain density function for the hot surrounding medium, thus, the pressure balance can yield the density of clouds as a function of the cloud position (Różańska et al. 2006; Baskin & Laor 2018). We do not address

the radiative transfer in our non-hydrodynamic simplified model either.

The most important effect here is that of shielding. In the dynamics, the shielding effect is included which leads to efficient acceleration of the cloud. However, fully shielded clouds do not produce emission lines. When we carry out a posteriori check of clouds that are ultimately well exposed to the central flux, we see that only a small fraction of levitated dust-sublimated clouds in the inner LIL BLR would be directly affected by the central UV radiation. An example of a cloud directly illuminated by the central flux is given and discussed in the section results.

We thus assume that the illumination must be predominantly indirect. This is in agreement with other arguments stating that LIL part of the BLR does not see the full emission from the disk central parts. First argument comes from shorter than expected time delays in higher Eddington ratio sources and it introduces the geometrical concept of two BLR regions – one is closer to the symmetry axis and exposed to irradiation, while the second one is hiding behind the geometrically thick accretion disk (Wang et al. 2014). The other argument comes directly from estimates of the line equivalent width which imply that only a small fraction, namely, on the order of one percent of the nuclear emission, is reprocessed to give the LIL lines such as Hβ, FeII, and the CaII triplet (Panda 2021). We thus assume that this emission must come from the scattering of the central UV radiation.

The presence of highly or fully ionized medium is well supported by observations as well as by the theory. The general picture is nicely illustrated by Ramos Almeida & Ricci (2017), who show the smooth outflow of low density material filling the space between clouds. This medium extends from direct vicinity of a black hole to the narrow line region (NLR) and beyond. In the case of Seyfert 2 galaxies, we see the scattering taking place in the NLR, since the region closer in is still shielded from us, and the reflection reveals the presence of the BLR lines that are otherwise hidden from the observer (Antonucci & Miller 1985). In the case of type 1 sources, we have a clear view down to the nucleus and we see the scatterers all the way down. Closer-in scattering medium consists of hot plasma only. In studies of the polarized light of Seyfert 1 galaxies, these scatterers have been phenomenologically divided into polar and equatorial scatterers (Smith et al. 2004, 2005). However, it well may be a continuous medium, mostly consisting of the innermost fully ionized wind plus intercloud BLR (and further away, also NLR) medium. The amount of such outflows is difficult to estimate, but it has been argued that energy and momentum lead to massive outflows that can be even optically thick for electron scattering (King 2010). The polarization level is rather low, from a fraction of a percent to a few percent (see e.g., Capetti et al. 2021; Popović et al. 2022, for most recent extensive measurements). Such a polarization level is consistent with the optical depth of scatterers on the order of 1, as it largely depends on the viewing angle (Lira et al. 2020). From theoretical point of view, the hot plasma together with the radiation pressure provide the confinement to the clouds (Krolik et al. 1981; Baskin & Laor 2018).

Therefore, the hot medium extending from the black hole vicinity up to BLR distances can scatter a fraction of the nuclear emission towards BLR clouds. Since the temperature of the medium is likely set at a Compton temperature value, $\sim 10^7$ K (Rybicki & Lightman 1986), only Thomson elastic scattering is important. This radiation scattered by the surrounding hot medium reaches to the clouds as illustrated in Fig. 1.

Our previous calculation of column density (Naddaf et al. 2021) indicates that the clouds at higher altitudes are more transparent to the scattered central flux and also to the observer. This

motivates us to give some weight to the otherwise uniform intrinsic emissivity of clouds as a function of their vertical position, namely:

$$\epsilon_{tot} = z \times \epsilon_{int}, \tag{3}$$

where z is the vertical position of clouds relative to the equatorial plane, and ϵ_{int} is the intrinsic constant emissivity of clouds which we assumed to be uniform throughout the LIL BLR.

As shown in Fig. 1, we assume that in case of formation of stream it may block the ionizing scattered central radiation to reach to outer BLR, so no efficient line emission is expected from that part. In the absence of the stream, lines can be produced by the whole BLR.

It should be noted that in our model, no line emission is expected from the disk itself due to shielding effect. In addition, we do not include any "moon effect" in the line calculations. This moon effect can be the important if the individual clouds are optically thick, so that the illuminated side of the clouds are brighter than the dark side, thus emitting more radiation, (see e.g., Goad et al. 2012; Czerny et al. 2017). Since we have not assumed optically thick clouds in our model, all clouds isotropically emit all the energy they receive (absorb), in the form of line emission. Although the model is symmetric with respect to the equatorial plane, only the clouds above the disk can contribute in the line production as the clouds on the other side are obscured by the disk itself.

4.2. Location of clouds in FRADO

In order to find the distribution of clouds in 2.5D FRADO, we first need to know the number of clouds to be launched at any given radius within the LIL BLR, or equivalently, the disk mass loss rate as a function of radius. The total mass loss rate results directly from our dynamical model (Naddaf et al. 2021), however, in order to have it serve as a function of radius, we adopted a method based on the optically thin approximation in stellar winds. Applying this approach to accretion disk, as in Czerny et al. (2017), yields the following mass loss rate:

$$\dot{M}_z \propto r^{-\frac{5}{2}}. \tag{4}$$

Assuming a constant cloud density, we can then calculate the total number of clouds that we have to launch per given radius in our model. We set the cloud density, arbitrarily and case-specifically, with the aim of obtaining a total number of around two million clouds building the LIL BLR. With the knowledge of the theoretical number of clouds launched at a given radius, a uniform random number generator (URNG) is then used in the following way to provide a non-biased random distribution of clouds. For each cloud launched at a radius, a URNG is used to randomly determine the azimuthal angle at which the cloud should be launched. This is due to that while we do have azimuthal symmetry in our model, we ultimately need a 3D distribution of clouds since the inclined observer breaks the symmetry. We use URNG again for the same launched cloud to find its random position along its trajectory, taking into account the velocity profile along the trajectory.

5. Results

5.1. Trajectories of BLR clouds

Figure 2 displays the trajectories of clouds launched at different radii within LIL BLR for the range of our three main initial physical parameters, namely, black hole mass, accretion rate,
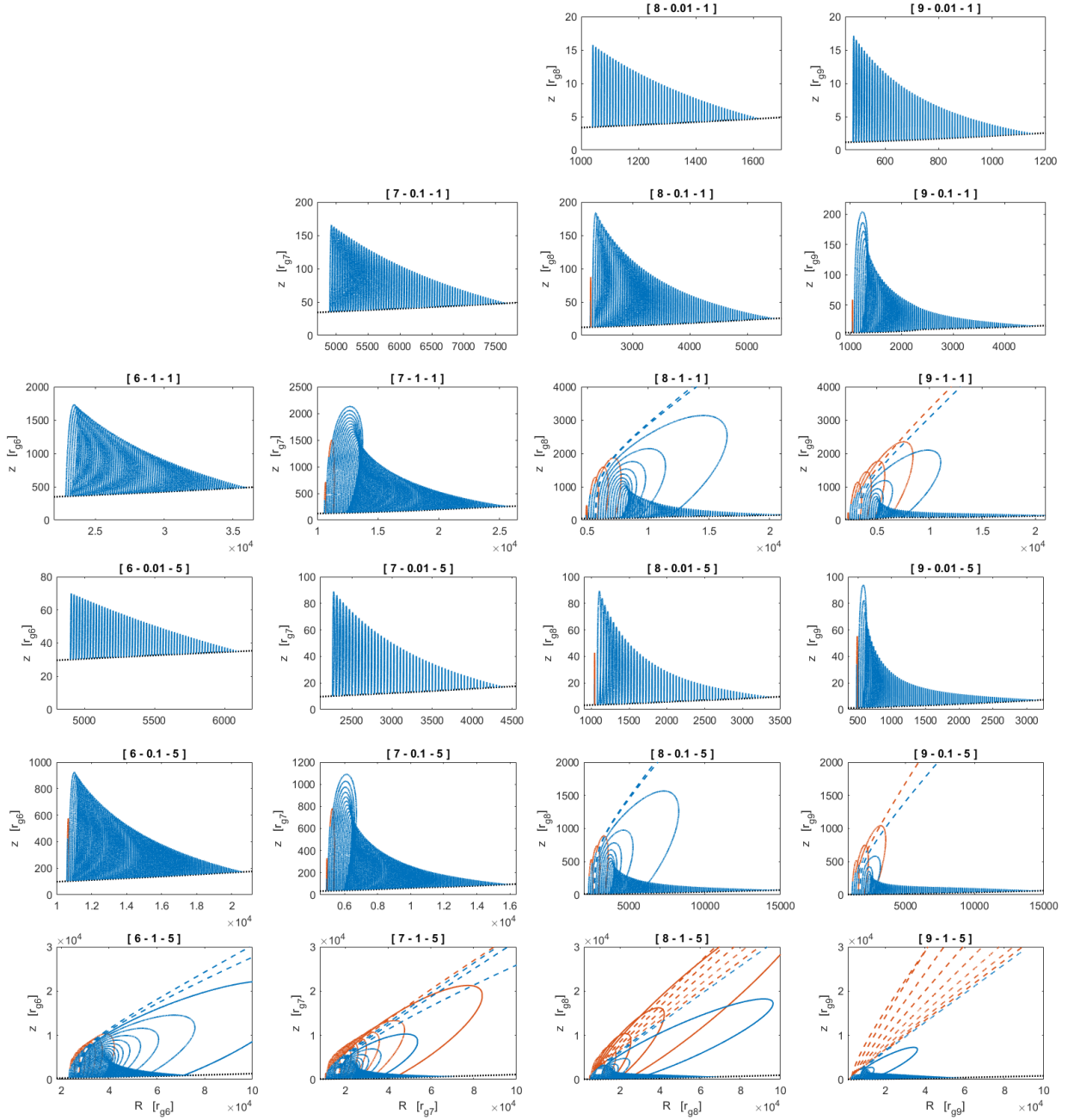
Fig. 2. Trajectories of clouds within BLR in FRADO. The three numbers *from left to right* in brackets atop of each panel stand for log of black hole mass in solar units, accretion rate in Eddington units, and the metallicity in solar units, respectively. The blue and red solid (or dashed) lines show the path of motion of dusty and dustless failed (or escaping) clouds, respectively. The black dotted line represents the disk surface.

and metallicity. The computation of trajectories are done for a very dense equally spaced set of initial radii within the region but only a small fraction of them are plotted for the matter of better visibility. The three blank panels in Fig. 2 indicate that radiation pressure was not efficient enough in those cases to launch any material from the disk.

The results are expressed in terms of black hole mass corresponding gravitational radius defined as:

$$r_{\rm g} = \frac{GM_{\rm BH}}{c^2},\qquad(5)$$

which is the minimum for the smallest black hole mass of $10^6\ M_\odot$ in our sample, that is,

$$r_{\rm g(6)} = 4.78 \times 10^{-8}\ [{\rm pc}] = 5.7 \times 10^{-5}\ [{\rm lt\text{-}day}].\qquad(6)$$

As can be seen, the funnel-shaped stream of material can form and get broader with an increase of not only black hole mass and accretion rate, but also with the increase in the dust-to-gas ratio parameter. The stream shows the smallest inclination (relative to the symmetry axis) for the largest values of initial parameters in our model grid, as visible in the bottom-right panel of Fig. 2. The radial extension of BLR, namely, the whole radial range within which a cloud can be lifted from the disk surface also becomes larger with the increase of the values of initial parameters. In our previous study, carried out for the fixed black hole mass of $10^8\ M_\odot$, we showed that the character of motion in 2.5D FRADO strongly depends on the accretion rate. Now, for the large grid of
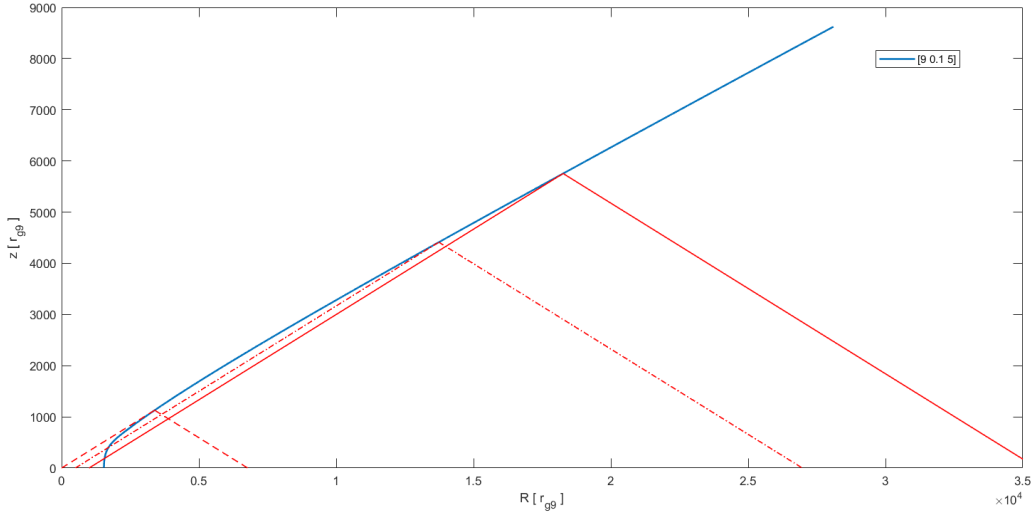
Fig. 3. Illustration of the shielding effect in our model. Here, we show the radial extension of the disk area seen by the selected flying cloud at three different exemplary positions along its trajectory, for the case of escaping cloud launched at $1540\,r_g$ with black hole mass of $10^9\,M_\odot$, Eddington rate of 0.1, and five times solar metallicity. The cloud located at vertical position of around 1100, 4500, and $5800\,r_g$ along its trajectory, sees the radial range of [0–6700], [500–26 800], and [1000–35 600] r_g, respectively. The model assumes the radial visibility as three times higher than the local cloud height ($\alpha = 3$, see Naddaf et al. 2021), so the area at the starting point is very small and we cannot show the early stages in this graphical scale, but the cloud is well exposed to the whole disk irradiation after reaching the height of $1000\,r_g$. Other clouds may never achieve such exposure to the disk central parts.

initial parameters, we can already see that it strongly depends not only on the Eddington rate of the source, but also strongly on the black hole mass and dust-to-gas ratio.

As seen from the results plotted in Fig. 2, there are eight cases in our model grid, each corresponding to a different set of initial parameters, for which the component c (i.e., the outflow stream) is formed. As a result, the component a (i.e., the outer tail) is not expected to contribute in line production as it does not receive the ionizing scattered radiation.

We also provide a scaled illustration of the action of shielding effect in detail in Fig. 3 for the case of an escaping trajectory for a model with black hole mass of $10^9\,M_\odot$, accretion rate of 0.1 in Eddington units, and five times solar metalicity. We illustrate the increasing fraction of the disk visible to the cloud as it moves along the trajectory. This cloud, when reaching a height of around $10^3\,r_g$, is illuminated by the central disk flux. Generally in our model, the clouds for high mass, high accretion rate, and high metallicity can or may be fully directly irradiated when they reach relatively large distances from the center. However, low mass, low Eddington ratio, and low metallicity solutions never predict strong direct exposure of the clouds to full irradiation. In such cases, from the observational point of view, LIL lines do form as well and show the double-peaked profiles, suggesting the line origin to be close to the disk surface, whereas direct irradiation in this case is highly inefficient (see e.g., Loska et al. 2004). This is consistent with the findings from our model.

5.2. Line profiles

Figure 4 shows the full grid of predicted line profiles for the distribution of clumps building the LIL BLR seen at different viewing angles. The line shapes shown in this figure were smoothed with spline technique for better appearance. We set the values of 15, 30, and 45 deg as the representative values for the viewing angle for type 1 AGNs. For these sources, the viewing angle is never very large as the BLR is then obscured by the torus (Antonucci 1993; Netzer 2015).

Consistently with the observations, the lines get narrower with the Eddington ratio (Pounds et al. 1995; Du et al. 2016) of the source and become broader along the black hole mass. Except for the high Eddington rate and high black hole masses, the predicted lines at solar metallicity are dominated by the disk-like shape. However, the higher value of metallicity changes the picture as it allows the efficient rise of material above the disk with vertical velocities comparable to those of the rotational Keplerian one. Generally, an overall view shows that all cases in which the component c of BLR (as shown in Fig. 1) is developed, a single-peaked profile can be expected; other cases without this component give rise to double-peaked line profiles. Comparing the line shapes by eye in terms of the metallicity, we can feasibly argue that the increase of the metallicity by a factor of five corresponds to the increase of the Eddington ratio of the source by a factor of ten. Likewise, we can expect single-peaked profiles for all super-Eddington sources regardless of the black hole mass and metallicity.

There are two important features in the single-peaked predicted profiles: asymmetry and blue-shift. The asymmetry cannot be due to the difference between the time duration of rise and fall of the clouds since in all cases only a very small fraction of failed clouds pass the sublimation location and lose their dust content and continue their motion as a ballistic motion. It means that most clouds complete their full orbit while keeping their dust content so that their motion are not expected to cause line asymmetry. As can be implied from both Figs. 2 and 4, the more intense and broad the outflow stream, the more asymmetric and blue-shifted the line shapes appear. Thus, these two features are interrelated implying that the outflow is dominant compared to the failed part of BLR.

6. Discussion

6.1. Comparison with 1D FRADO

The line shapes predicted by the 2.5D FRADO model show considerable improvement, even approaching characteristic
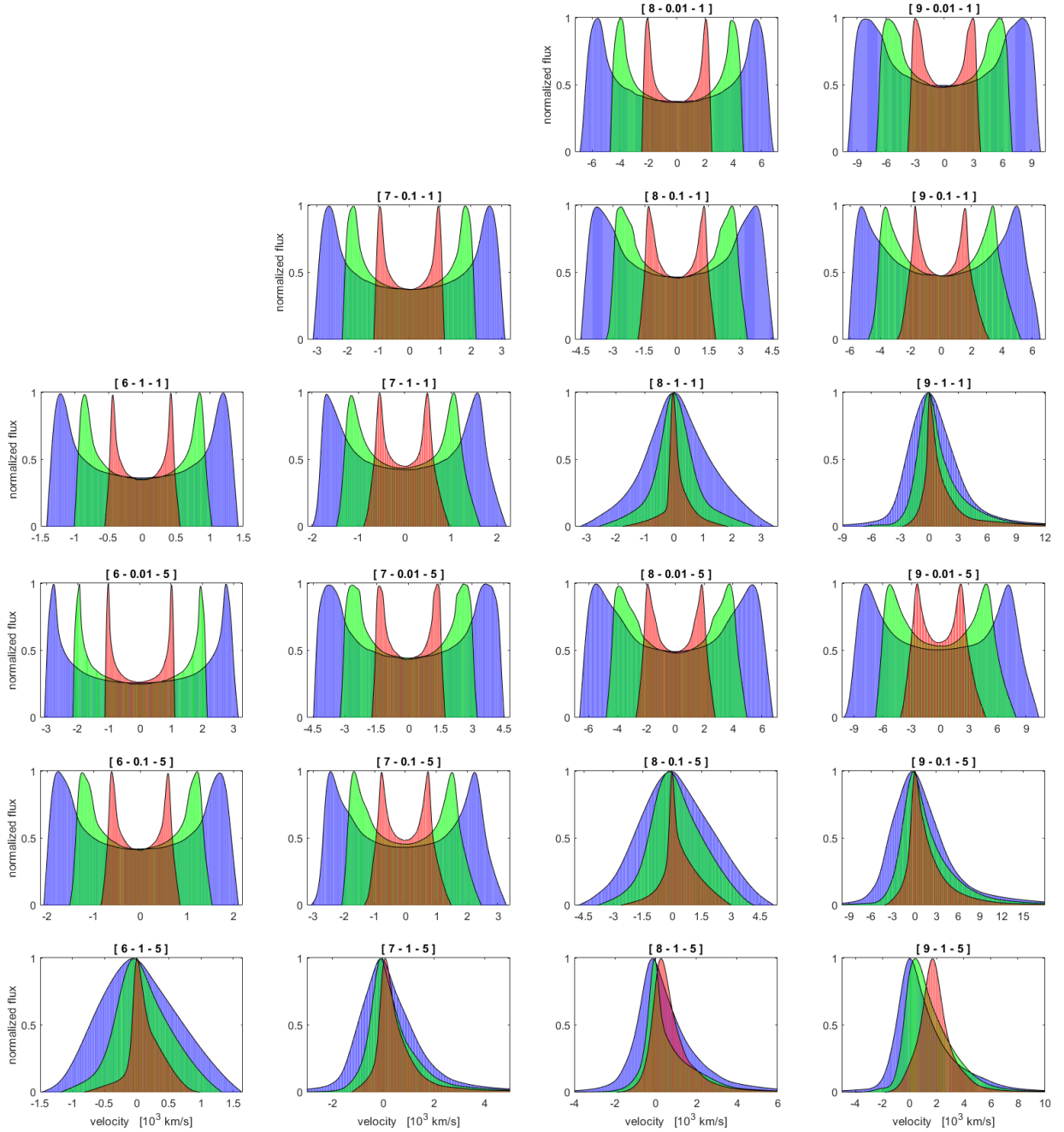
Fig. 4. Predicted dependence of line Profiles (normalized flux to one) on the accretion rate, black hole mass, and dust-to-gas ratio. The numbers in brackets are as in Fig. 2. Lines are color coded with red, green, and blue for the corresponding viewing angles of 15, 30, and 45, respectively.

Lorentzian profiles for high Eddington high black hole mass sources as compared to 1D FRADO, where the double-peaked structure was always obtained (Czerny et al. 2017).

In comparison with the 1D model with constant wavelength-averaged opacities, the 2.5D model is enhanced with the advanced realistic wavelength-dependent values of dust opacities where the dust-to-gas ratio regulates the strength of the radiative force. Increasing the dust-to-gas ratio from a solar value to five times solar (appropriate for quasars as discussed before) leads to a major improvement of the line shape toward single-peaked profiles characteristic for high accretors; whereas this could be obtained in 1D model if the wavelength-averaged dust opacity was greatly increased by a (not entirely realistic) factor of 1000 (Czerny et al. 2017).

6.2. Composite spectrum (mean quasar)

The mean composite quasar spectrum (Vanden Berk et al. 2001) from the Sloan Digital Sky Survey (SDSS) shows that a single-peaked line profile is expected for the LIL BLR. Such a spectrum represents quasars in SDSS data well (Shen et al. 2011), where the mean value of the black hole mass is $10^9 \, M_\odot$ (Swayamtrupta Panda, priv. comm.), and the mean Eddington ratio is 0.1 (Panda et al. 2018). We thus compared the model, taking the parameters as appropriate for the mean quasar to the MgII and Hβ line shape (shown in Fig. 5). With this aim, we locally subtracted the underlying power-law and then overplotted the theoretical shape of the line assuming arbitrary normalization. In the case of the Hβ line, prior removal of the narrow
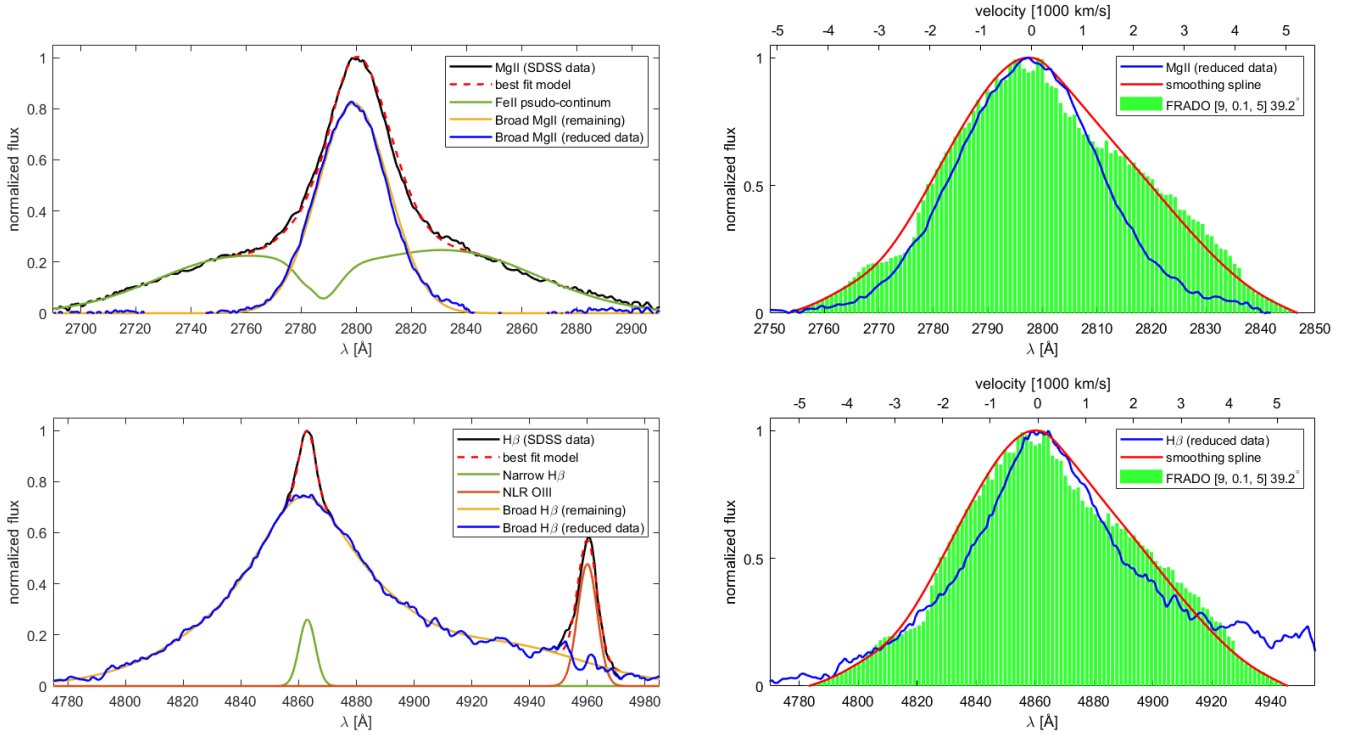
Fig. 5. *Right panels*: comparison of the fully corrected MgII and Hβ lines in the mean composite quasar spectrum from SDSS data to the line profile predicted by 2.5D FRADO for cases corresponding to the mean quasar physical parameters (black hole mass of $10^9\,M_\odot$, Eddington rate of 0.1) with metallicity of five times solar, viewed at 30 deg. *Left panels*: power-law-subtracted MgII and Hβ lines from SDSS data are decomposed into different components, as indicated in the plot legends.

Hβ component as well as [OIII] lines coming from the NLR was necessary, and for that we fixed the width of these components at $205\,\mathrm{km\,s^{-1}}$ and $220\,\mathrm{km\,s^{-1}}$ for Hβ and OIII, respectively. As for the MgII line, we used the semi-empirical UV FeII template[1] (Kovačević-Dojčinović & Popović 2015; Popović et al. 2019) to remove the FeII pseudo-continuum in the required spectral band. We see that the results show a nice fit with the data for the LIL part of BLR.

6.3. FWHM vs. σ_{line}

The ratio of the FWHM to the line dispersion, σ_{line}, is an important parameter (Collin et al. 2006) characterizing the line profile, although it does not differentiate between a single and double-peaked profiles. We calculated this ratio for the grid of our initial physical parameters (with Fig. 6 displaying the results). Most models are roughly consistent with the ratio expected for a Gaussian, but for high-mass, high-Eddington ratio models, this ratio dropped considerably, indicating that we are approaching Lorentzian profiles. Therefore, although the Lorentzian profiles might simply be expected for extremely low viewing angles (e.g., Goad et al. 2012), our results show that sources with high mass high Eddington ratio can generally lead to relatively Lorentzian shapes, regardless of the viewing angle. Moreover, the larger the black hole mass and accretion rate are, the more asymmetry and blue-shift in the line shape we have, as shown in Fig. 4.

This trend is overall consistent with the data (see e.g., Marziani et al. 2003). The strong trend with the change of the viewing angle is visible for high Eddington sources, whereas for the remaining sources, the effect is weak when FWHM/σ_{line}

---

[1] http://servo.aob.rs/FeII_AGN/link7.html

is used. What is somewhat surprising is the very strong trend related to the black hole mass, which is also visible in Fig. 4.

6.4. Model assumptions

In our model, we used a non-hydrodynamical approach based on assumptions of the motion of separate clouds under gravity and the action of radiation pressure acting on dust. This has considerable limitations but they are justified as the first approximation for modeling the LIL part of the BLR. As discussed in the classical paper of line-driven wind model (for HIL part of BLR) by Murray et al. (1995), the optical depth of the emitting region must be moderate (column density of order of $10^{23}\,\mathrm{cm^{-2}}$) and the local density is high (for LIL part it is higher than that of HIL, many authors argue for a local density about $10^{12}\,\mathrm{cm^{-3}}$, for instance, Adhikari et al. 2016; Baskin & Laor 2018; Panda et al. 2018), while the BLR is extended. There are two possibilities to support a consistent picture: it is either to assume a very narrow stream of material flowing out, with the cross-section on the order of $10^{12}\,\mathrm{cm}$, as in Murray et al. (1995), where they assume lower density so the size is actually larger $10^{14}\,\mathrm{cm}$; or to assume considerable clumpiness of the medium. We followed the second approach since there are natural thermal instabilities in the plasma, such as instability caused by X-ray irradiation (Krolik et al. 1981). In this case, the plasma spontaneously forms colder clumps (at a temperature of $\sim10^4\,\mathrm{K}$, cooled through atomic processes) embedded in a hotter medium (at temperature $\sim10^7\,\mathrm{K}$, set at an inverse Compton temperature value). The presence of highly or fully ionized medium is aptly supported by the observations as well as by the theory. Then the two media of density contrast of order of 10^3 provide the rough pressure balance. Blandford et al. (1990) discussed the typical values for
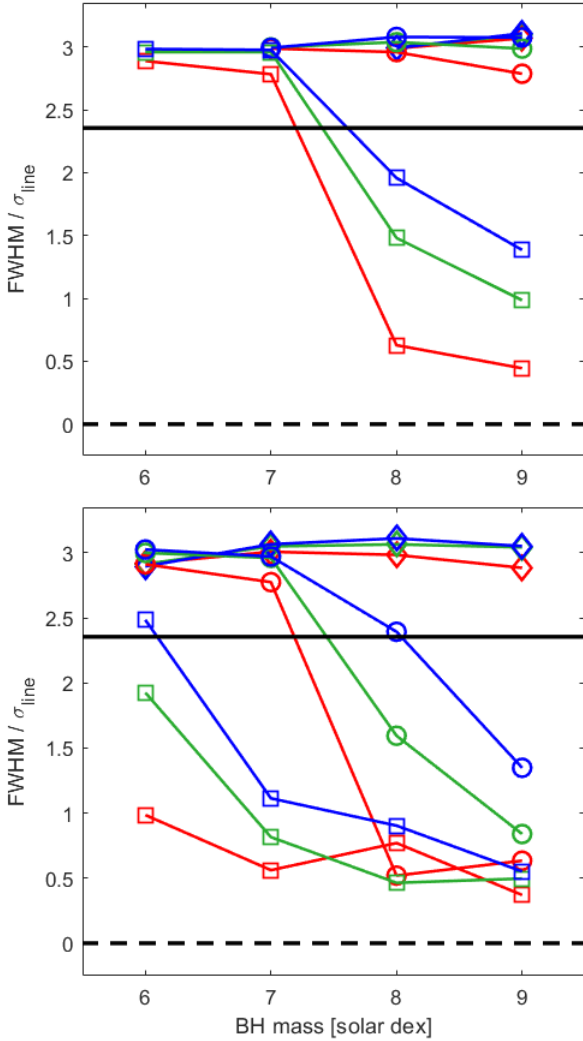
Fig. 6. Dependence of the ratio of FWHM/σ_{line} on the initial physical parameters for the solar (*upper panel*) and five times solar metallicity (*lower panel*). The red, green, and blue solid lines represents the viewing angles of 15, 30, and 45 deg, respectively. The diamonds, circles, and squares stand for the Eddington rates of 0.01, 0.1, and 1, respectively. The values of 2.3548 and zero expected for a Gaussian and Lorentzian profile are depicted by black solid and black dashed lines, respectively, for a reference.

ionization parameter in AGN clouds covering the range from 10^{-3} to 1, that is, up to four orders of magnitudes. The precise description of the structure of the clumpy medium is very difficult. Even in the case of a single cloud exposed to irradiation, in plane-parallel approximation requires a radiative transfer to be performed, which would then show the gradual change in the density, temperature, and ionization parameters (see e.g., Baskin & Laor 2018; Adhikari et al. 2018), with the low density first and the temperature roughly at inverse Compton temperature (depending on the shape of the incident spectrum), and then a relatively rapid decrease at the subsequent ionization fronts. A proper description of this transition, calculated under constant pressure, actually requires inclusion of the electron conduction (e.g., Begelman & McKee 1990; Różańska & Czerny 2000). Deep within the cloud, there is a further drop in temperature and a rise in density due to a decrease in the local flux as a result of absorption. As emphasized by Baskin & Laor (2018), radiation pressure also plays a dynamical role in this pro-

cess. The picture is further complicated if plane-parallel approximation is abandoned. The presence of the numerous clouds of complex shapes can be fully consistent with simple estimates of the cloud number based on line shape properties as done by Arav et al. (1998). Of course, there are also certain processes that can lead to cloud destruction, such as the action of tidal forces (Müller et al. 2022), Kelvin–Helmholtz instabilities, and cloud ablation), however, the destruction rate can be strongly affected by the magnetic field (e.g., McCourt et al. 2015). The relative importance between the condensation rate and destruction rate depends on the cloud size, as it is set roughly by the field length (Field 1965). Cloud formation in AGN has been seen in the numerical simulations from Waters et al. (2021), but at distances much greater than the BLR distance which was likely related to the numerical setup and the requested spatial resolution of the computations. The issue is thus extremely complex, and simple order-of-magnitude estimates based on a single density and single temperature of the cloud and intercloud medium are not fully adequate and cannot reproduce the full ionization parameter range. However, addressing this point in detail is beyond the scope of the current paper.

Our model contains one more important simplification. We assumed only the action of the radiation pressure acting on the dust, and we neglect the line driving effect. Close to the launching point, the local flux comes from the disk, without any considerable UV component, but when the clouds is alleviated high above the disk, the line-driving effect should set in. There have been numerous papers addressing the line-driven winds (Murray et al. 1995; Proga et al. 2000; Risaliti & Elvis 2010; see Giustini et al. 2020 for a recent review) but none of the studies have combined dust radiation pressure and line pressure in this context since the way of determining the radiative force is very different in these two scenarios. Our negligence of the line driving is most likely appropriate for description of launching clouds at the LIL BLR, but it underestimated the cloud velocities when the outflowing stream of the material forms. This effect should be incorporated in the future studies; specifically, we should combine our code with the QWIND (Risaliti & Elvis 2010; Quera-Bofarull et al. 2021) but this is not easy even in the case of non-hydrodynamical simulations.

The expected higher velocities of the clouds due to line driving will partially be slowed down by the interaction of the clouds with the ambient medium, which is also neglected in our model. The freshly launched clouds and inter-cloud medium are co-moving since clouds form through thermal instability. However, accelerating clouds detach from their surrounding and, thereby, some drag force is expected, although clouds are much denser than the ambient medium (roughly in pressure equilibrium) and the relative velocities between the hot medium and the clouds are not very high. This is because clouds and the intercloud medium likely share the Keplerian motion component of the velocity and follow the same initial vertical velocity gained before the fragmentation of the medium into clouds occurred.

Wind models having elements of the radiative transfer show single-peaked lines (Murray et al. 1995; Waters et al. 2016). In our work, with a simplified non-hydrodynamic approach to the dynamics of material in LIL BLR, the single-peaked profiles are obtained without incorporating the process of radiative transfer into the emissivity of clouds.

In a future work, it will be necessary to address the issue of cloud emissivity in more detail, including line formation in the dusty medium. However, this effect is strongly dependent not only on cloud irradiation but also on cloud local densities. At low densities, the presence of dust suppresses line

emission (Netzer & Laor 1993), while at high densities (above $10^{11.5}$ cm^{-3}), emission lines do form efficiently even in the presence of the dust. This explains the absence of a gap between the NLR and BLR region in narrow-line Seyfert 1 galaxies (Adhikari et al. 2016).

The assumption of the dust sublimation temperature fixed in the at 1500 K is simple to relax, and higher (or lower) temperature will predominantly shift the position of the BLR outward (or inward). This will be important for precise comparison of the radius–luminosity relation to the observational data, but we do not yet focus on this goal here. Indeed, a higher average temperature of ~1700 K is quite likely, but 1500 K is still frequently assumed even in data analysis (e.g., GRAVITY Collaboration 2020b) and broadband spectral fitting of the dust emission in AGN gives the values in individual sources in the range of 1000–1750 K (Hernán-Caballero et al. 2016). The more advanced approach, taking into account the specific dust species, like silicates, amorphous carbon, and so on, and the dependence of the sublimation temperature not only on the chemical composition, but also on specific grain size is far more complicated since the loss of the driving pressure force would be gradual, and the dust composition would have to be recalculated at each integration step for each cloud trajectory. This should be done at some stage, but a number of simplifications still used to recover the dynamics and the line emissivity do not yet require such an advanced approach.

7. Summary

Following our previous work on the dynamical character and shape of LIL BLR based on the non-hydrodynamic single-cloud 2.5D FRADO model (Naddaf et al. 2021), we here tested the model by calculation of line profiles for the model-concluded distribution of clouds along their trajectories within LIL BLR, for a relatively large grid of initial conditions. We adopted a simple approach, assuming a constant cloud density and without the element of radiative transfer included.

The predicted trend in the line shape seems consistent with observations, as the model implies narrower (or broader) line shape for sources with larger Eddington ratio (or smaller black hole mass). All solutions with a developed outflow stream of material show up single-peaked profiles, and the line shape approaches a Lorentzian shape for a high-mass high Eddington ratio. In other cases, a double-peaked disk-like line shape dominates.

Two features, namely: asymmetry and blue-shifting, seen in the line shapes developed in the cases with outflow streams show that the outflow is dominant compared to failed trajectories. These features were more visibly intense for the sources with high black hole mass and high Eddington ratios. Most importantly, we showed that the line profile predicted by our model for the case with initial physical parameters corresponding to those of the mean quasar is consistent with observed mean spectrum seen in the SDSS composite.

References

Adhikari, T. P., Różańska, A., Czerny, B., Hryniewicz, K., & Ferland, G. J. 2016, ApJ, 831, 68
Adhikari, T. P., Hryniewicz, K., Różańska, A., Czerny, B., & Ferland, G. J. 2018, ApJ, 856, 78
Antonucci, R. 1993, ARA&A, 31, 473
Antonucci, R. R. J., & Miller, J. S. 1985, ApJ, 297, 621
Arav, N., Barlow, T. A., Laor, A., Sargent, W. L. W., & Blandford, R. D. 1998, MNRAS, 297, 990
Artymowicz, P. 1993, PASP, 105, 1032
Artymowicz, P., Lin, D. N. C., & Wampler, E. J. 1993, ApJ, 409, 592
Baldwin, J. A. 1997, in IAU Colloq. 159: Emission Lines in Active Galaxies: New Methods and Techniques, eds. B. M. Peterson, F. Z. Cheng, & A. S. Wilson, ASP Conf. Ser., 113, 80
Baskin, A., & Laor, A. 2018, MNRAS, 474, 1970
Begelman, M. C., & McKee, C. F. 1990, ApJ, 358, 375
Bentz, M. C., Walsh, J. L., Barth, A. J., et al. 2009, ApJ, 705, 199
Bentz, M. C., Denney, K. D., Grier, C. J., et al. 2013, ApJ, 767, 149
Blandford, R. D., & McKee, C. F. 1982, ApJ, 255, 419
Blandford, R. D., Netzer, H., Woltjer, L., Courvoisier, T. J. L., & Mayor, M. 1990, Active Galactic Nuclei (Berlin: Springer-Verlag)
Boroson, T. A., & Green, R. F. 1992, ApJS, 80, 109
Capetti, A., Laor, A., Baldi, R. D., Robinson, A., & Marconi, A. 2021, MNRAS, 502, 5086
Castro, C. S., Dors, O. L., Cardaci, M. V., & Hägele, G. F. 2017, MNRAS, 467, 1507
Collin-Souffrin, S., Dyson, J. E., McDowell, J. C., & Perry, J. J. 1988, MNRAS, 232, 539
Collin, S., Kawaguchi, T., Peterson, B. M., & Vestergaard, M. 2006, A&A, 456, 75
Czerny, B., & Hryniewicz, K. 2011, A&A, 525, L8
Czerny, B., Du, P., Wang, J.-M., & Karas, V. 2016, ApJ, 832, 15
Czerny, B., Li, Y.-R., Hryniewicz, K., et al. 2017, ApJ, 846, 154
Dietrich, M., Hamann, F., Shields, J. C., et al. 2003, ApJ, 589, 722
Dong, X., Wang, T., Wang, J., et al. 2008, MNRAS, 383, 581
Du, P., Wang, J.-M., Hu, C., et al. 2014, MNRAS, 438, 2828
Du, P., Lu, K.-X., Zhang, Z.-X., et al. 2016, ApJ, 825, 126
Dyda, S., & Proga, D. 2018, MNRAS, 475, 3786
Elvis, M. 2000, ApJ, 545, 63
Esparza-Arredondo, D., Gonzalez-Martín, O., Dultzin, D., et al. 2021, A&A, 651, A91
Ferland, G. J., Baldwin, J. A., Korista, K. T., et al. 1996, ApJ, 461, 683
Field, G. B. 1965, ApJ, 142, 531
Ganguly, S., Proga, D., Waters, T., et al. 2021, ApJ, 914, 114
Gaskell, C. M. 2009, New Astron. Rev., 53, 140
Gezari, S., Halpern, J. P., & Eracleous, M. 2007, ApJS, 169, 167
Giustini, M., & Proga, D. 2020, in Nuclear Activity in Galaxies Across Cosmic Time, eds. M. Pović, P. Marziani, J. Masegosa, et al., 356, 82
Goad, M. R., Korista, K. T., & Ruff, A. J. 2012, MNRAS, 426, 3086
GRAVITY Collaboration (Sturm, E., et al.) 2018, Nature, 563, 657
GRAVITY Collaboration (Amorim, A., et al.) 2020a, A&A, 643, A154
GRAVITY Collaboration (Dexter, J., et al.) 2020b, A&A, 635, A92
GRAVITY Collaboration (Amorim, A., et al.) 2021, A&A, 648, A117
Grier, C. J., Peterson, B. M., Horne, K., et al. 2013, ApJ, 764, 47
Guerras, E., Mediavilla, E., Jimenez-Vicente, J., et al. 2013, ApJ, 764, 160
Hamann, F. 1997, ApJS, 109, 279
Hamann, F., & Ferland, G. 1992, ApJ, 391, L53
Hernán-Caballero, A., Hatziminaoglou, E., Alonso-Herrero, A., & Mateos, S. 2016, MNRAS, 463, 2064
Horne, K., Welsh, W. F., & Peterson, B. M. 1991, ApJ, 367, L5
Ilić, D., Popović, L. Č., La Mura, G., Ciroi, S., & Rafanelli, P. 2012, A&A, 543, A142
Kaspi, S., Smith, P. S., Netzer, H., et al. 2000, ApJ, 533, 631
King, A. R. 2010, MNRAS, 402, 1516
Kovačević-Dojčinović, J., & Popović, L. Č. 2015, ApJS, 221, 35
Krolik, J. H., & Done, C. 1995, ApJ, 440, 166
Krolik, J. H., McKee, C. F., & Tarter, C. B. 1981, ApJ, 249, 422
Lawrence, A., Elvis, M., Wilkes, B. J., McHardy, I., & Brandt, N. 1997, MNRAS, 285, 879
Le, H. A. N., & Woo, J.-H. 2019, ApJ, 887, 236
Li, Y.-R., Wang, J.-M., Ho, L. C., Du, P., & Bai, J.-M. 2013, ApJ, 779, 110
Li, Y.-R., Wang, J.-M., & Bai, J.-M. 2016, ApJ, 831, 206
Li, S.-S., Yang, S., Yang, Z.-X., et al. 2021, ApJ, 920, 9
Lira, P., Goosmann, R. W., Kishimoto, M., & Cartier, R. 2020, MNRAS, 491, 1
Loska, Z., Czerny, B., & Szczerba, R. 2004, MNRAS, 355, 1080
Lu, K.-X., Wang, J.-G., Zhang, Z.-X., et al. 2021, ApJ, 918, 50
Marziani, P., Sulentic, J. W., Zamanov, R., et al. 2003, ApJS, 145, 199
Mathis, J. S., Rumpl, W., & Nordsieck, K. H. 1977, ApJ, 217, 425
Matteucci, F., & Padovani, P. 1993, ApJ, 419, 485
McCourt, M., O'Leary, R. M., Madigan, A.-M., & Quataert, E. 2015, MNRAS, 449, 2
Mizumoto, M., Done, C., Tomaru, R., & Edwards, I. 2019, MNRAS, 489, 1152
Müller, A.L., Naddaf, M.H., Zajaček, M., et al. 2022, ApJ, 931, 39

Murray, N., Chiang, J., Grossman, S. A., & Voit, G. M. 1995, ApJ, 451, 498

Naddaf, M.-H., Czerny, B., & Szczerba, R. 2020, Front. Astron. Space Sci., 7, 15

Naddaf, M.-H., Czerny, B., & Szczerba, R. 2021, ApJ, 920, 30

Negrete, C. A., Dultzin, D., Marziani, P., et al. 2018, A&A, 620, A118

Netzer, H. 2013, The Physics and Evolution of Active Galactic Nuclei (Cambridge: Cambridge University Press)

Netzer, H. 2015, ARA&A, 53, 365

Netzer, H. 2020, MNRAS, 494, 1611

Netzer, H., & Laor, A. 1993, ApJ, 404, L51

Osterbrock, D. E. 1977, ApJ, 215, 733

Osterbrock, D. E. 1981, ApJ, 249, 462

Pancoast, A., Brewer, B. J., & Treu, T. 2011, ApJ, 730, 139

Pancoast, A., Brewer, B. J., & Treu, T. 2014, MNRAS, 445, 3055

Panda, S. 2021, A&A, 650, A154

Panda, S., Czerny, B., Adhikari, T. P., et al. 2018, ApJ, 866, 115

Peterson, B. M., Ferrarese, L., Gilbert, K. M., et al. 2004, ApJ, 613, 682

Popović, L. Č., Kovačević-Dojčinović, J., & Marčeta-Mandić, S. 2019, MNRAS, 484, 3180

Popović, L. Č., Shablovinskaya, E., & Savić, D. 2022, Astron. Nachr., 343, e210089

Pounds, K. A., Done, C., & Osborne, J. P. 1995, MNRAS, 277, L5

Proga, D., & Kallman, T. R. 2004, ApJ, 616, 688

Proga, D., Stone, J. M., & Kallman, T. R. 2000, ApJ, 543, 686

Quera-Bofarull, A., Done, C., Lacey, C. G., Nomura, M., & Ohsuga, K. 2021, ArXiv e-prints [arXiv:2111.02742]

Raimundo, S. I., Vestergaard, M., Goad, M. R., et al. 2020, MNRAS, 493, 1227

Ramos Almeida, C., & Ricci, C. 2017, Nat. Astron., 1, 679

Rees, M. J., Silk, J. I., Werner, M. W., & Wickramasinghe, N. C. 1969, Nature, 223, 788

Reeves, J. N., & Turner, M. J. L. 2000, MNRAS, 316, 234

Risaliti, G., & Elvis, M. 2010, A&A, 516, A89

Röllig, M., Szczerba, R., Ossenkopf, V., & Glück, C. 2013, A&A, 549, A85

Różańska, A., & Czerny, B. 2000, MNRAS, 316, 473

Różańska, A., Czerny, B., Życki, P. T., & Pojmański, G. 1999, MNRAS, 305, 481

Różańska, A., Goosmann, R., Dumont, A. M., & Czerny, B. 2006, A&A, 452, 1

Rybicki, G. B., & Lightman, A. P. 1986, Radiative Processes in Astrophysics (Germany: Wiley-VCH)

Shakura, N. I., & Sunyaev, R. A. 1973, A&A, 500, 33

Shangguan, J., Ho, L. C., & Xie, Y. 2018, ApJ, 854, 158

Shen, Y., Richards, G. T., Strauss, M. A., et al. 2011, ApJs, 194, 45

Shlosman, I., Vitello, P. A., & Shaviv, G. 1985, ApJ, 294, 96

Sluse, D., Hutsemékers, D., Courbin, F., Meylan, G., & Wambsganss, J. 2012, A&A, 544, A62

Smith, J. E., Robinson, A., Alexander, D. M., et al. 2004, MNRAS, 350, 140

Smith, J. E., Robinson, A., Young, S., Axon, D. J., & Corbett, E. A. 2005, MNRAS, 359, 846

Sniegowska, M., Marziani, P., Czerny, B., et al. 2021, ApJ, 910, 115

Sulentic, J. W., Marziani, P., & Dultzin-Hacyan, D. 2000, ARA&A, 38, 521

Szczerba, R., Omont, A., Volk, K., Cox, P., & Kwok, S. 1997, A&A, 317, 859

Vanden Berk, D. E., Richards, G. T., Bauer, A., et al. 2001, AJ, 122, 549

Voit, G. M. 1992, MNRAS, 258, 841

Wandel, A., Peterson, B. M., & Malkan, M. A. 1999, ApJ, 526, 579

Wang, J.-M., Qiu, J., Du, P., & Ho, L. C. 2014, ApJ, 797, 65

Ward, R. L., Wadsley, J., & Sills, A. 2014, MNRAS, 445, 1575

Warner, C., Hamann, F., Shields, J. C., et al. 2002, ApJ, 567, 68

Waters, T., Kashi, A., Proga, D., et al. 2016, ApJ, 827, 53

Waters, T., Proga, D., & Dannen, R. 2021, ApJ, 914, 62

Xu, F., Bian, F., Shen, Y., et al. 2018, MNRAS, 480, 345

Zhang, Z.-X., Du, P., Smith, P. S., et al. 2019, ApJ, 876, 49

Chapter 6

Summary & perspects

6.1 Summary

The active supermassive black holes in the center of galaxies play a key, but yet poorly understood, role in the evolution of galaxies. The inflowing, and/or outflowing gas associated with black hole accretion may either trigger or quench star formation, modifying profoundly galaxy appearance over cosmic time. The understanding of this phenomenon requires a better knowledge of the physical processes taking place at the closest vicinity of the central black hole, a region spatially unresolved with our telescopes, and where broad emission lines are formed. Broad strong emission lines are the most characteristic features in the optical/UV spectra of most unobscured galaxies with active nuclei (AGN). The exact geometry and kinematics of the emitting gas is still subject to debate as a variety of profiles are observed. These lines manifesting in either single-peaked or double-peaked profiles initiate from clouds orbiting the black hole at a few hundred (Wandel et al., 1999) up to few thousand gravitational radii (Markowitz et al., 2014). Coexistence of broad lines with the cold disk strongly points to the link between the cloud formation and the cold standard disk itself (e.g., Czerny et al., 2004). These broad lines are further divided into High Ionization Lines (HIL) emitted by hotter and lower-density clouds, and Low Ionization Lines (LIL) originating from cooler, denser clouds located further away from the central black hole than HIL medium (Collin-Souffrin et al., 1988). The measured time delays are shorter for HIL lines like HeII and CIV, while LIL represented by Balmer lines and the MgII emission show longer delays, indicating a stratification of the emission with the ionisation degree (Peterson & Wandel, 1999; Zajaček et al., 2021).

To explain the stratification of the BLR, Murray et al. (1995) proposed an efficient model of line-driven wind from the accretion disk as a natural source of HIL, which gained momentum with numerical studies supporting the wind launching (Proga et al., 2000; Waters et al., 2022). On the other hand, the most successful non-adhoc theoretically-motivated models proposed by Czerny & Hryniewicz (2011), known as FRADO (Failed Radiatively Accelerated Dusty Outflow), explains LIL in AGN through the dust-driving mechanism. It addresses the radiative acceleration of theoretically existing dusty material at the surface layers of the disk at radii where the effective temperature drops below the dust sublimation temperature of order of 1000 K. This sets the onset radius from which outwards the low ionized material is located. It is different from the onset of dusty torus which is determined based on the spherically approximated radiation from the central disk. As the model

69

describes, the dusty material in the form of clumps (clouds) ejected from the disk moves in the field of disk radiative force and gravitational potential of blackhole. In case of reaching high altitudes above the disk, it loses dust content due to being irradiated by the intense central disk radiation, so later it follows a ballistic motion falling back onto the disk. The basic one dimensional analytical form of the model (Czerny et al., 2017) successfully predicted the inner/outer radius of LIL-BLR, asymmetry in line profiles (due to dust evaporation), observationally consistent line shape parameter FWHM/σ, dependence of virial factor on black hole mass, and most interestingly the radius-luminosity (RL) relation which is a relation between the absolute luminosity of the source and distance of its broad line region (BLR) from the central black hole. The latter, if fully calibrated, allows the utilization of AGNs, or more specifically, highly luminous ones known as quasars, in cosmology to measure the cosmological distances hence the expansion rate of the universe.

I developed the 2.5D numerical non-hydrodynamical FRADO code to simulate the dynamics of material in low ionized BLR. The code incorporates the realistic prescription of extended disk radiation field, advanced values of wavelength-dependent dust opacities (Szczerba et al., 1997; Röllig et al., 2013), dynamical dust sublimation process and shielding effect (Murray et al., 1995).

The results from 2.5D FRADO model presented in my publications can be then summerzied as follows:

- Paper I: The cloud motion is rather complex and strongly depends on the parameters like black hole mass, accretion rate, viewing angle towards the nucleus, and the metallicity of the material. It successfully explains many observational dynamical features of LIL-BLR, for example the escaping wind structure similar to empirical picture of Elvis (2000).

- Paper II: The model can explain the most recent sample of reverberation measured Hβ time-delays including the spread of data with respect the Eddington ratio of sources. Successful test of the model with the observationally-established radius-luminosity relation in AGNs confirms the predictive power of the model.

- Paper III: Test of the model with calculations of the spectral line generic profiles shows that it can appropriately explain the low-ionized broad emission lines, such as MgII and Hβ, observed in mean spectrum of quasars. Various parameters, including accretion rate, black hole mass, viewing angle, and stronger than other the dust-to-gas mass ratio can affect the shape of the spectral line profiles.

I have also published a spin-off paper (as the 2nd author) based on the results from 2.5D FRADO which is about the production of non-thermal emission due to collision of BLR clouds with the underlying disk (Müller et al., 2022).

6.2 Forthcoming work

There is another work in which I have employed the 2.5D FRADO to test the implications of the dusty wind model for broad line absorption quasars (Naddaf et al., 2022, under the first and very minor revision)

Dust-driven wind as a model of Broad Absorption Line quasars

The signatures of massive, energetic outflows in Broad Absorption Line Quasars (BAL QSOs) serves as a hallmark of their impact on the feedback process within Active Galactic Nuclei (AGN), ultimately shaping the evolution of the central black hole and galactic bulge. We examined the mechanism of dust-driven winds based on the failed radiatively accelerated dusty outflow (FRADO) model proposed by Czerny & Hryniewicz, letting it be responsible for the formation of massive outflow. We modeled BAL QSOs as sources viewed along the cone of energetic outflows and calculated the probabilities of observing the BAL phenomenon as a function of main global parameters such as black hole masses, Eddington ratios, and metallicities. Our findings were then compared to observational data from SDSS DR7, taking into account the presence or absence of an obscuring torus. Our results indicate that BAL QSOs are typically characterized by black hole masses larger than 10^8 solar masses, and the BAL effect grows stronger with increasing accretion rate. High metallicities also enhance the likelihood of observing BAL features in the presence of a torus. The consistency of our model with the data supports the interpretation of the BAL phenomenon as a result of source orientation, rather than a transitory stage in AGN evolution.

6.3   Prospecs

It is much more there to develop the 2.5D FRADO model further and to test with the observational data, for example:

  (i) to include even more realistic properties of dust in AGNs from observational point of view including the dependence of the sublimation temperature on grain size and chemical composition, and including additional grain types like amorphous carbon grains, olivine grains etc. into the code as the input;

 (ii) to use radiative transfer codes in combination with the cloud distribution from 2.5D FRADO code to get the line emissivity, including the presence or absence of dust in the cloud;

(iii) to incorporate the line-driving mechanism into the code to see whether or not the HIL, LIL, and torus outflows really form separated nested structures, in order to examine the holistic geometry of AGNs from the theoretical point of view versus observational;

(iv) to further test the more realistic non-parametric geometry of BLR based on 2.5D FRADO model in other contexts such as microlensing;

 (v) and ultimately to perform detailed case studies with the code on the results of distribution of clouds and geometry of BLR shaping partially the geometry of AGNs, and subsequently calculation of corresponding time-delay histograms to examine the coherency of theory and observation, thus calibrating the radius-luminosity relation as the basis of quasars in cosmology. Precise determination of the mean (effective) radius of the BLR from the model will allow to attempt to measure the Hubble constant with FRADO model.

Bibliography

Abramowicz, M. A., Czerny, B., Lasota, J. P., & Szuszkiewicz, E. 1988, ApJ, 332, 646

Adhikari, T. P., Hryniewicz, K., Różańska, A., Czerny, B., & Ferland, G. J. 2018, ApJ, 856, 78

Angel, J. R. P., Stockman, H. S., Woolf, N. J., Beaver, E. A., & Martin, P. G. 1976, ApJ, 206, L5

Antonucci, R. 1993, ARA&A, 31, 473

Antonucci, R. & Miller, J. S. 1985, ApJ, 297, 621

Antonucci, R. R. J. 1984, ApJ, 278, 499

Armijos-Abendaño, J., López, E., Llerena, M., & Logan, C. H. A. 2022, MNRAS, 514, 1535

Baldwin, J., Ferland, G., Korista, K., & Verner, D. 1995, ApJ, 455, L119

Baldwin, J. A. 1977, MNRAS, 178, 67P

Baldwin, J. A., Rees, M. J., Longair, M. S., & Perryman, M. A. C. 1978, ApJ, 226, L57

Baron, D. & Ménard, B. 2019, MNRAS, 487, 3404

Barvainis, R. 1987, ApJ, 320, 537

Baskin, A. & Laor, A. 2018, MNRAS, 474, 1970

Begelman, M. C., McKee, C. F., & Shields, G. A. 1983, ApJ, 271, 70

Bennett, C. L., Banday, A. J., Gorski, K. M., et al. 1996, ApJ, 464, L1

Bentz, M. C., Denney, K. D., Grier, C. J., et al. 2013, ApJ, 767, 149

Bentz, M. C., Peterson, B. M., Pogge, R. W., & Vestergaard, M. 2009, ApJ, 694, L166

Bentz, M. C., Williams, P. R., & Treu, T. 2022, ApJ, 934, 168

Blandford, R. D. & Begelman, M. C. 1999, MNRAS, 303, L1

Blandford, R. D. & Payne, D. G. 1982, MNRAS, 199, 883

Bonzini, M., Padovani, P., Mainieri, V., et al. 2013, MNRAS, 436, 3759

Capriotti, E., Foltz, C., & Byard, P. 1980, ApJ, 241, 903

Castor, J. I., Abbott, D. C., & Klein, R. I. 1975, ApJ, 195, 157

Chen, K., Halpern, J. P., & Filippenko, A. V. 1989, ApJ, 339, 742

Collin, S. & Zahn, J.-P. 1999, A&A, 344, 433

Collin-Souffrin, S., Dyson, J. E., McDowell, J. C., & Perry, J. J. 1988, MNRAS, 232, 539

Czerny, B., Beaton, R., Bejger, M., et al. 2018, Space Sci. Rev., 214, 32

Czerny, B., Du, P., Wang, J.-M., & Karas, V. 2016, ApJ, 832, 15

Czerny, B. & Hryniewicz, K. 2011, A&A, 525, L8

Czerny, B., Hryniewicz, K., Maity, I., et al. 2013, A&A, 556, A97

Czerny, B., Li, Y.-R., Hryniewicz, K., et al. 2017, ApJ, 846, 154

Czerny, B., Modzelewska, J., Petrogalli, F., et al. 2015, Advances in Space Research, 55, 1806

Czerny, B., Rózańska, A., & Kuraszkiewicz, J. 2004, A&A, 428, 39

Czerny, M. & King, A. R. 1989, MNRAS, 236, 843

Dauser, T., Garcia, J., Wilms, J., et al. 2013, MNRAS, 430, 1694

Di Valentino, E. 2021, MNRAS, 502, 2065

Di Valentino, E., Melchiorri, A., Mena, O., Pan, S., & Yang, W. 2021, MNRAS, 502, L23

Done, C. & Krolik, J. H. 1996, ApJ, 463, 144

Dong, X., Wang, T., Wang, J., et al. 2008, MNRAS, 383, 581

Dorodnitsyn, A. & Kallman, T. 2021, ApJ, 910, 67

Dorodnitsyn, A., Kallman, T., & Proga, D. 2016, ApJ, 819, 115

Elitzur, M. & Shlosman, I. 2006, ApJ, 648, L101

Elvis, M. 2000, ApJ, 545, 63

Everett, J. E. & Murray, N. 2007, ApJ, 656, 93

Fanaroff, B. L. & Riley, J. M. 1974, MNRAS, 167, 31P

Fath, E. A. 1909, Lick Observatory Bulletin, 149, 71

Ferland, G. J., Chatzikos, M., Guzmán, F., et al. 2017, Rev. Mexicana Astron. Astrofis., 53, 385

Ferland, G. J., Korista, K. T., Verner, D. A., et al. 1998, PASP, 110, 761

Ferland, G. J. & Osterbrock, D. E. 1986, ApJ, 300, 658

Freedman, W. L., Madore, B. F., Hoyt, T., et al. 2020, ApJ, 891, 57

Gardner, E. & Done, C. 2014, MNRAS, 442, 2456

Giustini, M. & Proga, D. 2019, A&A, 630, A94

Goad, M. R., Korista, K. T., & Ruff, A. J. 2012, MNRAS, 426, 3086

Goodrich, R. W. 1995, ApJ, 440, 141

GRAVITY Collaboration, Amorim, A., Bauböck, M., et al. 2021, A&A, 648, A117

GRAVITY Collaboration, Amorim, A., Bauböck, M., et al. 2020, A&A, 643, A154

GRAVITY Collaboration, Sturm, E., Dexter, J., et al. 2018, Nature, 563, 657

Greenstein, J. L. 1963, Nature, 197, 1041

Greenstein, J. L. & Matthews, T. A. 1963, AJ, 68, 279

Grier, C. J., Peterson, B. M., Horne, K., et al. 2013, ApJ, 764, 47

Haardt, F. & Maraschi, L. 1991, ApJ, 380, L51

Hazard, C., Mackey, M. B., & Shimmins, A. J. 1963, Nature, 197, 1037

Henri, G. & Pelletier, G. 1991, ApJ, 383, L7

Higginbottom, N., Proga, D., Knigge, C., et al. 2014, ApJ, 789, 19

Hubble, E. 1929, Proceedings of the National Academy of Science, 15, 168

Hubble, E. P. 1926, ApJ, 64, 321

Ichimaru, S. 1977, ApJ, 214, 840

Ilić, D., Popović, L. Č., La Mura, G., Ciroi, S., & Rafanelli, P. 2012, A&A, 543, A142

Israelian, G. 1997, BAAS, 29, 1466

Kaastra, J. S., Steenbrugge, K. C., Crenshaw, D. M., et al. 2004, A&A, 422, 97

Kaspi, S., Smith, P. S., Netzer, H., et al. 2000, ApJ, 533, 631

Kellermann, K. I., Sramek, R. A., Schmidt, M., Green, R. F., & Shaffer, D. B. 1994, AJ, 108, 1163

Kollatschny, W. & Zetzl, M. 2011, Nature, 470, 366

Konigl, A. & Kartje, J. F. 1994, ApJ, 434, 446

Korista, K. & Ferland, G. 1998, ApJ, 495, 672

Kormendy, J. & Ho, L. C. 2013, ARA&A, 51, 511

Kormendy, J. & Richstone, D. 1995, ARA&A, 33, 581

Kovačević-Dojčinović, J., Marčeta-Mandić, S., & Popović, L. Č. 2017, Frontiers in Astronomy and Space Sciences, 4, 7

Kraemer, S. B. & Harrington, J. P. 1986, ApJ, 307, 478

Krolik, J. H. & Kriss, G. A. 1995, ApJ, 447, 512

Kubota, A. & Done, C. 2018, MNRAS, 480, 1247

Lemaître, G. 1927, Annales de la Société Scientifique de Bruxelles, 47, 49

Lemaître, G. 1931, MNRAS, 91, 483

Li, J.-W. & Cao, X. 2022, ApJ, 926, 11

Li, Y.-R., Wang, J.-M., Ho, L. C., Du, P., & Bai, J.-M. 2013, ApJ, 779, 110

Loska, Z., Czerny, B., & Szczerba, R. 2004, MNRAS, 355, 1080

Lusso, E. 2020, Frontiers in Astronomy and Space Sciences, 7, 8

Lynden-Bell, D. 1969, Nature, 223, 690

MacAlpine, G. M. 1985, in Astrophysics of Active Galaxies and Quasi-Stellar Objects, ed. J. S. Miller, 259–288

Maiolino, R., Marconi, A., & Oliva, E. 2001a, A&A, 365, 37

Maiolino, R., Marconi, A., Salvati, M., et al. 2001b, A&A, 365, 28

Marconi, A., Axon, D. J., Maiolino, R., et al. 2008, ApJ, 678, 693

Mardaljevic, J., Raine, D. J., & Walsh, D. 1988, Astrophysical Letters and Communications, 26, 357

Markowitz, A. G., Krumpe, M., & Nikutta, R. 2014, MNRAS, 439, 1403

Martin, P. G., Stockman, H. S., Angel, J. R. P., Maza, J., & Beaver, E. A. 1982, ApJ, 255, 65

Matt, G., Perola, G. C., & Piro, L. 1991, A&A, 247, 25

Miller, J. S. & Antonucci, R. R. J. 1983, ApJ, 271, L7

Miniutti, G., Saxton, R. D., Rodríguez-Pascual, P. M., et al. 2013, MNRAS, 433, 1764

Müller, A. L., Naddaf, M.-H., Zajaček, M., et al. 2022, ApJ, 931, 39

Murray, N. & Chiang, J. 1997, ApJ, 474, 91

Murray, N., Chiang, J., Grossman, S. A., & Voit, G. M. 1995, ApJ, 451, 498

Naddaf, M. H., Martinez-Aldama, M. L., Marziani, P., et al. 2022, arXiv e-prints, arXiv:2212.08222

Narayan, R. & Yi, I. 1994, ApJ, 428, L13

Netzer, H. 1987, MNRAS, 225, 55

Netzer, H. 2015, ARA&A, 53, 365

Netzer, H. & Davidson, K. 1979, MNRAS, 187, 871

Netzer, H. & Laor, A. 1993, ApJ, 404, L51

Netzer, H. & Marziani, P. 2010, ApJ, 724, 318

Neugebauer, G., Morton, D., Oke, J. B., et al. 1980, ApJ, 238, 502

Novikov, I. D. & Thorne, K. S. 1973, in Black Holes (Les Astres Occlus), 343–450

Osterbrock, D. E. 1978, Phys. Scr, 17, 285

Osterbrock, D. E. & Mathews, W. G. 1986, ARA&A, 24, 171

Padovani, P. 2016, A&A Rev., 24, 13

Padovani, P. 2017a, Frontiers in Astronomy and Space Sciences, 4, 35

Padovani, P. 2017b, Nature Astronomy, 1, 0194

Padovani, P., Alexander, D. M., Assef, R. J., et al. 2017, A&A Rev., 25, 2

Padovani, P., Miller, N., Kellermann, K. I., et al. 2011, ApJ, 740, 20

Pancoast, A., Brewer, B. J., & Treu, T. 2014, MNRAS, 445, 3055

Peacock, J. A., Miller, L., & Longair, M. S. 1986, MNRAS, 218, 265

Peterson, B. M., Ali, B., Horne, K., et al. 1993, ApJ, 402, 469

Peterson, B. M. & Gaskell, C. M. 1991, ApJ, 368, 152

Peterson, B. M. & Wandel, A. 1999, ApJ, 521, L95

Pietrini, P., Torricelli-Ciamponi, G., & Risaliti, G. 2019, A&A, 628, A26

Planck Collaboration, Ade, P. A. R., Aghanim, N., et al. 2016, A&A, 594, A13

Pounds, K. A., Nandra, K., Stewart, G. C., George, I. M., & Fabian, A. C. 1990, Nature, 344, 132

Proga, D. & Kallman, T. R. 2004, ApJ, 616, 688

Proga, D., Stone, J. M., & Kallman, T. R. 2000, ApJ, 543, 686

Rees, M. J., Silk, J. I., Werner, M. W., & Wickramasinghe, N. C. 1969, Nature, 223, 788

Reines, A. E. & Volonteri, M. 2015, ApJ, 813, 82

Richstone, D. O. & Schmidt, M. 1980, ApJ, 235, 361

Rieke, G. H. 1978, ApJ, 226, 550

Riess, A. G., Casertano, S., Yuan, W., Macri, L. M., & Scolnic, D. 2019, ApJ, 876, 85

Riess, A. G., Yuan, W., Casertano, S., Macri, L. M., & Scolnic, D. 2020, ApJ, 896, L43

Risaliti, G. & Elvis, M. 2010, A&A, 516, A89

Risaliti, G. & Lusso, E. 2019, Nature Astronomy, 3, 272

Risaliti, G., Nardini, E., Salvati, M., et al. 2011, MNRAS, 410, 1027

Röllig, M., Szczerba, R., Ossenkopf, V., & Glück, C. 2013, A&A, 549, A85

Różańska, A. 1999, MNRAS, 308, 751

Różańska, A., Dumont, A. M., Czerny, B., & Collin, S. 2002, MNRAS, 332, 799

Różańska, A., Malzac, J., Belmont, R., Czerny, B., & Petrucci, P. O. 2015, A&A, 580, A77

Rudy, R. J., Schmidt, G. D., Stockman, H. S., & Moore, R. L. 1983, ApJ, 271, 59

Rudy, R. J., Schmidt, G. D., Stockman, H. S., & Tokunaga, A. T. 1984, ApJ, 278, 530

Sacchi, A., Risaliti, G., Signorini, M., et al. 2022, A&A, 663, L7

Salpeter, E. E. 1964, ApJ, 140, 796

Sandage, A. 1965, ApJ, 141, 1560

Sandage, A. & Tammann, G. A. 1990, ApJ, 365, 1

Schmidt, M. 1963, Nature, 197, 1040

Schmidt, M. 1970, ApJ, 162, 371

Seyfert, C. K. 1943, ApJ, 97, 28

Shablovinskaya, E. S., Afanasiev, V. L., & Popović, L. č. 2020, ApJ, 892, 118

Shajib, A. J., Birrer, S., Treu, T., et al. 2020, MNRAS, 494, 6072

Shakura, N. I. & Sunyaev, R. A. 1973, A&A, 24, 337

Shuder, J. M. & MacAlpine, G. M. 1977, in Bulletin of the American Astronomical Society, Vol. 9, 431

Shuder, J. M. & MacAlpine, G. M. 1979, ApJ, 230, 348

Slipher, V. M. 1917, Lowell Observatory Bulletin, 3, 59

Spergel, D. N., Verde, L., Peiris, H. V., et al. 2003, ApJS, 148, 175

Suganuma, M., Yoshii, Y., Kobayashi, Y., et al. 2006, ApJ, 639, 46

Szczerba, R., Omont, A., Volk, K., Cox, P., & Kwok, S. 1997, A&A, 317, 859

Tanaka, Y., Nandra, K., Fabian, A. C., et al. 1995, Nature, 375, 659

Thompson, I., Stockman, H. S., Angel, J. R. P., & Beaver, E. A. 1980, MNRAS, 192, 53

Thorne, J., Robotham, A., Davies, L., & Bellstedt, S. 2022, AGN Unification Diagram, Was originally created to be included in the introduction of Thorne J. E., et al., 2022, MNRAS, 509, 4940

Titarchuk, L. 1994, ApJ, 434, 570

Tully, R. B. & Fisher, J. R. 1977, A&A, 54, 661

Urry, C. M. & Padovani. 1995, PASP, 107, 803

Ursini, F., Dovčiak, M., Zhang, W., et al. 2020, A&A, 644, A132

Wandel, A., Peterson, B. M., & Malkan, M. A. 1999, ApJ, 526, 579

Wang, J.-M., Du, P., Baldwin, J. A., et al. 2012, ApJ, 746, 137

Wang, J.-M., Du, P., Brotherton, M. S., et al. 2017, Nature Astronomy, 1, 775

Wang, J.-M., Ge, J.-Q., Hu, C., et al. 2011, ApJ, 739, 3

Waters, T., Kashi, A., Proga, D., et al. 2016, ApJ, 827, 53

Waters, T. & Proga, D. 2016, MNRAS, 460, L79

Waters, T., Proga, D., Dannen, R., & Dyda, S. 2022, ApJ, 931, 134

Witt, H. J., Czerny, B., & Zycki, P. T. 1997, MNRAS, 286, 848

Wong, K. C., Suyu, S. H., Chen, G. C. F., et al. 2020, MNRAS, 498, 1420

Zajaček, M., Czerny, B., Martinez-Aldama, M. L., et al. 2021, ApJ, 912, 10

Zeldovich, Y. B. 1964, Soviet Physics Doklady, 9, 195

Appendix: statements of contribution
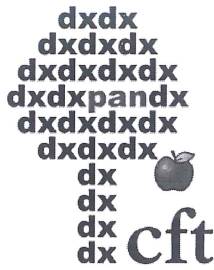
Center for Theoretical Physics
of the Polish Academy of Sciences

Centrum Fizyki Teoretycznej Polskiej Akademii Nauk

Warsaw, March 18, 2023

Prof. Bożena Czerny
Centrum Fizyki Teoretycznej PAN
Al. Lotników 32/46
02-668 Warsaw, Poland
Tel.: +48 22 847 09 20
Email: bcz@cft.edu.pl

Information about the co-authorship of the paper

As a co-author of the paper by Naddaf et al. (Naddaf, Czerny, Szczerba), titled "The Picture of BLR in 2.5D FRADO: Dynamics and Geometry" published in Astrophysical Journal in 2021, (Volume 920, id 30), I contributed to this paper by helping to define the project which is about 10% to the total effort of this paper. I confirm that Mr. Naddaf contributed in 80% of the total effort by implementing and performing the entire computations of the dynamics, and analyzing the dynamics and geometry of BLR, and writing the manuscript.

Bożena Czerny

Nicolaus Copernicus Astronomical Center
of the Polish Academy of Sciences

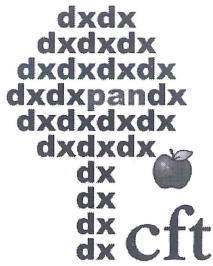Centrum Astronomiczne im. M. Kopernika Polskiej Akademii Nauk

Warsaw, March 18, 2023

Prof. Ryszard Szczerba
Centrum Astronomiczne im. M. Kopernika PAN
Ul. Rabianska 8
87-100 Torun, Poland
Tel.: +48 56 62 19 249
Email: szczerba@ncac.torun.pl

Information about the co-authorship of the paper

As a co-author of the paper by Naddaf et al. (Naddaf, Czerny, Szczerba), titled "The Picture of BLR in 2.5D FRADO: Dynamics and Geometry" published in *Astrophysical Journal* in 2021, (Volume 920, id 30), I contributed to this paper by helping with helping with implementation of the code developed by me and collaborators (*Röllig, M., Szczerba, R., Ossenkopf, V., & Glück, C. 2013, A&A, 549, A85*) which described the dust modelling procedure. I rate my contribution at about 10% to the total effort of this paper. I confirm that Mr. Naddaf contributed in 80% of the total effort by implementing and performing the entire computations of the dynamics, and analyzing the dynamics and geometry of BLR, and writing the manuscript.

R. Szczerba
Ryszard Szczerba

Center for Theoretical Physics
of the Polish Academy of Sciences

Centrum Fizyki Teoretycznej Polskiej Akademii Nauk

Warsaw, March 18, 2023

Prof. Bożena Czerny
Centrum Fizyki Teoretycznej PAN
Al. Lotników 32/46
02-668 Warsaw, Poland
Tel.: +48 22 847 09 20
Email: bcz@cft.edu.pl

Information about the co-authorship of the paper

As a co-author of the paper by Naddaf et al. (Naddaf, Czerny, Szczerba) titled "BLR Size in Realistic FRADO Model: The Role of Shielding Effect" published in the journal of Frontiers in Astronomy and Space Sciences in 2020, (Volume 7, id 15), I contributed to this paper by consulting the use of the data which I rate as about 5% of the total effort of this paper. I confirm that Mr. Naddaf contributed in 90% of the total effort by modelling the shielding effect and implementing and performing the entire computations of the BLR dynamics, and calculation of BLR size, and writing the manuscript.

Bożena Czerny

Nicolaus Copernicus Astronomical Center
of the Polish Academy of Sciences

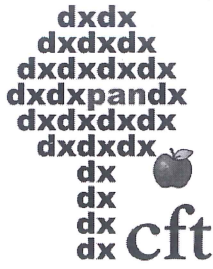Centrum Astronomiczne im. M. Kopernika Polskiej Akademii Nauk

Warsaw, March 18, 2023

Prof. Ryszard Szczerba
Centrum Astronomiczne im. M. Kopernika PAN
Ul. Rabianska 8
87-100 Torun, Poland
Tel.: +48 56 62 19 249
Email: szczerba@ncac.torun.pl

Information about the co-authorship of the paper

As a co-author of the paper by Naddaf et al. (Naddaf, Czerny, Szczerba) titled "BLR Size in Realistic FRADO Model: The Role of Shielding Effect" published in Frontiers in Astronomy and Space Sciences in 2020, (Volume 7, id 15), I contributed to this paper by consulting the dust subroutine which is about 5% to the total effort of this paper. I confirm that Mr. Naddaf contributed in 90% of the total effort by modelling the shielding effect and implementing and performing the entire computations of the BLR dynamics, and calculation of BLR size, and writing the manuscript.

R. Szczerba
Ryszard Szczerba

Center for Theoretical Physics
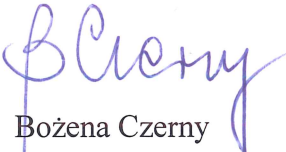# of the Polish Academy of Sciences

Centrum Fizyki Teoretycznej Polskiej Akademii Nauk

Warsaw, March 18, 2023

Prof. Bozena Czerny
Centrum Fizyki Teoretycznej PAN
Al. Lotników 32/46
02-668 Warsaw, Poland
Tel.: +48 22 847 09 20
Email: bcz@cft.edu.pl

Information about the co-authorship of the paper

As a co-author of the paper by Naddaf & Czerny, titled "Radiation pressure on dust explaining the low ionized broad emission lines in active galactic nuclei" published in the journal of Astronomy & Astrophysics in 2022, (Volume 663, id A77), I contributed to this paper by helping with finding the suitable data set and defining the spectral components. I rate my input at 10% to the total work in this paper. I confirm that Mr. Naddaf contributed in 90% of the total effort by implementing and performing the entire computations of the dynamics, and calculation of emission line profiles, and writing the manuscript.

Bożena Czerny